



## DISSERTATION

### The theory and application of inelastic coherence in the electron microscope

ausgeführt zum Zwecke der Erlangung des akademischen Grades eines  
Doktors der technischen Wissenschaften  
unter der Leitung von

Ao.Univ.Prof. Dr. Peter Schattschneider

E138

Institut für Festkörperphysik

eingereicht an der Technischen Universität Wien  
Fakultät für Physik

von

Dipl.-Ing. Walid Hetaba

0425909

Rechte Bahnzeile 16  
3494 Gedersdorf

Wien, im August 2015

## Zusammenfassung

In der vorliegenden Arbeit werden zwei auf den ersten Blick unabhängig erscheinende Techniken, “Energieverlust magnetisch chiraler Dichroismus” (EMCD) und “Energieverluste durch kanalisierte Elektronen” (ELCE), unter dem gemeinsamen Prinzip der interferometrischen “Elektronenenergieverlustspektrometrie” (EELS) beschrieben. Dazu werden die theoretischen Formulierungen der interferometrischen EELS, ELCE und EMCD dargestellt. Sowohl für ELCE als auch für EMCD werden Simulationen durchgeführt, die elastische und inelastische Streueffekte verbinden, um den Einfluss der dynamischen Beugung und Strahlkonvergenz auf die experimentellen Ergebnisse zu untersuchen.

Weiters wird EMCD im Rahmen von ausführlichen TEM-Untersuchungen von unterschiedlichen Heusler-Verbindungen und Magnetit verwendet. Dabei wird die Zuverlässigkeit in Hinblick auf den “täglichen Gebrauch” der Technik diskutiert. Die ausgewählten Materialien zeigen einen magnetostrukturellen Phasenübergang, der unter Verwendung von EMCD in-situ untersucht werden kann, um mehr Informationen über die Änderung der magnetischen Eigenschaften zu erhalten. Die Verbindung von Simulationen und Experimenten ermöglicht es, den magnetischen Phasenübergang für Materialien in der Spintronic maßzuschneidern.

Die ELCE Technik wird angewendet um die Änderung der Feinstruktur in Rutil bei Anregung von Endzuständen unterschiedlichen Charakters ortsspezifisch zu untersuchen. Kombinierte Blochwellen- und DFT-Simulationen zeigen exzellente Übereinstimmung mit den experimentellen Spektren.

Die vorliegende Arbeit zeigt, dass die Kombination von Simulationen dynamischer Beugungseffekte und Berechnungen der elektronischen Struktur notwendig ist um die Ergebnisse von ELCE und EMCD Messungen zu interpretieren. Diese Techniken können in zukünftigen Experimenten angewendet werden um z.B. die magnetischen Eigenschaften von Oberflächen und Grenzflächen zu untersuchen und um ortsabhängige Informationen über die Bindungen in Kristallen zu erhalten. Sie stellen hochentwickelte Mittel für elektronenmikroskopische Analysen in Gebieten wie funktionelle Materialien, Spintronics und Katalyse bereit.



## Abstract

In this work, two seemingly unrelated techniques, *energy-loss magnetic chiral dichroism* (EMCD) and *energy losses by channelled electrons* (ELCE), are described under the unifying principle of interferometric electron energy loss spectrometry (EELS). To this end, the theoretical formulations of interferometric EELS, ELCE and EMCD are presented. For both, ELCE and EMCD, simulations combining elastic and inelastic scattering effects are performed to discuss the influence of dynamical diffraction and beam convergence on the experimental results.

Furthermore, EMCD is applied in course of a thorough TEM investigation of different Heusler alloys as well as magnetite, discussing its reliability concerning a “daily use”. The chosen materials exhibit a magnetostructural phase transition which can be investigated in-situ using EMCD gaining knowledge about the changes of the magnetic properties. Combining simulations and experiments paves the way for tailoring of the magnetic phase transition of materials for use in spintronics.

The ELCE technique is applied to site-specifically investigate the change of the fine-structure as final states of different character are probed in rutile. It is shown that a combined Bloch wave and DFT simulation exhibits excellent agreement with the experimental spectra.

The presented work shows that the combination of simulations of dynamical diffraction effects and electronic structure calculations is necessary to interpret results of ELCE and EMCD measurements. These techniques can be applied in future experiments to investigate for example the magnetic properties at surfaces and interfaces and to gain site-specific information about the bonding situation in crystals. Thus, they provide sophisticated means for electron microscopical analyses in fields like functional materials, spintronics and catalysis.

# Danksagung

Ich bedanke mich bei Prof. Peter Schattschneider für seine Unterstützung und Betreuung meiner Doktorarbeit. Außerdem bin ich ihm dankbar dafür, dass er mich zur richtigen Zeit mit den richtigen Leuten bekannt gemacht hat und mir die Möglichkeit gegeben hat, an verschiedenen Forschungseinrichtungen zu arbeiten.

Ganz besonders möchte ich mich bei Dr. Stefan Löffler bedanken. Er hat mich bei meinen Simulationen mit “bw” und “ixchel” unterstützt und mir im Bereich der Grafikbearbeitung und im Umgang mit Linux geholfen. Außerdem habe ich die letzten fünf Jahre mit ihm im gemeinsamen Büro sehr genossen.

Dr. Michael Stöger-Pollach gebührt großer Dank für seine Hilfe im experimentellen Bereich der Arbeit. Seine Kommentare regten immer wieder zum Nachdenken an. Von ihm habe ich die praktische Arbeit am Elektronenmikroskop gelernt und das Interesse daran, die Fähigkeiten der Geräte möglichst auszureizen, übernommen.

Bei Prof. Johannes Bernardi möchte ich mich für die tolle Einbindung bei USTEM und die Finanzierung bedanken, ebenso dafür dass er mir die Freiheiten gegeben hat, die ich für das Schreiben meiner Arbeit brauchte.

Andreas Steiger-Thirsfeld und Jakob Gruber danke ich für die Hilfe bei der Probenpräparation und dafür, dass sie für mich so gute TEM-Proben hergestellt haben. Bei Charlotte Kitzhofer, den übrigen Mitgliedern von USTEM und bei Prof. Christoph Eisenmenger-Sittner und seiner Gruppe bedanke ich mich für das tolle Arbeitsklima.

Prof. Andreas Hütten danke ich für die Finanzierung und die Anleitung in dem Teil der Doktorarbeit, in dem ich mich mit Heusler-Verbindungen beschäftigt habe. Bei ihm, Lars Helmich, Niclas Teichert, Dr. Inga Ennen und Dr. Annalena Wolff bedanke ich mich für die freundliche Aufnahme in der Arbeitsgruppe bei meinen Aufenthalten in Bielefeld und die gute Zusammenarbeit.

Ganz herzlich möchte ich mich bei Prof. Schlögl bedanken, der mir die Möglichkeit gab an seinen Elektronenmikroskopen Messungen durchzuführen, mich immer wieder in seine Institute eingeladen und mich in meiner Arbeit gefördert hat. Außerdem danke ich ihm

dafür, dass er mich im letzten Jahr meiner Doktorarbeit finanziert hat. Dr. Marc Willinger danke ich für die ausgezeichnete Zusammenarbeit in seiner Arbeitsgruppe und dass er meine Arbeit ebenfalls gefördert hat. Der gesamten Arbeitsgruppe Elektronenmikroskopie der Abteilung Anorganische Chemie am FHI-Berlin danke ich für die freundliche Aufnahme bei meinen Aufenthalten in Berlin.

Der Fachschaft Physik und der Fachschaft Doktorat danke ich dafür, mir ein Umfeld geboten zu haben, in dem ich mich in meiner Freizeit anderen Dingen abseits der Doktorarbeit widmen konnte. Die Arbeit in der Studierendenvertretung hat mir viel Spaß gemacht und durch sie habe ich viel gelernt. Allen, mit denen ich in meiner Funktion als Vorsitzender der Studienkommission für die Doktoratsstudien zusammengearbeitet habe, danke ich für die interessante Zeit. Besonders möchte ich hier Stefan Kornher und sein Team vom Dekanatszentrum Freihaus erwähnen.

Dr. Ines Häusler danke ich dafür, dass sie mir bei meinen Aufenthalten in Berlin immer wieder ein Dach über dem Kopf gewährt hat. Ihr, Dr. Holm Kirmse und Dr. Anna Mogilatenko danke ich für ihre Freundschaft und die netten gemeinsamen Unternehmungen in Berlin und Umgebung. Durch sie alle und Prof. Wolfgang Neumann habe ich eine Reihe schöner Erinnerungen, die ich mit meinen Berlin-Aufenthalten seit 2008 verbinde.

Für die finanzielle Unterstützung in den letzten Jahren danke ich dem Fonds zur Förderung der wissenschaftlichen Forschung (FWF Projekte F4501-N16 “FOXSI” und I543-N20 “OMG”), der deutschen Forschungsgemeinschaft (DFG Schwerpunktsprogramm SPP 1599 “Ferroic Cooling”), der Max-Planck-Gesellschaft (Stipendium für Doktoranden), der Österreichischen Gesellschaft für Elektronenmikroskopie (ASEM), der European Microscopy Society (EMS), der Fakultät für Physik an der TU Wien und natürlich USTEM.

Abschließend möchte ich mich noch herzlich bei meinen Eltern und meiner Schwester bedanken, die mich durch alle Höhen und Tiefen dieser Doktorarbeit begleitet, unterstützt und motiviert haben. Auch meinen Großeltern danke ich dafür, dass sie mich immer wieder motiviert haben.

# Contents

<b>I. Preface</b>	<b>1</b>
<b>1. Introduction</b>	<b>2</b>
1.1. Transmission Electron Microscopy . . . . .	2
1.2. Analytical techniques . . . . .	6
1.3. Coherence effects in the TEM . . . . .	7
1.4. Simulations . . . . .	7
1.5. Outline . . . . .	8
<b>II. Interferometric EELS</b>	<b>9</b>
<b>2. Diffraction theory</b>	<b>10</b>
2.1. Kinematic theory of diffraction . . . . .	10
2.2. Dynamical theory of diffraction . . . . .	14
<b>3. The mixed dynamic form factor</b>	<b>21</b>
3.1. The double differential scattering cross section . . . . .	21
3.2. Models for the DDSCS . . . . .	23
3.2.1. Single plane wave . . . . .	23
3.2.2. Superposition of plane waves . . . . .	25
3.2.3. Bloch waves . . . . .	28
3.3. The MDFF for crystals . . . . .	29
<b>4. ELCE</b>	<b>32</b>
4.1. Simulations . . . . .	32
4.2. Early use of ELCE . . . . .	37

---

<b>5. EMCD</b>	<b>41</b>
5.1. The revealing of EMCD and its progress . . . . .	41
5.2. Theoretical description . . . . .	42
5.3. Experimental setup . . . . .	45
5.3.1. EELS detector setup . . . . .	45
5.3.2. Beam convergence . . . . .	48
5.4. Simulations . . . . .	50
5.4.1. Thickness dependence of the EMCD signal . . . . .	50
5.4.2. Effects of beam convergence . . . . .	58
5.5. Calculating magnetic moments . . . . .	66
<b>III. Applications</b>	<b>71</b>
<b>6. EMCD investigation of Heusler alloys</b>	<b>72</b>
6.1. Introduction . . . . .	72
6.2. Heusler compounds . . . . .	72
6.3. Magnetocaloric effect . . . . .	78
6.4. Ferroic cooling . . . . .	82
6.5. Investigation of Heusler alloys . . . . .	84
6.5.1. Overview of the investigated samples . . . . .	84
6.5.2. $\text{Ni}_2\text{MnSn}$ and $\text{Ni}_{52}\text{Mn}_{33.3}\text{Sn}_{14.7}$ . . . . .	85
6.5.3. $\text{Ni}_{50}\text{Mn}_{34.5}\text{In}_{15.5}$ . . . . .	89
6.5.4. $\text{Ni}_2\text{MnSn}$ – $\text{Ni}_2\text{MnGa}$ double layer . . . . .	98
6.5.5. $\text{Ni}_2\text{MnSn}$ gradient layer . . . . .	102
6.5.6. Other investigated samples . . . . .	105
6.6. Interpretation . . . . .	107
6.6.1. Results of the investigations . . . . .	107
6.6.2. Proposed workflow for EMCD experiments . . . . .	111
<b>7. EMCD investigation of magnetite</b>	<b>112</b>
7.1. The Verwey transition in magnetite . . . . .	112
7.2. In-situ EMCD investigation . . . . .	113

---

<b>8. ELCE investigation of rutile</b>	<b>116</b>
8.1. The crystal structure of rutile . . . . .	116
8.2. Simulations . . . . .	116
8.3. Experimental setup . . . . .	123
8.4. Results . . . . .	124
<b>IV. Summary</b>	<b>126</b>
<b>9. Conclusion and Outlook</b>	<b>127</b>
9.1. Summary . . . . .	127
9.2. Future experiments and theoretical approaches . . . . .	129
<b>List of Abbreviations</b>	<b>130</b>
<b>List of Figures</b>	<b>132</b>
<b>List of Tables</b>	<b>137</b>
<b>Bibliography</b>	<b>138</b>

Wie alles sich zum Ganzen webt,  
Eins in dem andern wirkt und lebt!

Johann Wolfgang von Goethe, Faust I

Part I.

Preface



# 1. Introduction

## 1.1. Transmission Electron Microscopy

The foundations of modern transmission electron microscopy were laid in the early 1930ies in Berlin, where the first transmission electron microscope (TEM) was invented and built by Knoll and Ruska [1]. The first commercial TEMs were available in 1936 manufactured by Siemens in Germany. In 1942 the Vienna University of Technology started to operate its first transmission electron microscope. Thus, the University performed high-end research using most modern technology. After a short time of operation, the TEM was removed to protect it from war damage. 1946 it was put back into operation, and remained at the Vienna University of Technology until the end of its life-time. The research pursued using the microscope focused mainly on biological, medical and chemical topics. A new TEM (Siemens ELMISKOP 1A) was acquired in 1965 and with it, the research focus changed from biological and medical question to materials science and solid state physics. As the trend in electron microscopy went to increasing accelerating voltages, 1975 the first 200 kV TEM in Austria was put into operation at the TU Wien. Since 1981 a Siemens ELMISKOP 1A was equipped with an electron energy-loss spectrometer. This instrument remained in use until 1996.

Not only experimental work was performed at the Vienna University of Technology. There was also a lot of progress achieved in the theoretical description of electron optics and electron scattering. Walter Glaser's research work focussed on electron optics which he pursued from 1949 until his death in 1960. In the last thirty years, Peter Schattschneider was responsible for the theoretical work on inelastic electron scattering. The current research focus includes magnetic chiral dichroism and vortex beams.

In 1999, the university service centre for transmission electron microscopy (USTEM) was established, uniting the operation of all transmission electron microscopes of the university in a joint pool. The acquisition of a new field emission TEM followed in 2001.

This microscope is located in one of the world's most exposed sites, in the 8th floor of one of the university's buildings. The influence of three subway and three tram lines are minimised using an active magnetic field compensation system. In 2008 a new transmission and a new scanning electron microscope were installed, while two old instruments were dismantled. A few years ago, the oldest TEM at the Vienna University of Technology was finally taken out of service after 31 years. The primary task of USTEM are microscopical and nano-analytical studies for various institutions and companies, as well as the training of students at the microscopes. The pool of instruments at USTEM is held up-to-date by modernising them and additional equipment were purchased. The newest acquisition in 2015 was a TEM sample holder with which cathodoluminescence experiments can be performed. Additional to the theoretical works mentioned above, the research focus of USTEM lies in low acceleration voltage transmission electron microscopy. In this field, it is one of the leading research groups.

A transmission electron microscope works in a very similar way as an optical microscope. Both consist of a source of light or electrons, respectively, a condenser system, an objective system and finally an imaging system. The difference to an optical microscope is that in a TEM electrons are used to form the image instead of light. The electrons are emitted from a thermionic source, which is a metal filament that is heated to a temperature  $T_C$ , such that the conduction electrons can overcome the material's work function. It is evident that the melting point  $T_m$  of the cathode material needs to be higher than  $T_C$ . Historically, Tungsten filaments were used in electron microscopes, with the filament's working temperature  $T_C = 2500$  K to  $3000$  K while the melting point is  $T_m = 3650$  K [2]. LaB<sub>6</sub> filaments, which are used nowadays, exhibit a lower work function, thus the cathodes are heated to a temperature  $T_C = 1400$  K to  $2000$  K. Applying an additional electrical field at the cathode further reduces the work function, which is called Schottky effect. Such Schottky emitters are Tungsten filaments covered with ZrO. The ZrO coating additionally reduces the work function of the Tungsten filament, leading to a working temperature of  $T_C = 1800$  K for Schottky emission [2]. If the tip of a Tungsten filament has a radius below  $0.1$   $\mu\text{m}$ , the potential barrier becomes so narrow that the electrons can be emitted by tunnelling through the barrier. Such emitters are called field emission guns (FEG). Field emission emitters are available as heated filaments or as a so-called cold FEG. The heating of a FEG is mainly to prevent adsorption of material on the filament [2]. The energy distribution of electrons emitted by heated filaments can be described by a combination of a Gaussian and Lorentz distribu-

tion [3]. The electrons emitted from a cold FEG can be described by a Fowler-Nordheim distribution, which is typical for the quantum mechanical tunneling effect [4].

Making use of the fact that electrons are charged particles, they are accelerated using electric fields and the magnetic lenses of the condenser-, objective- and projective-system are used to propagate the electron beam through the sample until it reaches the imaging system. This could consist of either a fluorescent screen or a charge-coupled device (CCD). Depending on the operating mode of the magnetic lenses, either a magnified image of the sample or a diffraction pattern can be made visible. Changing a TEM from imaging mode to a mode where diffraction patterns can be acquired, is facilitated easily by simply pushing a button. This is because of the fact that in magnetic lenses the focal length can be tuned continuously. A schematic of a TEM is shown in figure 1.1.

The reason for using electrons instead of light is the possibility of a higher spatial resolution, determined by the Abbé limit [1]. It is noteworthy that at the time of the invention of the electron microscope, Ernst Ruska was not aware of the wave nature of the electrons and he used a description applying geometrical optics. Only later a wave optical approach was used. As with all optical instruments, magnetic lenses suffer from similar problems and show lens aberrations, which worsen the achievable resolution. The point resolution of a FEI Tecnai G<sup>2</sup> TF 20 for example, is 0.21 nm. What was available for optical systems for a long time, became available for TEMs only in recent years: aberration corrector systems. They use a system of multipole magnetic lenses in order to correct for the lens aberrations. A JEOL JEM-ARM200F microscope using a corrector system for the condenser system as well as the objective system, achieves a point resolution of 0.11 nm in TEM mode and a spatial resolution of 0.08 nm in the scanning TEM mode.

A modern TEM is a versatile tool for materials science, as it provides a wide variety of analytical techniques. Additionally to the capabilities of imaging and diffraction techniques, energy dispersive x-ray (EDX) analysis, as well as electron energy-loss spectrometry (EELS) can be performed. These two techniques are complementary, as EELS is advantageous for investigating materials with low or medium atomic number  $Z$ , while EDX has advantages when examining materials with higher values of  $Z$ . Both techniques give the possibility for a chemical investigation of TEM samples.

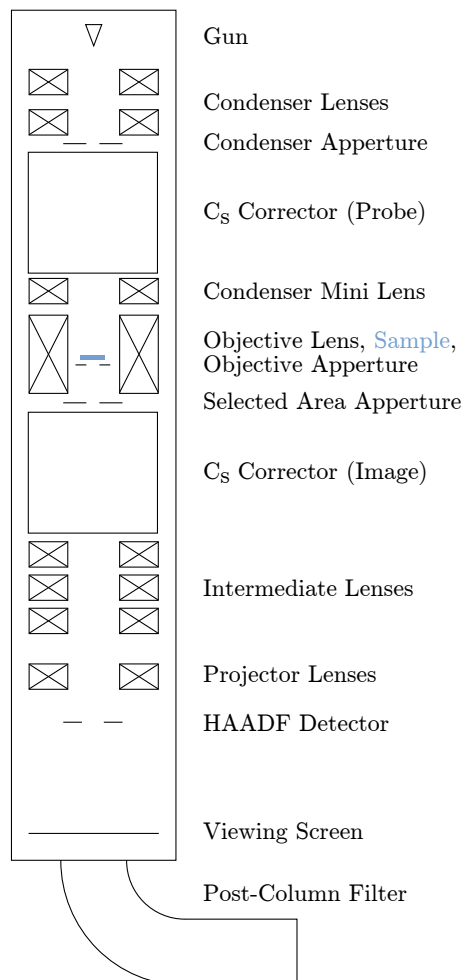


Figure 1.1.: Schematic of a transmission electron microscope.

## 1.2. Analytical techniques

Electrons on their way through the sample do not only experience elastic interaction with the sample atoms but also inelastic scattering. Electrons of the sample atoms are excited and characteristic X-rays are emitted as soon as these atoms relax into their ground state. The emitted radiation gives information about the samples' constituents and makes elemental quantification possible. One should keep in mind that the relative errors for elemental quantification are ca. 5-10% [1].

Another analytical technique used quite often is EELS. Again, beam electrons experience inelastic scattering but now the energy of these electrons itself is recorded in a spectrum. This is usually done by separating electrons of different energies using a sector magnet. These devices can either be mounted below the viewing screen (post-column energy filter) or inside the microscope column in between the objective and projective lens system (in-column filter).

Using EELS, quantification of the elemental composition of a TEM sample is also possible, with an error of 1-5% [3]. Moreover, besides elemental analysis, EELS enables to calculate the sample thickness (with an accuracy of ca. 10%) and to investigate the chemical environment of the probed atoms in the sample by analysing the fine-structure of the respective core-loss elemental edges. The latter technique includes detailed investigation of the energy-loss near edge structure (ELNES). For a detailed description of the possibilities of EELS, see [3].

When performing EELS experiments, energy resolution is important. With modern TEMs using a LaB<sub>6</sub> cathode or a FEG, values of 0.5 eV to 1.0 eV are achieved. When a monochromator is installed, values of 0.1 eV to 0.3 eV are obtained. Using a cold FEG as electron source, an energy resolution below 0.35 eV is available without the use of a monochromating device. The current optimum using the Nion Hermes microscope, equipped with a monochromator and a sophisticated stabilisation system of the microscope's high tension, is an energy resolution of ca. 10 meV [1, 3].

Advanced methods in EELS provide the possibility to gain information about the chemical environment of atoms in the sample as well as knowledge about bonding situations. Furthermore, magnetic properties can be investigated at the atomic scale and site-specific information can be retrieved. All this is of paramount importance when it comes to studying e.g. materials for catalysis, spintronics and magnetostructural phase transitions or functional materials. Nevertheless, performing these techniques can be

quite demanding and cause problems. Mainly it is the lack of signal intensity that has to be dealt with. Furthermore, one has to work very thoroughly and compare the results with simulations in order to interpret them.

### 1.3. Coherence effects in the TEM

Coherence effects in the TEM can be observed every time phase contrast imaging is used. For example, every high resolution TEM image relies on coherence effects [1]. Interferometry in the TEM is nothing to be established in a sophisticated way, it rather “happens” every time one investigates a crystalline sample. The crystal itself acts as a coherent beam splitter, creating interfering electron waves [5].

The effects of coherence on inelastic scattering processes have been under investigation for more than 30 years. Kohl and Rose published their work on image formation using inelastically scattered electrons in 1985 [6]. In their work, the mixed dynamic form factor (MDFF) was introduced. Using the MDFF, inelastic coherence can best be modelled. There is an alternative approach by Allen and co-workers [7, 8]. Inelastic coherence was studied repeatedly leading to the description of interferometric EELS. The possibility of interferometric EELS as well as some applications were elucidated in [5, 9, 10]. The first application of interferometric EELS reported was the technique called *energy losses by channelled electrons* (ELCE), while in 2003 another technique, *energy-loss magnetic chiral dichroism* (EMCD), was described.

### 1.4. Simulations

For both techniques, ELCE and EMCD, one has to consider dynamical diffraction effects, which can significantly influence the measured signal. Therefore, the experimental energy-loss spectra have to be compared with simulations in order to interpret the results of the measurements. This is done using a simulation software that makes use of the Bloch wave formalism. The change of the relative intensities of elemental core-loss edges due to channelling effects can be calculated. Furthermore, the modulation of the measured EMCD effect with respect to sample thickness and orientation can be simulated. Details on the simulation program can be found in [11].

Other simulation software packages, capable of modelling a material’s electronic struc-

ture, can be used to calculate energy-loss spectra. In this work, we used the density functional theory (DFT) simulation package WIEN2k. Details on this software can be found in [12, 13]. Some information about how this program can be used for electron microscopy and EELS are found for example in [14, 15]. The DFT software packages are, in contrast to the simulation programs described in the above paragraph, ignoring the dynamical scattering effects in a crystal. Therefore, in order to fully describe the acquired spectra when performing ELCE or EMCD, one needs to combine both simulation softwares. This was reported in [16, 17] and it is also described in the following work.

## 1.5. Outline

In this work, the basic formulations underlying the theory of interferometric EELS are described (chapters 2 and 3). Furthermore, two at the first sight seemingly unrelated methods are described and applied under the unifying aspect of interferometric EELS. The theory of ELCE and EMCD can be found in chapters 4 and 5. The application of EMCD in a thorough electron microscopical investigation of Heusler alloys is described in chapter 6 and the reliability of the technique, concerning a “daily use” is discussed. Additionally, EMCD measurements on magnetite can be found in chapter 7. The technique ELCE is applied to site-specifically investigate the fine structure of the oxygen K-edge of rutile, which is presented in chapter 8. This chapter is based on an article published in the peer-reviewed journal *Micron* [17].

Part II.

## Interferometric EELS



## 2. Diffraction theory

### 2.1. Kinematic theory of diffraction

Considering scattering at the crystal lattice, Bragg's law describes the situation of constructive interference of the electron beams and thus the existence of reflections in the observed diffraction pattern:

$$2d_{hkl} \sin \theta_B = n \cdot \lambda. \quad (2.1)$$

The distance of lattice planes with Miller indices  $(hkl)$  is given by  $d_{hkl}$ ,  $\theta_B$  is the Bragg angle,  $\lambda$  is the wave length of the electron beam and  $n$  denotes an integer. Using reciprocal lattice vectors, one can find an equivalent, vectorial description of this situation:

$$\mathbf{k} - \mathbf{k}_0 = \mathbf{q} = \mathbf{g}, \quad (2.2)$$

with  $\mathbf{k}_0$  the incident wave vector,  $\mathbf{k}$  the diffracted wave vector,  $\mathbf{q}$  the momentum transfer vector and  $\mathbf{g}$  a reciprocal lattice vector. Using the concept of the Ewald sphere, one can easily visualise the situation and that exact Bragg conditions are fulfilled every time the Ewald sphere intersects a point in the reciprocal lattice (see figure 2.1). From the figure it also becomes clear that the vectorial description of equation (2.2) is equivalent to equation (2.1), keeping in mind that  $|\mathbf{k} - \mathbf{k}_0| = (4\pi \sin \theta_B)/\lambda$  and  $g = (2\pi)/d_{hkl}$ .

The amplitude of the scattered wave can be calculated using the formula [2]:

$$F(\mathbf{q}) = \sum_{k=1}^n f_k \exp[-i(\mathbf{k} - \mathbf{k}_0) \cdot \mathbf{r}_k] \cdot \sum_m \sum_n \sum_o \exp[-i(\mathbf{k} - \mathbf{k}_0) \cdot \mathbf{r}_g] = F_{\text{cell}} \cdot G, \quad (2.3)$$

with  $\mathbf{r}_k = u_k \mathbf{a}_1 + v_k \mathbf{a}_2 + w_k \mathbf{a}_3$  denoting the position of the atoms present in the unit cell and  $\mathbf{r}_g = m \mathbf{a}_1 + n \mathbf{a}_2 + o \mathbf{a}_3$  the translation vector describing the origins of the unit cells. The first factor in equation (2.3) is called structure amplitude while the second factor is named lattice amplitude. For details on the derivation see e.g. [2] and [18].

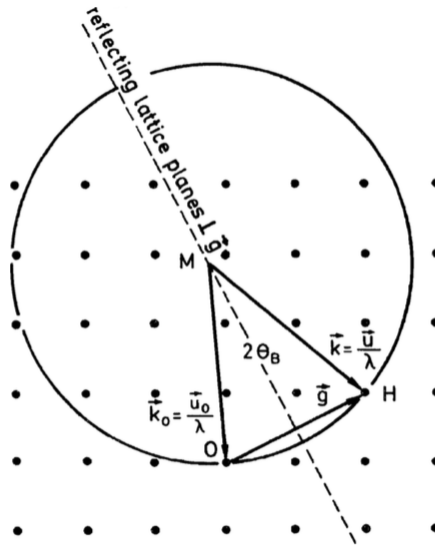


Figure 2.1.: Sketch illustrating the exact Bragg condition in which the Ewald sphere intersects a reciprocal lattice point. The sphere has a radius of  $1/\lambda$  ( $\mathbf{u}_0$  and  $\mathbf{u}$  are unit vectors in the respective directions), the reciprocal lattice vector  $\mathbf{g}$  is normal to the corresponding lattice plane ( $hkl$ ) with  $g = 1/d_{hkl}$ . From the sketch it can also be seen that  $|\mathbf{k} - \mathbf{k}_0| = (2 \sin \theta_B)/\lambda$ . Taken from [2]. On has to keep in mind that in this sketch a different convention is used with  $\mathbf{k} = 1/\lambda$  instead of  $\mathbf{k} = (2\pi)/\lambda$ . Thus the values in this figure have to be multiplied by  $2\pi$  to get the same results as in the text.

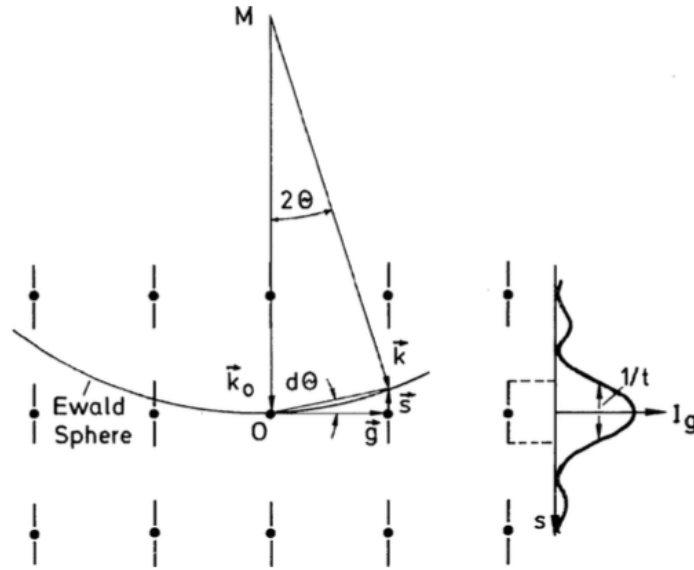


Figure 2.2.: The excitation error  $\mathbf{s}$  describes the deviation from the exact Bragg condition. The elongated shape of the diffraction spots' intensity  $I_g$  ("relrods"), present for example in thin TEM samples, is shown on the right hand side. Image taken from [2].

The structure amplitude gives certain restriction on which reflections in the diffraction pattern are excited and which are suppressed, depending on the actual crystal structure.

The lattice amplitude on the other hand, is responsible for the fact that in actual TEM experiments diffraction spots are excited even if the Bragg condition is not exactly fulfilled. To understand this behaviour, first the excitation error  $\mathbf{s}$  is introduced, which describes the deviation from the exact Bragg condition (see figure 2.2). The excitation error points from the reciprocal lattice point  $\mathbf{g}$  towards the Ewald sphere in a direction parallel to the incident wave vector. The magnitude of  $\mathbf{s}$  is defined as

$$s = g\Delta\theta, \quad (2.4)$$

with  $\Delta\theta$  the tilt angle out of the exact Bragg condition. In such a case with a small tilt out of the Bragg condition, one gets for the lattice amplitude [2]:

$$G = \sum_{m,n,o} \exp[-i\mathbf{s} \cdot \mathbf{r}_g]. \quad (2.5)$$

Replacing the sum with an integral over the crystal volume  $V = L_1L_2L_3$ , the diffracted intensity becomes:

$$I_g \propto |F_{\text{cell}}|^2 \frac{4 \sin^2(s_x L_1/2)}{(s_x a_1)^2} \frac{4 \sin^2(s_y L_2/2)}{(s_y a_2)^2} \frac{4 \sin^2(s_z L_3/2)}{(s_z a_3)^2}. \quad (2.6)$$

Taking a closer look on the factor describing the  $z$  direction, which is per definition corresponding to the thickness  $t$  of the TEM sample, one can easily find that it has its maximum value at  $s_z = 0$ , while it first becomes zero at  $s_z = (2\pi)/L_3 = (2\pi)/t$ . The same behaviour is found for the  $x$  and  $y$  direction with the factors becoming zero at much lower excitation errors  $s_x = (2\pi)/L_1$  and  $s_y = (2\pi)/L_2$ . This behaviour gives rise to the needle shaped intensity of the reciprocal lattice points. Consequently, it allows the excitation of diffraction spots for not-exact Bragg conditions as the Ewald sphere can intersect the “relrods” with an excitation error  $\mathbf{s} \neq 0$ .

In [2], Fresnel diffraction is used to calculate the contribution of a layer  $dz$  of the TEM sample to the amplitude of the diffracted beam, which leads to the introduction of the important quantity called *extinction distance*  $\xi_g$ . The amplitude is found to be:

$$\psi_g = i \frac{\pi}{\xi_g} \exp[2\pi i k_0 t] \int_0^t \exp[-2\pi i s z] dz, \quad (2.7)$$

with the extinction distance

$$\xi_g = \frac{\pi V_e}{\lambda F(\theta)}. \quad (2.8)$$

$V_e$  is the volume of the unit cell,  $\lambda$  the wave length of the electron beam and  $F(\theta)$  is the structure amplitude, with  $\theta = 2\theta_B$  being the scattering angle. Calculating the diffracted intensity leads to the same behaviour for the excitation error  $\mathbf{s}$  as found in equation (2.6):

$$I_g = \frac{\pi^2 \sin^2(\pi t s)}{\xi_g^2 (\pi s)^2}. \quad (2.9)$$

Typical values for the extinction distance  $\xi_g$  are given in table 7.2 of reference [2]. A few of them are exemplarily given here in table 2.1. It can be seen that the extinction distance  $\xi_g$  is material dependent, as well as strongly dependent on the Bragg reflection.

Table 2.1.: Extinction distances  $\xi_g$  in [nm] for electrons with an energy of 100 keV in different elements and for different Bragg reflections. Values taken from [2].

hkl	111	200
Al	56.3	68.5
Cu	28.6	32.6
Ni	26.8	30.6
hkl	110	200
Cr	28.8	42.3
Fe	28.6	41.2

## 2.2. Dynamical theory of diffraction

In order to describe situations typical for TEM experiments, one has to go beyond the description of the kinematic theory of diffraction. Instead, the dynamical diffraction theory has to be used to describe elastic scattering of the electron beam in the sample. The reason for this is the kinematic theory being valid for thin films only. In the kinematic approximation  $I_g = \pi^2 t^2 / \xi_g^2$  holds for the exact Bragg condition ( $s = 0$ ) which results in an untypically large value of  $I_g$  compared to  $I_0$  when the sample thickness is increased. Therefore, in the two-beam case the kinematic theory is applicable for sample thicknesses of  $t < \xi_g/10$ . In the  $n$ -beam case it is restricted to even thinner samples [2]. Typical values for  $\xi_g$  are shown in Table 2.1. For thicker samples (as they are present in the investigations performed in this work) the dynamical theory is used, as it overcomes the aforementioned restrictions. On the one hand, it is possible to formulate this theory as a system of differential equations (done so by Howie and Wheelan [19, 20]). On the other hand, it can be described as an Eigenvalue problem (the Ansatz of Bethe [21]), which is used in the following derivation using the nomenclature given in [2].

The Schrödinger equation for the probe electron has to be solved for a crystal-periodic potential. In a relativistically corrected, stationary form the equation reads [2]:

$$\left[ \frac{\hbar^2}{2m} \nabla^2 + E^* - V(\mathbf{r}) \right] \psi(\mathbf{r}) = 0 \quad \text{with} \quad E^* = E \frac{2E_0 + E}{2(E_0 + E)}, \quad (2.10)$$

while for smaller energies of the electrons the non-relativistic equation can be used.  $E_0$  denotes the rest energy,  $E$  the kinetic energy and  $m$  the relativistic mass of the electron.

Due to its periodicity, the potential  $V(\mathbf{r})$  can be written as a Fourier sum:

$$V(\mathbf{r}) = - \sum_{\mathbf{g}} V_{\mathbf{g}} \exp(i\mathbf{g} \cdot \mathbf{r}) = - \frac{\hbar^2}{2m} \sum_{\mathbf{g}} U_{\mathbf{g}} \exp(i\mathbf{g} \cdot \mathbf{r}). \quad (2.11)$$

The  $\mathbf{g}$  are vectors in the reciprocal space and correspond to points in the reciprocal lattice,  $\mathbf{r}$  are real space vectors. The  $V_{\mathbf{g}}$  and the  $U_{\mathbf{g}}$  can be related to the structure amplitude  $F(\theta)$  and to the extinction distance  $\xi_{\mathbf{g}} = 1/(\lambda U_{\mathbf{g}})$  (see also equation (2.8)). To solve the Schrödinger equation for this problem, equation (2.11) is inserted into equation (2.10) and an Ansatz with plane waves for the wave function that shows the same periodicity of the lattice is made:

$$b_{\mathbf{k}_0}^{(j)}(\mathbf{r}) = \mu^{(j)}(\mathbf{r}) \cdot \exp[i\mathbf{k}_0^{(j)} \cdot \mathbf{r}] \quad (2.12)$$

$$\mu^{(j)}(\mathbf{r}) = \sum_{\mathbf{g}} C_{\mathbf{g}}^{(j)} \cdot \exp[i\mathbf{g} \cdot \mathbf{r}]. \quad (2.13)$$

The solutions are then called Bloch waves:

$$b_{\mathbf{k}_0}^{(j)}(\mathbf{r}) = \sum_{\mathbf{g}} C_{\mathbf{g}}^{(j)} \cdot \exp[i(\mathbf{k}_0^{(j)} + \mathbf{g}) \cdot \mathbf{r}]. \quad (2.14)$$

The sum over  $\mathbf{g}$  covers the infinite number of all reciprocal lattice vectors. In practice the sum is limited to  $n$  excited reflections  $\mathbf{g} = \mathbf{g}_1, \dots, \mathbf{g}_n$  including the beam transmitted in the direction of incidence  $\mathbf{g} = \mathbf{0}$ . The  $C_{\mathbf{g}}^{(j)}$  are called amplitude factors or plane wave amplitudes and the  $\mu^{(j)}(\mathbf{r})$  are referred to as Bloch functions. The  $\mathbf{k}_0^{(j)}$  are the wave vectors of the plane waves and  $\mathbf{k}_{\mathbf{g}}^{(j)} = \mathbf{k}_0^{(j)} + \mathbf{g}$  are the wave vectors of the Bloch waves. The final solution of the Schrödinger equation is itself a superposition of  $j = 1, \dots, n$  Bloch waves

$$\psi_{tot}(\mathbf{r}) = \sum_j \varepsilon^{(j)} b_{\mathbf{k}_0}^{(j)}(\mathbf{r}) \quad (2.15)$$

with amplitudes  $\varepsilon^{(j)}$ , in order to satisfy given boundary conditions at the vacuum-crystal interface. When substituting the formulation of the Bloch waves and the Fourier expansion of the potential into the Schrödinger equation (2.10), together with the abbreviation

$$K = \left[ 2m_0 E \left( 1 + \frac{E}{2E_0} \right) + 2m_0 V_0 \left( 1 + \frac{E}{E_0} \right) \right]^{1/2} \cdot \frac{1}{\hbar} \quad (2.16)$$

for the wave vector inside the crystal, one gets

$$\sum_{\mathbf{g}} \left[ K^2 - (\mathbf{k}_0^{(j)} + \mathbf{g})^2 + \sum_{\mathbf{h} \neq 0} U_{\mathbf{h}} \exp[i\mathbf{h} \cdot \mathbf{r}] \right] \times C_{\mathbf{g}}^{(j)} \cdot \exp[i(\mathbf{k}_0^{(j)} + \mathbf{g}) \cdot \mathbf{r}] = 0. \quad (2.17)$$

For this set of equations all coefficients of the term  $\exp[i(\mathbf{k}_0^{(j)} + \mathbf{g}) \cdot \mathbf{r}]$  have to be zero separately (as it is assumed that the exponential function is non-zero). This leads to the fundamental equations of the dynamical scattering theory

$$\left[ K^2 - (\mathbf{k}_0^{(j)} + \mathbf{g})^2 \right] C_{\mathbf{g}}^{(j)} + \sum_{\mathbf{h} \neq 0} U_{\mathbf{h}} C_{\mathbf{g}-\mathbf{h}}^{(j)} = 0. \quad (2.18)$$

After introducing the approximations

$$K + \left| \mathbf{k}_0^{(j)} + \mathbf{g} \right| \simeq K + k_z^{(j)} \simeq 2K \quad (2.19)$$

and

$$K - \left| \mathbf{k}_0^{(j)} + \mathbf{g} \right| \simeq s_{\mathbf{g}} - (k_z^{(j)} - K) \simeq s_{\mathbf{g}} - \gamma^{(j)} \quad (2.20)$$

(see figure 2.3) one gets for the first factor in equation (2.18):

$$\left[ K^2 - (\mathbf{k}_0^{(j)} + \mathbf{g})^2 \right] = \left( K + \left| \mathbf{k}_0^{(j)} + \mathbf{g} \right| \right) \left( K - \left| \mathbf{k}_0^{(j)} + \mathbf{g} \right| \right) \simeq 2K (s_{\mathbf{g}} - \gamma^{(j)}). \quad (2.21)$$

The approximations (2.19) and (2.20) are justified as  $K \gg g$  holds (for 200 kV electrons the radius of the Ewald sphere is  $1/\lambda \approx 2505 \text{ nm}^{-1}$  compared to  $g_{(\bar{1}11)} \approx 26.1 \text{ nm}^{-1}$  in NiO [2, 3, 15]). With this, the fundamental equations can be formulated as an Eigenvalue problem in matrix form

$$\begin{pmatrix} A_{11} & \dots & A_{1n} \\ \vdots & \ddots & \vdots \\ A_{n1} & \dots & A_{nn} \end{pmatrix} \begin{pmatrix} C_1^{(j)} \\ C_2^{(j)} \\ \dots \\ C_n^{(j)} \end{pmatrix} = \gamma^{(j)} \begin{pmatrix} C_1^{(j)} \\ C_2^{(j)} \\ \dots \\ C_n^{(j)} \end{pmatrix} \quad \text{for } j = 1, \dots, n \quad (2.22)$$

with the matrix elements  $A_{11} = 0$ ,  $A_{gg} = s_{\mathbf{g}}$ ,  $A_{hg}^* = A_{gh} = U_{g-h}/2K = 1/(2\xi_{g-h})$ . The matrix  $\mathbf{A}$  has  $n$  Eigenvalues  $\gamma^{(j)}$  with orthonormal Eigenvectors  $C_{\mathbf{g}}^{(j)}$  with  $j = 1, \dots, n$

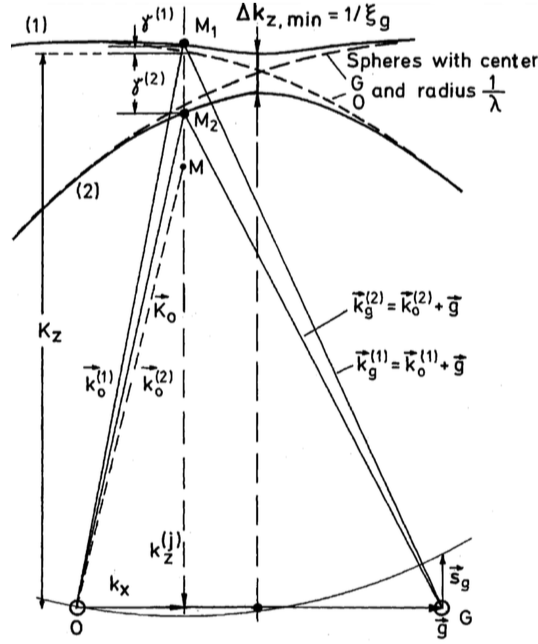


Figure 2.3.: Sketch of the dispersion surface and its construction. Image taken from [2].

and  $\mathbf{g} = \mathbf{g}_1, \dots, \mathbf{g}_n$ . If the matrix  $\mathbf{C}$  and the diagonal matrix  $\{\gamma\}$  are introduced, such that  $C_{gj} = C_g^{(j)}$  and the diagonal elements of  $\{\gamma\}$  are the Eigenvalues  $\gamma^{(j)}$ , the equation (2.22) can be written as:

$$\mathbf{A} \cdot \mathbf{C} = \{\gamma\} \cdot \mathbf{C}. \quad (2.23)$$

The matrix  $\mathbf{A}$  is Hermitian by construction and symmetric for centrosymmetric crystals [2]. The Eigenvectors are orthogonal and satisfy the relations

$$\sum_{\mathbf{g}} C_g^{(i)*} C_g^{(j)} = \delta_{ij}; \quad \sum_j C_g^{(j)*} C_h^{(j)} = \delta_{gh}. \quad (2.24)$$

Each Eigenvalue  $\gamma^{(j)}$  corresponds to a Bloch wave (2.14) with a set of wave vectors  $\mathbf{k}_0^{(j)} + \mathbf{g}$ . The total wave function as a solution to equation (2.10) is a superposition of different Bloch waves with the Bloch wave amplitudes  $\varepsilon^{(j)}$ :

$$\psi_{tot}(\mathbf{r}) = \sum_j \varepsilon^{(j)} b_{\mathbf{k}_0}^{(j)}(\mathbf{r}) = \sum_j \varepsilon^{(j)} \sum_{\mathbf{g}} C_g^{(j)} \exp[i(\mathbf{k}_0^{(j)} + \mathbf{g}) \cdot \mathbf{r}]. \quad (2.25)$$



The amplitude of a reflection  $\mathbf{g}$  can be determined by summing over all  $j = 1, \dots, n$  for the particular lattice point  $\mathbf{g}$ , which leads to

$$\psi_{\mathbf{g}}(\mathbf{r}) = \sum_j \varepsilon^{(j)} C_{\mathbf{g}}^{(j)} \exp[i(\mathbf{k}_0^{(j)} + \mathbf{g}) \cdot \mathbf{r}]. \quad (2.26)$$

The boundary conditions require the incident plane wave in the vacuum and the Bloch waves in the crystal to be continuous, i.e. to be equal at the entrance plane of the specimen, which leads to

$$\begin{aligned} \psi_0(0) &= \sum_j \varepsilon^{(j)} C_0^{(j)} = 1, \\ \psi_{\mathbf{g}}(0) &= \sum_j \varepsilon^{(j)} C_{\mathbf{g}}^{(j)} = 0 \text{ for all } \mathbf{g} \neq 0. \end{aligned} \quad (2.27)$$

Together with the orthogonality relations (2.24) this leads to  $\varepsilon^{(j)} = C_0^{(j)*}$  for normal incidence. For the  $n$ -beam case the equations (2.27) can be written as

$$\mathbf{C} \cdot \boldsymbol{\varepsilon} = \boldsymbol{\psi}(0), \quad (2.28)$$

with  $\boldsymbol{\varepsilon}$  and  $\boldsymbol{\psi}(0)$  being column vectors with  $n$  entries ( $\varepsilon^{(j)}, j = 1, \dots, n$  and  $\psi_{\mathbf{g}}(0), \mathbf{g} = \mathbf{g}_1, \dots, \mathbf{g}_n$ ). When solving equation (2.22) for the 2-beam case, the solutions for the Eigenvalues are:

$$\gamma^{(j)} = \frac{1}{2\xi_g} \left[ w - (-1)^j \sqrt{1 + w^2} \right] \quad (2.29)$$

with  $w = s\xi_g$  characterising the tilt out of the Bragg condition ( $s$  being the excitation error). Using the calculated  $\gamma^{(j)}$ , the amplitudes  $\varepsilon^{(j)} C_{\mathbf{g}}^{(j)} = C_0^{(j)*} C_{\mathbf{g}}^{(j)}$  can be determined:

$$C_0^{(j)*} C_0^{(j)} = \frac{1}{2} \left[ 1 + (-1)^j \frac{w}{\sqrt{1 + w^2}} \right], \quad C_0^{(j)*} C_{\mathbf{g}}^{(j)} = -\frac{1}{2} \frac{(-1)^j}{\sqrt{1 + w^2}}. \quad (2.30)$$

With (2.30) one obtains [2]:

$$\psi_0(t) = \sum_{j=2}^2 C_0^{(j)*} C_0^{(j)} \exp[ik_z^{(j)} t] \quad (2.31)$$

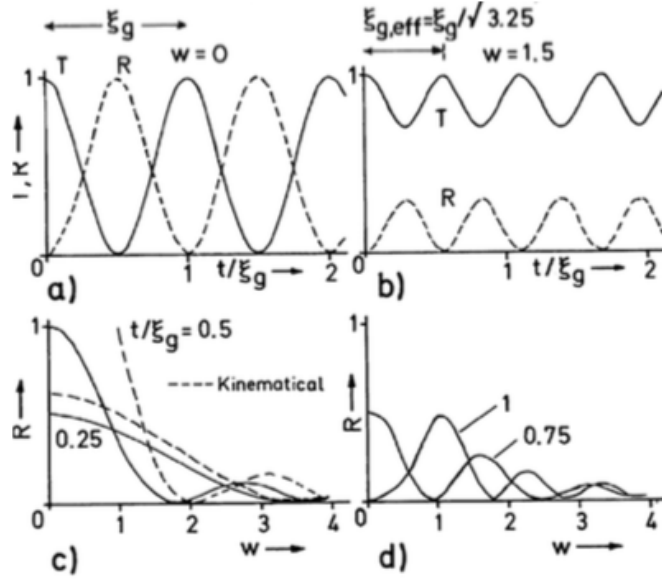


Figure 2.4.: The thickness dependence of the transmitted and reflected beam in a two-beam case. a) The exact Bragg condition is fulfilled ( $w = 0$ ), b) the same for a tilted case. c) and d) shows the intensity of the reflected beam intensity with respect to sample tilt for different sample thicknesses. Image taken from [2].

and

$$\psi_g(t) = \sum_{j=2}^2 C_0^{(j)*} C_g^{(j)} \exp[ik_z^{(j)}t] \cdot \exp[igx]. \quad (2.32)$$

Using (2.29) and (2.30) the reflection  $R$  (intensity of the diffracted beam  $I_g$ ) and transmission  $T$  (intensity of the transmitted beam  $I_0$ ) can be calculated as:

$$R = \psi_g \psi_g^* = 1 - T = 1 - \psi_0 \psi_0^* = \frac{1}{1+w^2} \sin^2 \left( \pi \sqrt{1+w^2} \frac{t}{\xi_g} \right). \quad (2.33)$$

In the exact Bragg condition ( $w = 0$ ) the intensity oscillates between the transmitted and diffracted beam as  $R = \sin^2(\pi t/\xi_g)$ . Thus, the periodicity with respect to the sample thickness is given by the extinction distance  $\xi_g$ , leading to the so-called *Pendellösung* of the dynamical scattering theory (see figure 2.4). For  $w \neq 0$  this periodicity can be described by the effective extinction distance  $\xi_{g,\text{eff}} = \xi_g/\sqrt{1+w^2}$ . The dependence of transmission  $T$  and reflection  $R$  on the sample tilt leads to the so-called “rocking-curves” (see figure 2.4).

---

The n-beam case can be treated by numerically solving equation (2.22). In order to calculate the effects in an experiment using the technique called *Atom Location by Channelling Enhanced Microanalysis* (ALCHEMI, [22]), the treatment of the beam electrons up to now would be sufficient. However, for ELCE experiments, the inelastically scattered electrons of the beam have to be propagated through the crystal until they reach the exit plane of the specimen. In order to facilitate this, one can make use of the reciprocity theorem [23]. This theorem states that one can exchange electron source and detector in an electron microscope when describing the propagation of the electrons, which can be used, for example, when describing the ray paths of a TEM in comparison to a scanning TEM (STEM) [2]. At first sight, it seems that the reciprocity theorem can only be used for the description of elastic scattering, as time inversion symmetry is obvious in this case. Nevertheless, the theorem can be applied to inelastic scattering also, as was shown in [24]. Using the reciprocity theorem for the simulations performed in this work, the outgoing electron wave is again described as a superposition of Bloch waves, defined by the detector position. Similar to the boundary conditions of the incoming wave, the boundary conditions now require for the outgoing wave to be continuous with a plane wave in the vacuum at the exit surface of the crystal. Invoking reciprocity, this corresponds to a plane wave originating from a pointlike detector in the farfield.

## 3. The mixed dynamic form factor

### 3.1. The double differential scattering cross section

Making use of Fermi's golden rule, in first order Born approximation the probability of a transition from an initial state  $|\Psi_i\rangle$  to a final state  $|\Psi_f\rangle$  can be written as [25]:

$$W_{i \rightarrow f} = \frac{2\pi}{\hbar} \left| \langle \Psi_f | \hat{V} | \Psi_i \rangle \right|^2 dv_f \cdot \delta(E_{|f\rangle} - E_{|i\rangle}), \quad (3.1)$$

with the perturbation operator  $\hat{V}$  and  $dv_f$  representing a phase space element around the final state  $|\Psi_f\rangle$ . The system is described in its initial state with energy  $E_{|i\rangle}$  by

$$|\Psi_i\rangle = |\psi_i\rangle \otimes |i\rangle, \quad (3.2)$$

while the final state with energy  $E_{|\Psi_f\rangle}$  is described by

$$|\Psi_f\rangle = |\psi_f\rangle \otimes |f\rangle, \quad (3.3)$$

with  $|\psi_{i,f}\rangle$  being the state of the probe electron and  $|i\rangle, |f\rangle$  the states of the target system. It is assumed that the system can be factorised into eigenstates of the probe electron and the target electron subsystems. This assumption is made due to the large difference in kinetic energy, which allows to neglect exchange and correlation effects between the electrons of the two subsystems [5]. The energy loss  $E$  of the probe is defined by

$$E := E_{|f\rangle} - E_{|i\rangle}, \quad (3.4)$$

hence the transition rate can be written as

$$W_{i \rightarrow f} = \frac{2\pi}{\hbar} \left| \langle \psi_f | \langle f | \hat{V} | i \rangle | \psi_i \rangle \right|^2 dv_f \cdot \delta(E_{|f\rangle} - E_{|i\rangle} - E). \quad (3.5)$$

In a TEM experiment it is assumed that the initial state of the probe is known exactly by preparation of the electron beam and it is possible to measure the final state to a sufficient accuracy. To determine the transition probability without observing the target, the sum over all possible target states is performed, accounting for conservation of energy and averaging over the initial target states with the occupation probabilities  $p_i$ . This leads to the expression:

$$W_{i \rightarrow f} = \frac{2\pi}{\hbar} \sum_i p_i \sum_f \left| \langle \psi_f | \langle f | \hat{V} | i \rangle | \psi_i \rangle \right|^2 dv_f \cdot \delta(E_{|f\rangle} - E_{|i\rangle} - E). \quad (3.6)$$

The differential particle current of free electrons scattered into  $dEd\Omega$  is given by

$$dj = \frac{2\pi}{\hbar} \sum_i p_i \sum_f \left| \langle \psi_f | \langle f | \hat{V} | i \rangle | \psi_i \rangle \right|^2 \frac{k_f m}{\hbar^2} dEd\Omega \cdot \delta(E_{|f\rangle} - E_{|i\rangle} - E), \quad (3.7)$$

as the differential phase space element is given by  $dv_f = k_f^2 dk_f d\Omega$  and using that the energy of free electrons is  $E = \hbar^2 k_f^2 / (2m)$ . It was used that the final probe electron states can be described as plane waves. Here plane wave scattering in a single free atom was assumed. For a more realistic situation, i.e. a Bloch wave scattering on an atom in crystalline environment, see section 3.2.3 and [16]. For a crystal the relativistic mass of the electron is denoted as  $m = \gamma m_e$  and  $k_f$  is the wave vector of the final probe state. The differential scattering cross section measured by the detector is given by

$$dj = d\sigma(E, \Omega) \cdot j_i, \quad (3.8)$$

with  $d\sigma$  being the scattering cross section and  $j_i$  the incident particle current density. Combining (3.7) with (3.8) leads to the double differential scattering cross-section (DDSCS):

$$d\sigma(E, \Omega) = \sum_i p_i \sum_f \left| \langle \psi_f | \langle f | \hat{V} | i \rangle | \psi_i \rangle \right|^2 \frac{2\pi k_f m}{\hbar^3 j_i} dEd\Omega \cdot \delta(E_{|f\rangle} - E_{|i\rangle} - E). \quad (3.9)$$

Assuming that the incoming electrons can also be described as a plane wave, the incident particle current density can be written as

$$j_i = \frac{\hbar k_i}{(2\pi)^3 m} \quad (3.10)$$

with  $k_i$  being the wave vector of the initial probe state, resulting in

$$\frac{\partial^2 \sigma}{\partial E \partial \Omega} = \left( \frac{2\pi}{\hbar} \right)^4 m^2 \frac{k_f}{k_i} \sum_i p_i \sum_f \left| \langle \psi_f | \langle f | \hat{V} | i \rangle | \psi_i \rangle \right|^2 \cdot \delta(E_{|f\rangle} - E_{|i\rangle} - E). \quad (3.11)$$

## 3.2. Models for the DDSCS

### 3.2.1. Single plane wave

The initial and final states of the probe electron are now described as plane waves, as it was already assumed in the previous section. This is justified in a classical setting of scattering experiments, as the electron source, as well as the detector, is placed far away from the scattering centre. Thus, the probe states can be written as

$$|\psi_i\rangle = |\mathbf{k}_i\rangle, \quad |\psi_f\rangle = |\mathbf{k}_f\rangle, \quad (3.12)$$

and projected onto the real space  $\psi_{i,f}(\mathbf{r}) = \langle \mathbf{r} | \psi_{i,f} \rangle$ :

$$\psi_i(\mathbf{r}) = \frac{1}{(2\pi)^{3/2}} \exp[i\mathbf{k}_i \mathbf{r}], \quad \psi_f(\mathbf{r}) = \frac{1}{(2\pi)^{3/2}} \exp[i\mathbf{k}_f \mathbf{r}]. \quad (3.13)$$

The perturbation  $\hat{V}$  is described by the Coulomb interaction potential between the probe electron at position  $\mathbf{r}$  and the target electrons at  $\mathbf{R}_j$  and nuclei at  $\mathbf{a}_k$ :

$$\hat{V} = \frac{1}{4\pi\epsilon_0} \left( \sum_k \frac{-Ze^2}{|\mathbf{r} - \mathbf{a}_k|} + \sum_j \frac{e^2}{|\mathbf{r} - \mathbf{R}_j|} \right). \quad (3.14)$$

Considering the Born-Oppenheimer approximation, the probe electron wave functions are independent of the nuclei wave functions. Thus, only the second term of equation (3.14) has to be considered, leading to

$$\langle \mathbf{k}_f | \langle f | \hat{V} | i \rangle | \mathbf{k}_i \rangle = \frac{e^2}{4\pi\epsilon_0} \sum_j \left\langle f \left| \left( (2\pi)^{-3} \int d^3r e^{-i\mathbf{k}_f \mathbf{r}} \frac{1}{|\mathbf{r} - \mathbf{R}_j|} e^{i\mathbf{k}_i \mathbf{r}} \right) \right| i \right\rangle. \quad (3.15)$$

The integral can be evaluated using the shift theorem for Fourier transformations, yielding

$$\int d^3r e^{-i\mathbf{k}_f \mathbf{r}} \frac{1}{|\mathbf{r} - \mathbf{R}_j|} e^{i\mathbf{k}_i \mathbf{r}} = \int d^3r e^{i\mathbf{Q} \cdot \mathbf{r}} \frac{1}{|\mathbf{r} - \mathbf{R}_j|} = \frac{4\pi}{Q^2} e^{i\mathbf{Q} \cdot \mathbf{R}_j}, \quad (3.16)$$

introducing the scattering vector

$$\mathbf{Q} = \mathbf{k}_i - \mathbf{k}_f. \quad (3.17)$$

The scattering vector consists of the lateral momentum transfer  $\mathbf{q} = (q_x, q_y)$  and the characteristic momentum transfer for inelastic scattering  $q_E$  [15]:

$$\mathbf{Q} = \begin{pmatrix} q_x \\ q_y \\ q_E \end{pmatrix}. \quad (3.18)$$

The characteristic momentum transfer is defined as [3]:

$$q_E = k_0 \frac{E}{E_0} \left( \frac{E_0 + m_e c^2}{E_0 + 2m_e c^2} \right), \quad (3.19)$$

with  $k_0$  being the incoming electron wave vector,  $E$  the investigated energy loss and  $E_0$  the energy of the incoming electrons. For an acceleration voltage of the beam electrons of 200 kV, one gets  $k_0 = 2505 \text{ nm}^{-1}$ . The characteristic momentum transfer for an oxygen K-edge at 531 eV is  $q_E = 4.34 \text{ nm}^{-1}$ .

Using the above results of the evaluation for the Fourier transformation, the DDSCS reads:

$$\begin{aligned} \frac{\partial^2 \sigma}{\partial E \partial \Omega} &= \frac{e^4 m^2}{\hbar^4 \epsilon_0^2 4\pi^2 Q^2} \frac{k_f}{k_i} \sum_i p_i \sum_f \sum_j |\langle f | e^{i\mathbf{Q} \cdot \mathbf{R}_j} | i \rangle|^2 \cdot \delta(E_{|f\rangle} - E_{|i\rangle} - E) \\ &= \frac{4\gamma^2 k_f}{a_0^2 k_i} \sum_i p_i \sum_f \sum_j |\langle f | e^{i\mathbf{Q} \cdot \mathbf{R}_j} | i \rangle|^2 \cdot \delta(E_{|f\rangle} - E_{|i\rangle} - E), \end{aligned} \quad (3.20)$$

with the Bohr radius  $a_0 = \frac{4\pi\epsilon_0 \hbar^2}{m_e e^2}$  and accounting for the relativistic mass correction  $m = \gamma m_e$  using  $\gamma = \frac{1}{\sqrt{1-v_e^2/c^2}} = \frac{1}{\sqrt{1-\beta^2}}$ . It is convenient to introduce another abbreviation:

$$S(\mathbf{Q}, E) = \sum_i p_i \sum_f \sum_j |\langle f | e^{i\mathbf{Q} \cdot \mathbf{R}_j} | i \rangle|^2 \cdot \delta(E_{|f\rangle} - E_{|i\rangle} - E), \quad (3.21)$$

which is called the dynamic form factor (DFF). Inserting equation (3.21) into equa-

tion (3.20) the DDSCS becomes:

$$\frac{\partial^2 \sigma}{\partial E \partial \Omega} = \frac{4\gamma^2 k_f}{a_0^2 k_i} S(\mathbf{Q}, E). \quad (3.22)$$

### 3.2.2. Superposition of plane waves

The initial state of the electron probe is now taken as a superposition of two plane waves, as it is introduced in [5, 6], where the concept of interferometric EELS is described. The initial probe state reads

$$|\psi_i\rangle = a_1 |\mathbf{k}_1\rangle + a_2 |\mathbf{k}_2\rangle, \quad |a_1|^2 + |a_2|^2 = 1, \quad (3.23)$$

while the final probe state  $|\mathbf{k}_f\rangle$  remains a plane wave. Nelhiebel described how a crystalline sample could be used to facilitate such a beam splitting and thus perform interferometric EELS [5]. The sketch shown in figure 3.1 describes the realisation of such a Mach-Zehnder interferometer using the crystal. The DDSCS can then be written as

$$\begin{aligned} \frac{\partial^2 \sigma}{\partial E \partial \Omega} &= \left(\frac{2\pi}{\hbar}\right)^4 m^2 \frac{k_f}{k_i} \sum_i p_i \sum_f \left| \langle \psi_f | \langle f | \hat{V} | i \rangle (a_1 |\mathbf{k}_1\rangle + a_2 |\mathbf{k}_2\rangle) \right|^2 \cdot \delta(E_{|f\rangle} - E_{|i\rangle} - E) \\ &= \left(\frac{2\pi}{\hbar}\right)^4 m^2 \frac{k_f}{k_i} \sum_i p_i \sum_f \left[ |a_1|^2 \left| \langle \mathbf{k}_f | \langle f | \hat{V} | i \rangle |\mathbf{k}_1\rangle \right|^2 + |a_2|^2 \left| \langle \mathbf{k}_f | \langle f | \hat{V} | i \rangle |\mathbf{k}_2\rangle \right|^2 \right. \\ &\quad \left. + 2\Re \left[ a_1 a_2^* \langle \mathbf{k}_f | \langle f | \hat{V} | i \rangle |\mathbf{k}_1\rangle \langle \mathbf{k}_2 | \langle i | \hat{V} | f \rangle |\mathbf{k}_f\rangle \right] \right] \cdot \delta(E_{|f\rangle} - E_{|i\rangle} - E). \end{aligned} \quad (3.24)$$

Inserting the Coulomb interaction by means of equation (3.15) and (3.16) yields

$$\begin{aligned} \frac{\partial^2 \sigma}{\partial E \partial \Omega} &= \frac{4\gamma^2 k_f}{a_0^2 k_i} \sum_i p_i \sum_f \left[ \sum_j \frac{|a_1|^2}{Q^4} \left| \langle \mathbf{k}_f | \langle f | e^{i\mathbf{Q}\cdot\mathbf{R}_j} | i \rangle |\mathbf{k}_1\rangle \right|^2 \right. \\ &\quad \left. + \sum_{j'} \frac{|a_2|^2}{Q'^4} \left| \langle \mathbf{k}_f | \langle f | e^{-i\mathbf{Q}'\cdot\mathbf{R}_{j'}} | i \rangle |\mathbf{k}_2\rangle \right|^2 \right. \\ &\quad \left. + 2\Re \left[ \sum_j \sum_{j'} \frac{a_1 a_2^*}{Q^2 Q'^2} \langle \mathbf{k}_f | \langle f | e^{i\mathbf{Q}\cdot\mathbf{R}_j} | i \rangle |\mathbf{k}_1\rangle \langle \mathbf{k}_2 | \langle i | e^{-i\mathbf{Q}'\cdot\mathbf{R}_{j'}} | f \rangle |\mathbf{k}_f\rangle \right] \right] \\ &\quad \cdot \delta(E_{|f\rangle} - E_{|i\rangle} - E). \end{aligned} \quad (3.25)$$



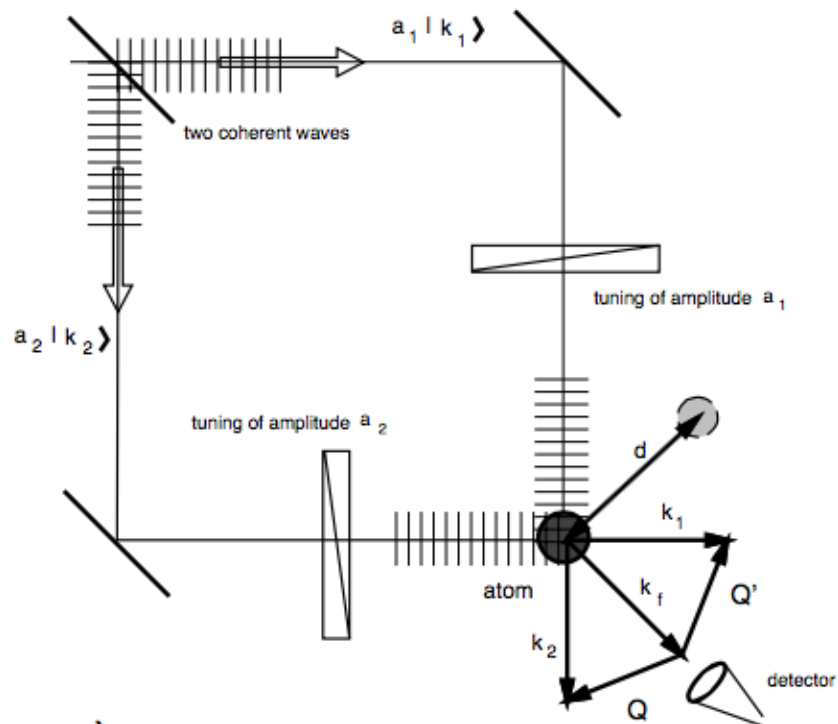


Figure 3.1.: Realisation of a Mach-Zehnder interferometer using a crystalline sample. The beam-splitting is achieved by Bragg diffraction. The distance  $d$  between the atoms would lead to a change of phases in the ionisation process. Sketch taken from [5].

The scattering vectors are defined as

$$\mathbf{Q} = \mathbf{k}_1 - \mathbf{k}_f, \quad \mathbf{Q}' = \mathbf{k}_2 - \mathbf{k}_f. \quad (3.26)$$

Using the definition of the dynamic form factor, equation (3.25) can be rewritten as

$$\begin{aligned} \frac{\partial^2 \sigma}{\partial E \partial \Omega} = & \frac{4\gamma^2 k_f}{a_0^2 k_i} \left[ |a_1|^2 \frac{1}{Q^4} S(\mathbf{Q}, E) + |a_2|^2 \frac{1}{Q'^4} S(\mathbf{Q}', E) \right. \\ & \left. + 2\Re \left[ a_1 a_2^* \frac{1}{Q^2 Q'^2} S(\mathbf{Q}, \mathbf{Q}', E) \right] \right]. \end{aligned} \quad (3.27)$$

In the equation above, the mixed dynamic form factor (MDFF) was introduced:

$$S(\mathbf{Q}, \mathbf{Q}', E) = \sum_i p_i \sum_f \sum_j \langle f | e^{i\mathbf{Q} \cdot \mathbf{R}_j} | i \rangle \sum_{j'} \langle i | e^{-i\mathbf{Q}' \cdot \mathbf{R}_{j'}} | f \rangle \cdot \delta(E_{|f\rangle} - E_{|i\rangle} - E). \quad (3.28)$$

It should be noted that the scattering from different  $|i\rangle$  or to different  $|f\rangle$  is incoherent, but the scattering between different  $\mathbf{Q}$  and  $\mathbf{Q}'$  is incoherent. In principle, the sum over all initial and final states of all atoms has to be included in the MDFF. However, this can be reduced to an incoherent sum over a number of MDFFs, each for a single atom of the crystal. This is due to the fact that the initial states of the target are highly localised in real space and that the MDFF shows the same periodicity as the crystal. This is shown in [23, 26]. Therefore in the following

$$S(\mathbf{Q}, \mathbf{Q}', E) = \sum_i \sum_f \langle f | e^{i\mathbf{Q} \cdot \mathbf{R}} | i \rangle \langle i | e^{-i\mathbf{Q}' \cdot \mathbf{R}} | f \rangle \cdot \delta(E_{|f\rangle} - E_{|i\rangle} - E) \quad (3.29)$$

is used for the MDFF. The DFF can be retrieved by setting  $\mathbf{Q}' = \mathbf{Q}$ , thus leading to  $S(\mathbf{Q}, \mathbf{Q}, E) = S(\mathbf{Q}, E)$ . The DFF can be interpreted as the diagonal elements of the MDFF, with the off-diagonal elements describing the influence of interference effects on the measured signal. To calculate this influence, in [5] the expression

$$\frac{\partial^2 A}{\partial E \partial \Omega} = \frac{4\gamma^2 k_f}{a_0^2 k_i} \frac{S_j(\mathbf{Q}, \mathbf{Q}', E)}{Q^2 Q'^2} \quad (3.30)$$

was introduced. There are some useful properties of the MDFF derived in [6] and summarised in [23]:

- it is hermitian:  $S(\mathbf{Q}, \mathbf{Q}', E)^* = S(\mathbf{Q}', \mathbf{Q}, E)$ ,

- for targets with inversion symmetry  $S(\mathbf{Q}, \mathbf{Q}', E) = S(-\mathbf{Q}, -\mathbf{Q}', E)$  holds,
- if the target is invariant under time-reversal transformation, the MDFF obeys the rule  $S(\mathbf{Q}, \mathbf{Q}', E) = S(-\mathbf{Q}', -\mathbf{Q}, E)$ .

### 3.2.3. Bloch waves

Using the Bloch wave formalism, the wave function of the incoming electron wave in a periodic crystal can be described by [2]:

$$\psi(\mathbf{r}) = \sum_j \sum_{\mathbf{g}} \varepsilon^{(j)} C_{\mathbf{g}}^{(j)} \cdot \exp[i(\mathbf{k}_0^{(j)} + \mathbf{g}) \cdot \mathbf{r}] \quad (3.31)$$

and the outgoing electron wave by:

$$\tilde{\psi}(\mathbf{r}) = \sum_l \sum_{\mathbf{h}} \tilde{\varepsilon}^{(l)} \tilde{C}_{\mathbf{h}}^{(l)} \cdot \exp[i(\mathbf{k}_0^{(l)} + \mathbf{h}) \cdot \mathbf{r}]. \quad (3.32)$$

This is a generalisation of what is given in section 3.2.2. More details on the Bloch wave formalism can be found in section 2.2. The momentum transfer vectors become

$$\mathbf{Q} = \mathbf{Q}_{\mathbf{g}\mathbf{h}}^{jl} = (\mathbf{k}_0^{(j)} + \mathbf{g}) - (\mathbf{k}_0^{(l)} + \mathbf{h}) = \mathbf{k}_0^{(j)} - \mathbf{k}_0^{(l)} + \mathbf{g} - \mathbf{h} \quad (3.33)$$

and

$$\mathbf{Q}' = \mathbf{Q}_{\mathbf{g}'\mathbf{h}'}^{j'l'} = \mathbf{k}_0^{(j')} - \mathbf{k}_0^{(l')} + \mathbf{g}' - \mathbf{h}'. \quad (3.34)$$

The Bloch wave vectors inside the crystal fulfill the condition

$$\mathbf{k}_0^{(j)} = \mathbf{k} + \gamma^{(j)} \cdot \mathbf{n}, \quad (3.35)$$

with  $\mathbf{n}$  the surface normal vector of the crystal surface and  $\mathbf{k}$  the wave vector of the incoming electron wave and  $\gamma^{(j)}$  called ‘‘Anpassung’’. Using these formulas in equation (3.20), the double differential scattering cross section becomes:

$$\frac{\partial^2 \sigma}{\partial E \partial \Omega} = \frac{4\gamma^2 k_f}{a_0^2 k_i} \sum_{\mathbf{x}} \sum_{\substack{j,j',l,l' \\ \mathbf{g},\mathbf{g}',\mathbf{h},\mathbf{h}'}} X_{\mathbf{g}\mathbf{h}\mathbf{g}'\mathbf{h}'}^{jlj'l'}(\mathbf{x}) \frac{S_{\mathbf{x}}(\mathbf{Q}, \mathbf{Q}', E)}{Q^2 Q'^2}, \quad (3.36)$$

with  $\mathbf{k}_i$  the incoming and  $\mathbf{k}_f$  the outgoing electron wave vector and

$$X_{\mathbf{g}\mathbf{h}\mathbf{g}'\mathbf{h}'}^{jlj'l'}(\mathbf{x}) = \varepsilon^{(j)} C_{\mathbf{g}}^{(j)} (\tilde{\varepsilon}^{(l)} \tilde{C}_{\mathbf{h}}^{(l)})^* (\varepsilon^{(j')} C_{\mathbf{g}'}^{(j')})^* \tilde{\varepsilon}^{(l')} \tilde{C}_{\mathbf{h}'}^{(l')} \cdot e^{i(\mathbf{Q}-\mathbf{Q}')\cdot\mathbf{x}} \cdot e^{id(\tilde{\gamma}^{(l)}-\tilde{\gamma}^{(l')})} \quad (3.37)$$

includes all the prefactors of the incoming and outgoing Bloch waves. The vectors  $\mathbf{x}$  denote the positions of the target atoms in the sample where the inelastic scattering process occurs. Thus,  $S_{\mathbf{x}}(\mathbf{Q}, \mathbf{Q}', E)$  describes the MDFF for each of the target atoms. The summation over all reciprocal vectors and Bloch wave indices ensure that not only the indirect terms (MDFF) are included in equation (3.36), but also the direct terms (DFF). For equation (3.36) a boundary condition for the Bloch waves was used, such that at the crystal surfaces they are described as plane waves. Furthermore, the reciprocity theorem was invoked, describing the outgoing wave as the solution of the time inverted Schrödinger equation with the EELS detector taking the place of the electron source [27]. More details can be found in [9].

### 3.3. The MDFF for crystals

In order to actually calculate the DDSCS, one needs a description of the MDFF suitable for the considered problem. This task comes down to describing the initial and final states  $|i\rangle, |f\rangle$  of the target, which is usually a crystalline TEM sample. As in core-loss EELS the initial states are highly localised at the atomic nuclei, it is favourably to work with spherical harmonics centered at the atomic positions. Thus, the exponential functions can be rewritten using the Rayleigh expansion [23]:

$$e^{i\mathbf{Q}\mathbf{R}} = 4\pi \sum_{\lambda=0}^{\infty} \sum_{\mu=-\lambda}^{\lambda} i^{\lambda} Y_{\lambda}^{\mu}(\mathbf{Q}/Q) Y_{\lambda}^{\mu}(\mathbf{R}/R) j_{\lambda}(QR), \quad (3.38)$$

with  $Y_{\lambda}^{\mu}$  the spherical harmonics and  $j_{\lambda}$  the spherical Bessel function of first kind. The MDFF then reads:

$$S(\mathbf{Q}, \mathbf{Q}', E) = 16\pi^2 \sum_{\lambda\lambda'} i^{\lambda-\lambda'} \sum_{\mu\mu'} \sum_i p_i \sum_f Y_{\lambda}^{\mu}(\mathbf{Q}/Q) Y_{\lambda'}^{\mu'}(\mathbf{Q}'/Q') \times \\ \langle f | Y_{\lambda}^{\mu}(\mathbf{R}/R) j_{\lambda}(QR) | i \rangle \langle i | Y_{\lambda'}^{\mu'}(\mathbf{R}/R) j_{\lambda'}(Q'R) | f \rangle \delta(E_{|f\rangle} - E_{|i\rangle} - E). \quad (3.39)$$

For crystal wave functions, which are the most suitable description for the work presented here, the initial state can be described as follows [23]:

$$\begin{aligned}
|i\rangle &= |n, l, 1/2, j, j_z\rangle \\
&= \sum_{ms} |n, l, m, 1/2, s\rangle \langle l, m, 1/2, s | j, j_z\rangle \\
&= \sum_{ms} (-1)^{-l+\frac{1}{2}-j_z} \sqrt{2j+1} \begin{pmatrix} l & \frac{1}{2} & j \\ m & s & -j_z \end{pmatrix} |n, l, m, 1/2, s\rangle. \tag{3.40}
\end{aligned}$$

The initial states are eigenstates of the total angular momentum operator and typically the overlap of the core states of neighbouring atoms is negligible. The unoccupied final states are usually found in the conduction band. They are described using the set of quantum numbers  $|\nu\rangle$ , which in the band structure formalism contains the band index and the wave number. For the matrix elements appearing in the MDFF, only the part of the final states that shows significant overlap with the initial states is of importance. Therefore, the muffin-tin approximation as used in the DFT simulation software WIEN2k [12] can be applied. In this case, the final states are expanded into eigenstates of the angular momentum:

$$|\nu\rangle = \sum_{LMS} D_{LMS}^\nu(E_\nu) |\nu, L, M, 1/2, S\rangle. \tag{3.41}$$

For the actual calculation of the MDFF, the initial and final states are usually projected onto the real space, leading to:

$$\begin{aligned}
\langle \mathbf{R} | n, l, m \rangle &= u_l(R) Y_l^m(\mathbf{R}/R) \\
\langle \mathbf{R} | \nu, L, M \rangle &= u_L(R) Y_L^M(\mathbf{R}/R), \tag{3.42}
\end{aligned}$$

with  $u_l(R)$  and  $u_L(R)$  being radial wave functions. For possible models and approximations how to calculate these wave functions in a simulation, see [12, 13, 15]. Linking the description of the final states in equation (3.41) to the formalism used in WIEN2k leads to the result that the local charge density with  $L, M$  character in the atomic sphere centered around the atom with index  $t$  can be written as

$$\rho_{\nu, L, M, S}^t(\mathbf{R}) = |D_{LMS}^{\nu, t}(E_\nu) u_L(E_\nu, R) Y_L^M(\mathbf{R}/R)|^2. \tag{3.43}$$

The local partial charge can be obtained by integration over the sphere  $t$ :

$$q_{\nu,L,M,S}^t = |D_{LMS}^{\nu,t}(E_{\nu})|^2. \quad (3.44)$$

The local partial density of states (DOS) is calculated by summing over all partial charges for the same energy  $E$  but different band states  $\nu$ :

$$\chi_{LMS}^t(E) = \sum_{\nu} |D_{LMS}^{\nu,t}(E_{\nu})|^2 \delta(E - E_{\nu}). \quad (3.45)$$

Inserting the assumptions for the initial and final states into equation (3.39) and following the elucidations in [23], one arrives at the following evaluation of the MDF:

$$\begin{aligned} S(\mathbf{Q}, \mathbf{Q}', E) = & \sum_{\nu} \sum_{mm'} \sum_{\lambda\lambda'} \sum_{\mu\mu'} \sum_{LMS} \sum_{L'M'S'} i^{\lambda-\lambda'} 4\pi(2l+1) \times \\ & \sqrt{(2L+1)(2L'+1)(2\lambda+1)(2\lambda'+1)} \times \\ & Y_{\lambda}^{\mu}(\mathbf{Q}/Q)^* \langle j_{\lambda}(Q) \rangle_{\nu n j L S} Y_{\lambda'}^{\mu'}(\mathbf{Q}'/Q') \langle j_{\lambda'}(Q') \rangle_{\nu n j L' S'} \times \\ & \begin{pmatrix} L & \lambda & l \\ 0 & 0 & 0 \end{pmatrix} \begin{pmatrix} L' & \lambda' & l \\ 0 & 0 & 0 \end{pmatrix} \begin{pmatrix} L & \lambda & l \\ -M & \mu & m \end{pmatrix} \begin{pmatrix} L' & \lambda' & l \\ -M' & \mu' & m' \end{pmatrix} \times \\ & \sum_{j_z} (-1)^{M+M'} (2j+1) \begin{pmatrix} l & \frac{1}{2} & j \\ m & S & -j_z \end{pmatrix} \begin{pmatrix} l & \frac{1}{2} & j \\ m' & S' & -j_z \end{pmatrix} \times \\ & (D_{LMS}^{\nu})^* (D_{L'M'S'}^{\nu}) \delta(E_{|f} - E_{|i} - E). \end{aligned} \quad (3.46)$$

In this context, it is noteworthy to mention the definition of the cross density of states (XDOS) in comparison with the DOS given in equation (3.45):

$$X_{LMS,L'M'S'}(E) := \sum_{\nu} (D_{LMS}^{\nu})^* D_{L'M'S'}^{\nu} \delta(E - E_{\nu}). \quad (3.47)$$

The existence of  $L, M, S$  crossterms is related to the fact that the states in the system under investigation can not be described as  $L, M, S$  eigenstate. The above formulas show that usually it is in general not sufficient to use the DOS without the crossterms. However, as the XDOS and thus the appearance of crossterms is dependent on the symmetry of the investigated material as well as the choice of the coordinate system. Thus, a clever choice of the coordinate system can simplify the calculations. For more details on this see [5, 16, 23].

# 4. ELCE

## 4.1. Simulations

In order to illustrate the strong dependence of the results of ELCE measurements on the samples' constituents, simulations for a NiO crystal and a TiO<sub>2</sub> crystal (rutile) are compared. The crystal structures of NiO and rutile are given in table 4.1. The respective Bloch wave amplitudes, as given in equation (2.15), for exact channelling conditions are depicted in figure 4.1. For the calculation of both materials the [110] zone axis was used. A slight tilt out of the zone axis was set up in order to reach exact channelling conditions. A thickness of 70 nm and a superposition of five Bloch waves were used in the calculations. In both cases the Laue circle centre was chosen such that a systematic row condition was obtained. It can be seen that the amplitude shows maxima in the rows containing the heavier element of the structure. Furthermore, a repetition of the amplitude distribution with respect to the sample thickness is evident. It is also visible that for the two materials, the depth at which this repetition starts is different as this phenomenon depends on the extinction distance, which itself is material dependent.

The effect of tilting the sample with respect to the electron beam on the channelling

Table 4.1.: Crystallographic data of NiO and TiO<sub>2</sub> as it was used for the conducted simulations. Data taken from [28].

NiO	Lattice type	Lattice parameters	Atom positions
	R	$a = b = 2.97 \text{ \AA}$ $c = 14.53 \text{ \AA}$ $\alpha = \beta = \gamma = 90^\circ$	Ni <sub>1</sub> : (0 0 0) Ni <sub>2</sub> : (0.5 0.5 0.5) O: (0.25 0.25 0.25)
TiO <sub>2</sub>	Space group	Lattice parameters	Atom positions
	P42/mnm (136)	$a = b = 4.59 \text{ \AA}$ $c = 2.96 \text{ \AA}$ $\alpha = \beta = \gamma = 90^\circ$	Ti: (0 0 0) O: (0.3 0.3 0.3)

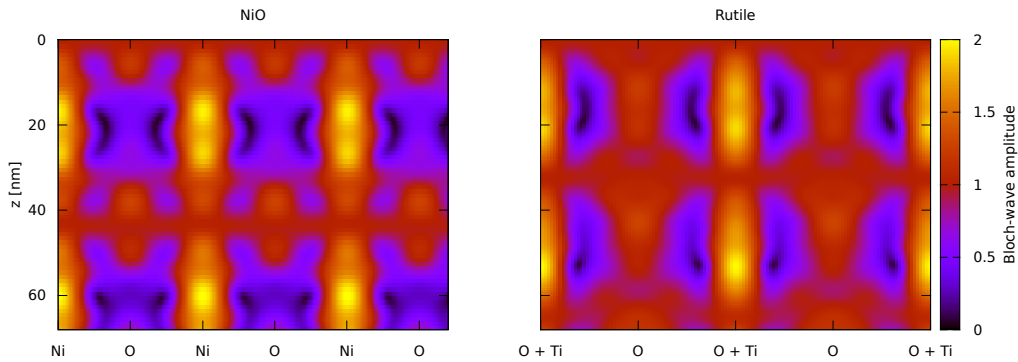


Figure 4.1.: Comparison of the Bloch wave amplitudes, as given in equation (2.15), in NiO and rutile. For both materials the simulations were performed for a sample tilted out of the  $[110]$  zone axis in order to obtain systematic row conditions. The repetition of the amplitude distribution with respect to the  $z$ -axis occurs at different sample depths as it depends on  $\xi_{\mathbf{g}}$  which in turn is material dependent.

conditions is shown in figure 4.2 to figure 4.6. In the first simulation, the Laue circle centre (LCC) is shifted to a position of  $(00\bar{20})$  in order to obtain a systematic row condition. In the subsequent simulations the position of the Laue circle centre was changed along the systematic row in order to simulate sample tilt. Depicted are the results of simulations where the LCC was shifted 0.25, 0.5, 0.75 and 1.0 of the distance between the  $\mathbf{0}$  and the  $\mathbf{G}$  reflection. The change in the amplitude distribution and thus the change in the channelling conditions is evident. Furthermore, it becomes clear that the change of the channelling effects with respect to sample tilt is not straightforward to interpret. Even more, as for interferometric EELS experiments not only the incoming wave has to be taken into account but also the outgoing wave, which itself shows different channelling conditions in general.

In figure 4.7 to figure 4.10 the hypothetical inelastic scattering intensity distribution is shown with respect to different channelling conditions. These simulations illustrate, how much an atom at a certain position inside the unit cell would contribute to the measured EELS signal, if a respective elemental edge would be investigated. The change in channelling conditions were achieved by changing the position of the spectrometer with respect to the diffraction pattern, thus changing the direction of the outgoing wave. The position of the detector was changed along the systematic row condition between the  $\mathbf{0}$  and the  $\mathbf{G}$  reflection. The results of the simulations with detector positions of 0.25, 0.5,



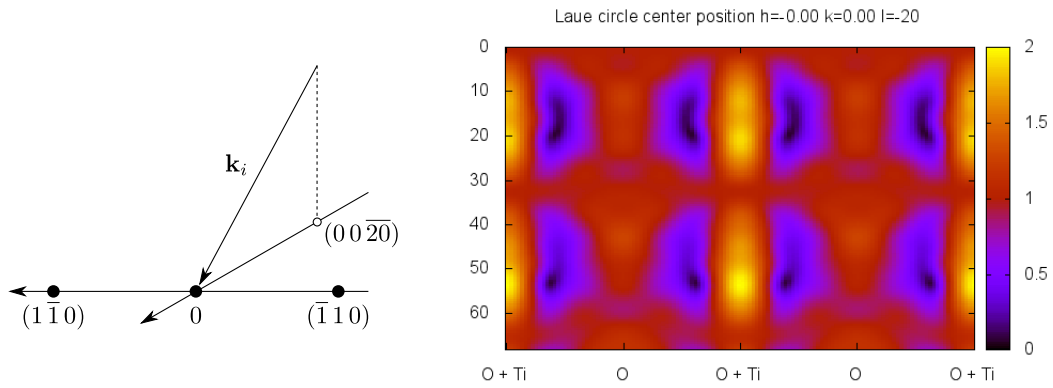


Figure 4.2.: Map of Bloch wave amplitudes in rutile. The sample is tilted out of the  $[1\ 1\ 0]$  zone axis, such that the Laue circle centre position is at  $(0\ 0\ \bar{2}0)$ , in order to obtain systematic row conditions. The plot of the Bloch wave amplitudes is the same as the left part of figure 4.1 and is given here to facilitate comparison with the following figures. On the left hand side, a sketch of the scattering condition used in this simulation is shown.

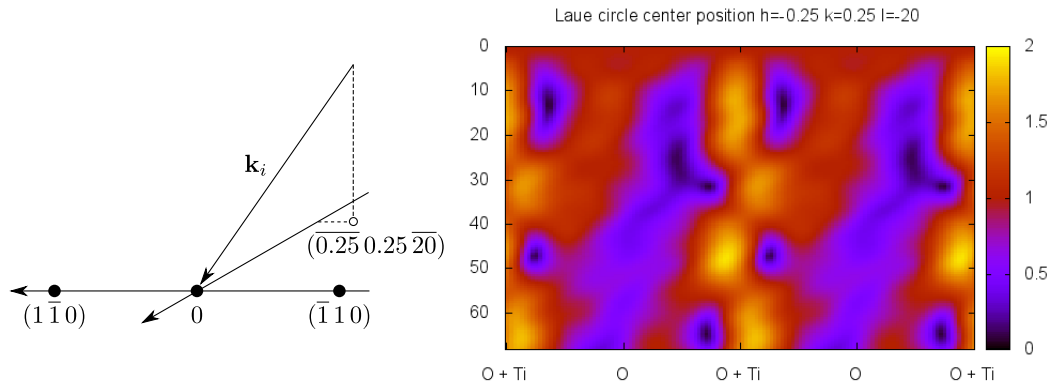


Figure 4.3.: Map of Bloch wave amplitudes in rutile. The Laue circle centre is tilted along the systematic row direction a fourth of the distance between  $0$  and  $G$  spot to change the channelling conditions inside the crystal. On the left hand side, a sketch of the scattering condition for this simulation can be seen.

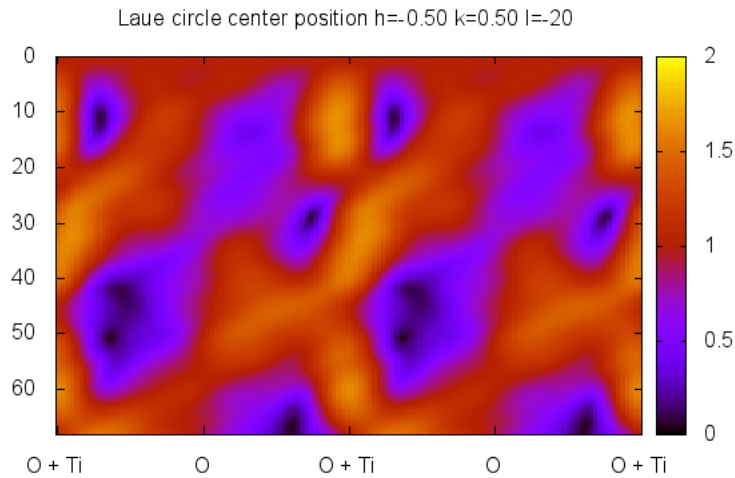


Figure 4.4.: Map of Bloch wave amplitudes in rutile. The Laue circle centre is tilted along the systematic row direction half of the distance between  $\mathbf{0}$  and  $\mathbf{G}$  spot to change the channelling conditions inside the crystal.

0.6 and 0.75 of the mentioned distance are shown. Once again, it is evident that the interpretation of the results would not be that straightforward as it was thought in the beginning of ELCE.

The simulation program used for the calculation of the Bloch wave intensities is described in [11]. It is written in object-oriented C++ code and takes its input parameters from an extensible markup language (XML) configuration file while the output is plain-text based. The different sections of the configuration file specify the crystal parameters as well as the atom positions, the microscope specific values and finally the experimental setup. The program has three possible output modes. The first is to calculate the Bloch wave amplitudes inside the crystal of a specified thickness with a certain position of the Laue circle centre, corresponding to a certain tilt of the sample with respect to the electron beam. The second mode is to calculate some kind of hypothetical intensity map, which describes how much a specific position inside the crystal would contribute to the detected energy-loss signal if there were an atom present at this position (whose electrons could be excited with the given energy-loss of the beam). Additionally to the input values of the first mode, it takes the position of the detector. The position has to

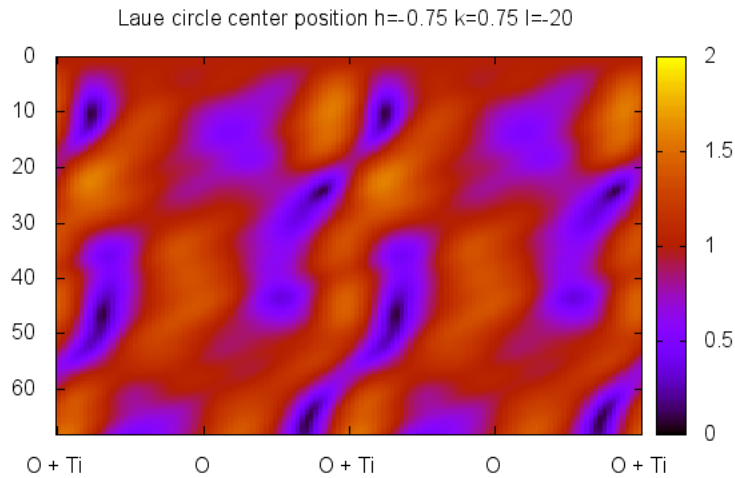


Figure 4.5.: Map of Bloch wave amplitudes in rutile. The Laue circle centre is tilted along the systematic row direction  $3/4$  of the distance between  $\mathbf{0}$  and  $\mathbf{G}$  spot to change the channelling conditions inside the crystal.

be given in a coordinate system that takes the distance between the  $\mathbf{0}$  and  $\mathbf{G}$  reflection as unit distance in x-direction, and the y-direction perpendicular to it. The third mode takes the calculated scattering intensities mentioned above and sums up the contribution at the position of the atoms, which contribute to the scattering process.

The second and third modes take as an input value a switch that controls how the inelastic scattering processes are treated. In early versions of the simulation program, only a simple dipole approximation was implemented [11]. In the current version, it is also possible to use a model for the MDFF that combines the Bloch wave formalism with calculations done using WIEN2k. One has to extract the radial wave functions as well as the XDOS from a WIEN2k calculation. This is done for a specific energy-loss, so it has to be repeated until the full interval of energy-loss one is interested in is covered. The resulting spectrum is unbroadened, utilizing a WIEN2k subroutine instrumental broadening as well as finite lifetime broadening can be accounted for. For details see [12]. Using this procedure, the ELNES affected by the desired channelling conditions can be calculated.

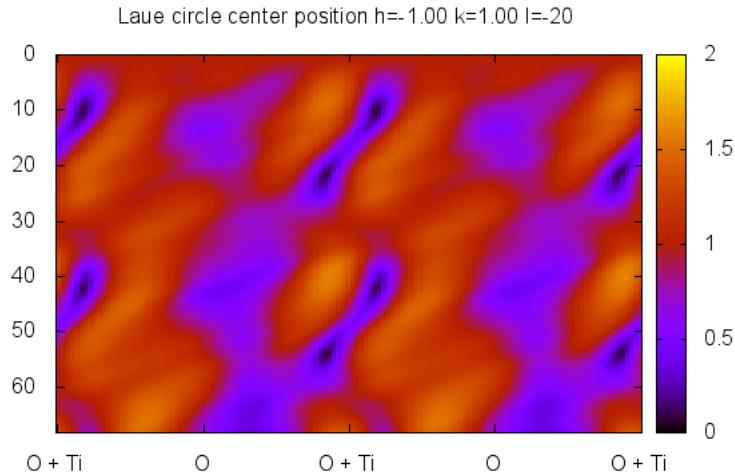


Figure 4.6.: Map of Bloch wave amplitudes in rutile. The Laue circle centre is tilted along the systematic row direction to change the channelling conditions inside the crystal.

## 4.2. Early use of ELCE

Taftø, Spence and Krivanek first combined electron channelling with analytical transmission electron microscopy (TEM) and reported it in a series of papers in 1982 [22, 29–34]. When performing energy dispersive X-ray analysis, the technique was called *Atom Location by Channelling Enhanced Microanalysis* (ALCHEMI) [22] and it was used to identify crystallographic sites of atomic species and for analysing impurities. In combination with EELS the technique was named *energy losses by channelled electrons* (ELCE) [22].

The principle of both techniques is rather simple. The wave function of the probe electrons in the crystal can be described in a Bloch waves basis [1, 18] (see also section 2.2). The Bloch waves differ, in the location of their intensity-maxima. Depending on the orientation of the crystal with respect to the electron beam, these Bloch waves are weighted differently. Thus, the intensity distribution of the electron beam inside the sample shows a distinct pattern of maxima and minima. Whenever the position of an atom coincides with these intensity maxima, the X-ray signal or the energy-loss signal originating from its site will be enhanced (which is then called site-specificity).

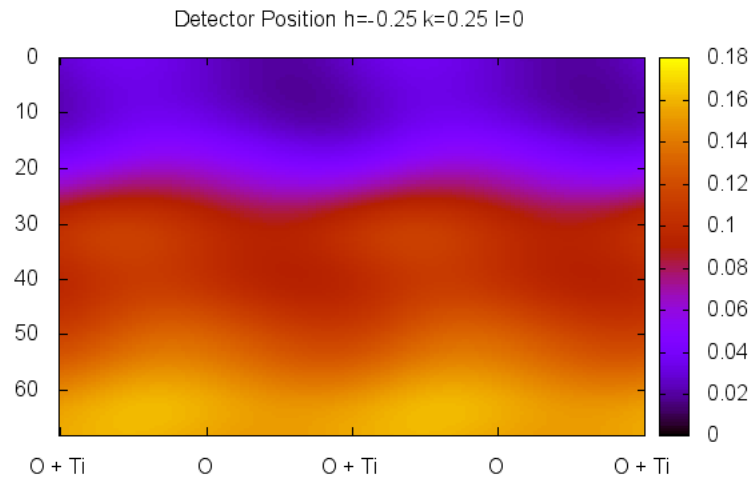


Figure 4.7.: Calculated intensities of inelastic scattering in rutile. The Laue circle centre was placed at  $(00\overline{20})$  and the detector was placed at a point  $1/4$  of the distance between  $\mathbf{0}$  and  $\mathbf{G}$  reflection.

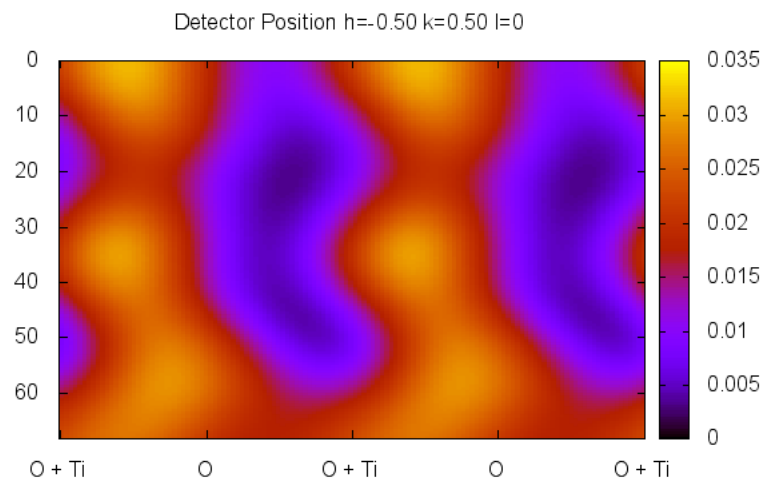


Figure 4.8.: Calculated intensities of inelastic scattering in rutile. The detector was placed at a point  $1/2$  of the distance between  $\mathbf{0}$  and  $\mathbf{G}$  reflection.

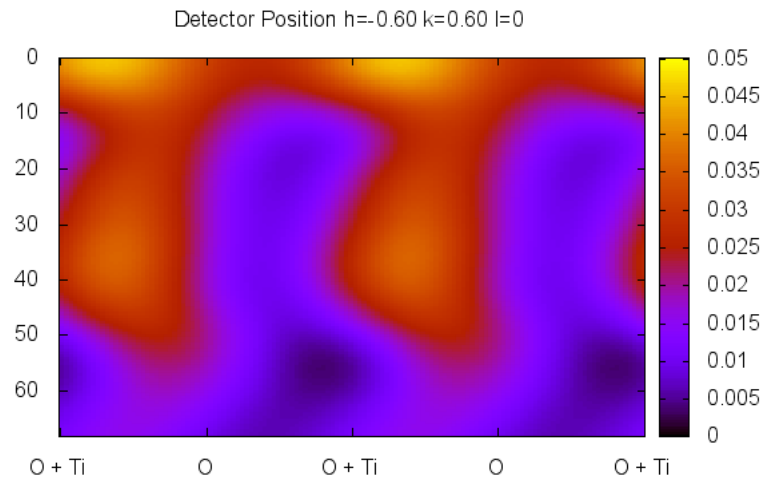


Figure 4.9.: Calculated intensities of inelastic scattering in rutile. The detector was placed at a point 0.6 of the distance between  $\mathbf{0}$  and  $\mathbf{G}$  reflection.

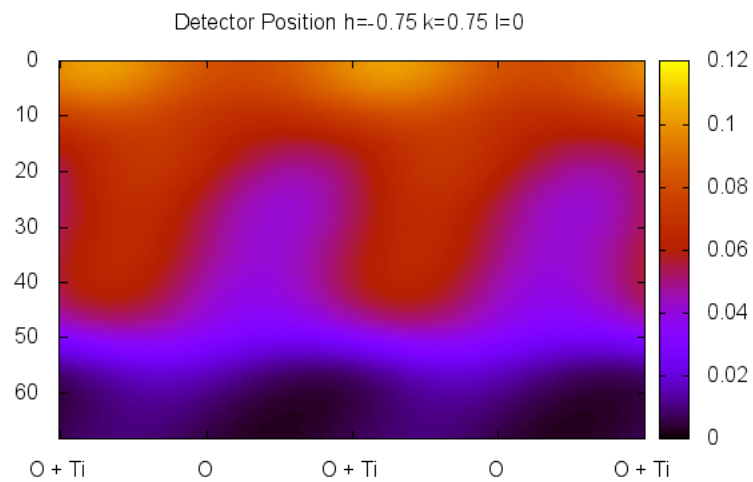


Figure 4.10.: Calculated intensities of inelastic scattering in rutile. The detector was placed at a point  $3/4$  of the distance between  $\mathbf{0}$  and  $\mathbf{G}$  reflection.

ALCHEMI is easier to perform and to interpret than ELCE, as only the incoming electron wave has to be considered. The reason for this being the much weaker interaction of the outgoing characteristic X-rays with the sample material. For ELCE, not only the incoming wave but also the outgoing electron wave, which both undergo inelastic and elastic scattering processes, have to be considered. Thus, the initial enthusiasm with ELCE faded away when it was realised that the detailed description turned out to be more difficult than expected. As the spectrometer is usually placed off axis in ELCE experiments, long acquisition times are necessary and spectra often show a low signal-to-noise (S/N) ratio. Due to these theoretical and instrumental shortcomings, ELCE was not widely used until recently, except for works described by Nüchter and Sigle in 1995 [35–39].

In recent experiments, measurements are usually performed under systematic-row condition in order to have a small definite set of Bragg spots excited which in turn give rise to a small set of significantly excited Bloch waves. Thus, it is easier to get reproducible experimental conditions which allow to compare theory and measurements more easily. The Bloch wave intensity distribution in systematic row conditions has been studied extensively by numerous authors (e.g. [1, 5]). It was found that it is strongly dependent on sample thickness and beam tilt. Hence, numerical simulations for the experimental set of parameters have to be performed to interpret ELCE measurements.

The ELCE technique can be used to study the fine-structure of ionisation edges (ELNES) in detail to investigate atomic orbitals with site-specificity. Nelhiebel investigated the fine-structure by choosing a single (high intensity) direction in the diffraction plane [10]. The experiments shown in the work presented here go beyond Nelhiebel’s approach. By analysing the differences in the site-specific ionisation edge fine-structure for different detector positions, it is possible to probe different orientations of the final state orbitals. It is noteworthy that despite the fact that electron microscopists tend to use the phrase “atomic orbitals” in a crystal environment, due to the band structure formalism applied in the calculations, what is probed in the experiments are rather unoccupied states in energy bands of a certain character (e.g.  $p_x, p_y, p_z$  for O K-edge excitations) above the Fermi level.

## 5. EMCD

### 5.1. The revealing of EMCD and its progress

A common spectroscopic method for investigating magnetic properties is X-ray magnetic circular dichroism (XMCD). This technique relies on the fact that the absorption cross-section for magnetic samples depends on the helicity of the probe. Keeping the similarity of EELS and X-ray absorption spectroscopy (XAS) in mind, one can understand that ELNES and X-ray absorption near edge structures (XANES) give access to the same physical properties. That said, information about the magnetic properties of a sample should be available by means of “dichroic” EELS.

Energy-loss magnetic chiral dichroism was first proposed in 2003 [40], when it was found that one does not need spin-polarised electrons but instead can rely on the equivalence of the polarisation vector  $\boldsymbol{\varepsilon}$  of XAS and the momentum transfer vector  $\mathbf{q}$  of EELS. To gain proof of this equivalency and the proposed EMCD effect, first experiments were conducted 2006 on a Fe-sample in a FEI Tecnai G<sup>2</sup> TF20 TEM at the Vienna University of Technology [41]. For comparison, XMCD measurements were performed on the very same sample.

Soon after the first EMCD experiments, the underlying theoretical description was refined and accompanying simulations were performed [27]. Dynamical diffraction effects were treated using a Bloch wave Ansatz. It was found that these effects can enhance or diminish the measured EMCD signal, bringing a dependence on the sample thickness into the game. The calculation methods were consequently developed and improved [11, 42]. Furthermore, sum-rules which allow the determination of spin and orbital magnetic moments ( $m_s$  and  $m_l$ ) were derived [43, 44]. Due to the dynamical diffraction effects, calculating  $m_l$  and  $m_s$  separately would require the exact knowledge of all information related to these dynamical effects [44]. Therefore, it is more reasonable to determine the fraction  $m_l/m_s$ , which is independent of the dynamical diffraction effects.



On the experimental side, in the years after the first EMCD measurements, the challenge was to drive the spatial resolution to better values. Starting from a resolution of 200 nm, it was pushed down to 10 nm using a Co sample [45] and further to 2 nm [46] using a sample consisting of subsequent Fe and Au layers of variable layer-thickness. In recent years, the interest went on to techniques beyond “standard” EMCD, like energy filtered diffraction patterns [47] and STEM-EMCD [48]. The aim of further increasing spatial resolution to reach atomic resolution would include tuning the electron beam’s wavefront phases by means of a probe  $C_S$ -corrector in a STEM. An actual atomic-resolution STEM-EMCD measurement was reported by [49] but signal to noise ratio is a severe problem for such EMCD experiments. It is noteworthy that most of the reported experimental work on EMCD are some sort of “proof of concept” experiments. Only a few reports exist where EMCD was actually used in the course of material analysis investigation, e.g. [50–52].

## 5.2. Theoretical description

As already mentioned in section 5.1, the theoretical description of EMCD relies on the equivalence of  $\boldsymbol{\varepsilon}$  and  $\mathbf{Q}$ . In a dipole and single particle approximation, the double differential scattering cross-section of EELS reads:

$$\frac{\partial^2 \sigma}{\partial E \partial \Omega} = \sum_{i,f} \frac{4\gamma^2}{a_0^2 q^4} \frac{k_f}{k_i} |\langle f | \mathbf{Q} \cdot \mathbf{R} | i \rangle|^2 \delta(E_i - E_f + E), \quad (5.1)$$

while the absorption cross section of XAS can be written as:

$$\sigma = \sum_{i,f} 4\pi^2 \hbar \alpha \omega |\langle f | \boldsymbol{\varepsilon} \cdot \mathbf{R} | i \rangle|^2 \delta(E + E_i - E_f), \quad (5.2)$$

with  $\alpha = e^2/(4\pi\epsilon_0\hbar c)$  the fine structure constant,  $\boldsymbol{\varepsilon}$  the polarisation vector and  $\omega$  the photon radial frequency [41]. From these two equations, the equivalency of  $\boldsymbol{\varepsilon}$  and  $\mathbf{Q}/Q$  can be seen. One can also understand that there is no need for spin-polarised electrons if it is kept in mind that it is the circular polarised phonons that trigger the excitation in an XMCD experiment by coupling to the angular momentum of the excited atom [45]. Thus, for EMCD, the circular polarisation of the virtual photons [53], which are exchanged in the inelastic electron scattering process, are important [53, 54].

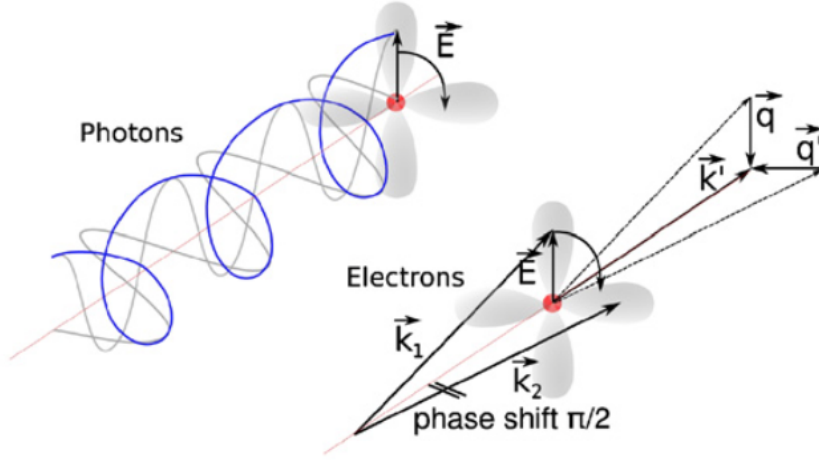


Figure 5.1.: Equivalency of a circular polarised electric field caused by photons and electrons. The phase shift of  $\pm\pi/2$  is induced via Bragg diffraction by the crystal itself. The EELS detector is positioned such that  $\mathbf{q} \perp \mathbf{q}'$ . Taken from [55].

Instead of using (virtual) photons, one can describe the transition process using a circular polarised electric field  $\mathbf{E}$ , which is parallel to the polarisation vector  $\boldsymbol{\varepsilon}$  and antiparallel to the momentum transfer vector  $\mathbf{q}$  [41, 55]. A circular polarised wave can be described by two perpendicular linear polarised waves with a phase shift of  $\pm\pi/2$ . This corresponds to a polarisation vector  $\boldsymbol{\varepsilon} \pm i \cdot \boldsymbol{\varepsilon}'$  with  $\boldsymbol{\varepsilon} \perp \boldsymbol{\varepsilon}'$  and a momentum transfer vector  $\mathbf{q} \pm i \cdot \mathbf{q}'$  with  $\mathbf{q} \perp \mathbf{q}'$ . These relations are depicted in figure 5.1. In EMCD, the phase shift is introduced through the crystal itself by means of Bragg diffraction [9, 41]. A such prepared electron beam would lead to  $a_1 = 1$  and  $a_2 = \pm i$  in equation (3.25) and therefore to:

$$\sigma^\pm = \frac{\partial^2 \sigma}{\partial E \partial \Omega} = \frac{4\gamma^2 k_f}{a_0^2 q^4 k_i} \left[ \frac{1}{Q^4} S(\mathbf{Q}, E) + \frac{1}{Q'^4} S(\mathbf{Q}', E) \pm 2\Im \left[ \frac{1}{Q^2 Q'^2} S(\mathbf{Q}, \mathbf{Q}', E) \right] \right]. \quad (5.3)$$

As becomes clear from equation (5.3), only the part including the MDFF changes when the helicity is reversed. The dichroic signal is defined as the difference of two measurements with reversed helicity. It is usually given as the percentage:

$$\frac{\Delta\sigma}{\sigma} := 2 \cdot \frac{\sigma^+ - \sigma^-}{\sigma^+ + \sigma^-} = 2 \cdot \frac{2\Im [S(\mathbf{Q}, \mathbf{Q}', E)/(Q^2 Q'^2)]}{S(\mathbf{Q}, E)/Q^4 + S(\mathbf{Q}', E)/Q'^4}. \quad (5.4)$$

If the phase shift is not exactly  $\pi/2$ , this corresponds to an elliptically polarised wave.

In such a case, the measured effect as given in equation (5.4) becomes smaller.

In order to take a closer look at the MDFF in a typical EMCD experiment, we recall it being calculated for crystal wave functions in equation (3.46). A fully spin-polarised case is assumed, which would be the case with a material, whose magnetisation is fully saturated in the magnetic field of the objective lens of the TEM. With the magnetic field of almost 2 T in the FEI Tecnai microscope, this is a reasonable assumption for most magnetic materials. The spins are then quantised along the direction of the external magnetic field of the TEM, which is defined as the  $z$ -axis. This leads to [56]:

$$S(\mathbf{Q}, \mathbf{Q}', E) = \sum_{\nu} \sum_L A_{\nu n j L}(E) \cdot \langle j_1(Q) \rangle_{\nu n j L} \langle j_1(Q') \rangle_{\nu n j L} \left( \frac{\mathbf{Q} \cdot \mathbf{Q}'}{QQ'} + i \frac{C_{j l L}}{2} \frac{(\mathbf{Q} \times \mathbf{Q}')_z}{QQ'} \right) \quad (5.5)$$

with

$$A_{\nu n j L}(E) = \frac{3}{2}(2L+1)(2j+1) \begin{pmatrix} L & 1 & l \\ 0 & 0 & 0 \end{pmatrix}^2 |D_L^{\nu}|^2 \delta(E_f - E_i - E) \quad (5.6)$$

and

$$C_{j l L} = \begin{cases} -\left(-\frac{l}{l+1}\right)^{(L-1)\left(\frac{3}{2}-|L-j|\right)} & j, l, L \geq 0, L = l \pm 1, j = l \pm \frac{1}{2}, \\ 0 & \text{otherwise.} \end{cases} \quad (5.7)$$

The two terms in the bracket can be approximated as:

$$\Re[S(\mathbf{Q}, \mathbf{Q}', E)] \propto (\mathbf{Q} \cdot \mathbf{Q}'), \quad (5.8)$$

$$\Im[S(\mathbf{Q}, \mathbf{Q}', E)] \propto (\mathbf{Q} \times \mathbf{Q}') \cdot \frac{\mathbf{M}}{M}, \quad (5.9)$$

with  $\mathbf{M}$  the net magnetic moment of the scattering atom. As mentioned above,  $\frac{\mathbf{M}}{M} = \mathbf{e}_B = \mathbf{e}_z$  holds for a typical EMCD experiment.

Due to the circular polarisation, a selection rule  $\Delta m_l = \pm 1$  is induced in the inelastic scattering process present in EMCD [57, 58]. In virtually all cases the  $L_{2,3}$  edge is investigated, which means that the initial states in the process are  $2p_{1/2}$  and  $2p_{3/2}$  states. Because of the spin-orbit coupling, the states are described using  $|j, m_j\rangle$  as good quantum numbers and  $n = 2$ ,  $l = 1$  and  $s = 1/2$  fixed. This gives rise to the Wigner 3j symbol present in equation (5.6), which has to be used in order to calculate the transition probabilities [57]. Furthermore, one has to keep in mind the difference in the spin-up and spin-down DOS above  $E_F$  in magnetic materials. This gives rise to different intensities in the  $L_2$  and the  $L_3$  edge for measurements with opposite helicity.

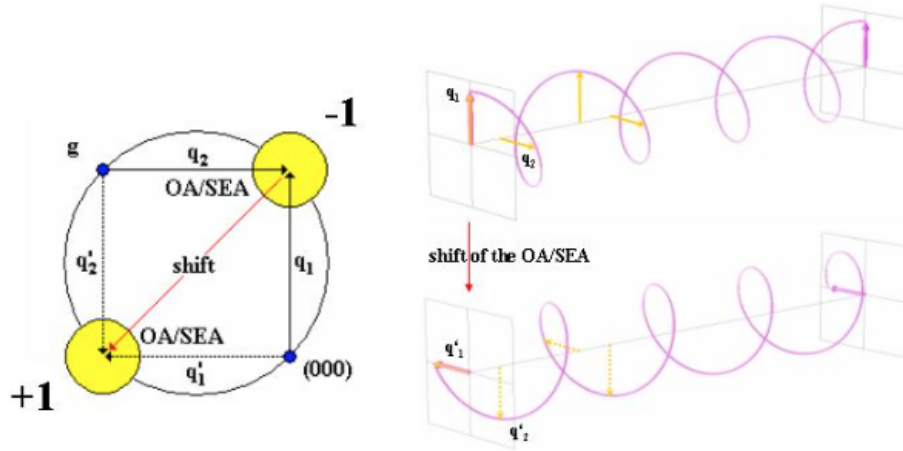


Figure 5.2.: Sketch of the setup for an EMCD experiment using a two-beam case. For the two measurement positions at the Thales-circle the condition  $\mathbf{q} \perp \mathbf{q}'$  and  $q = q'$  holds, and a phase shift of  $\pm\pi/2$  is assumed. This gives opposite helicity for the two measurements. Image taken from [53, 57].

## 5.3. Experimental setup

### 5.3.1. EELS detector setup

As mentioned in the previous section, two perpendicular momentum transfer vectors  $\mathbf{q} \perp \mathbf{q}'$  with a phase shift of  $\pm\pi/2$  are necessary to measure an EMCD effect. To facilitate this in an actual experiment, a basic geometry of a two-beam case with the transmitted beam and an excited  $\mathbf{G}$ -reflection is required. The Bragg diffraction in the crystal itself creates the phase shift between the two beams. Placing the spectrometer entrance aperture on the Thales-circle in the centre of the two reflections would give a condition with the momentum transfer vectors perpendicular and  $q = q'$ . Changing the position of the SEA to its mirrored position using the systematic row defined by  $\mathbf{0}$  and  $\mathbf{G}$  as mirror axis gives the possibility to measure the signal with opposite helicity. A sketch of the two measurement positions as well as the helicity of the electronic excitation is shown in figure 5.2.

It would also be possible to measure an EMCD effect using different positions of the SEA with respect to the Bragg reflections. The only conditions to be kept in mind are  $\mathbf{q} \nparallel \mathbf{q}'$  and the phase shift being different from  $n \cdot \pi$ . Nevertheless, the measured EMCD effect would be smaller than when measured at the optimal positions.

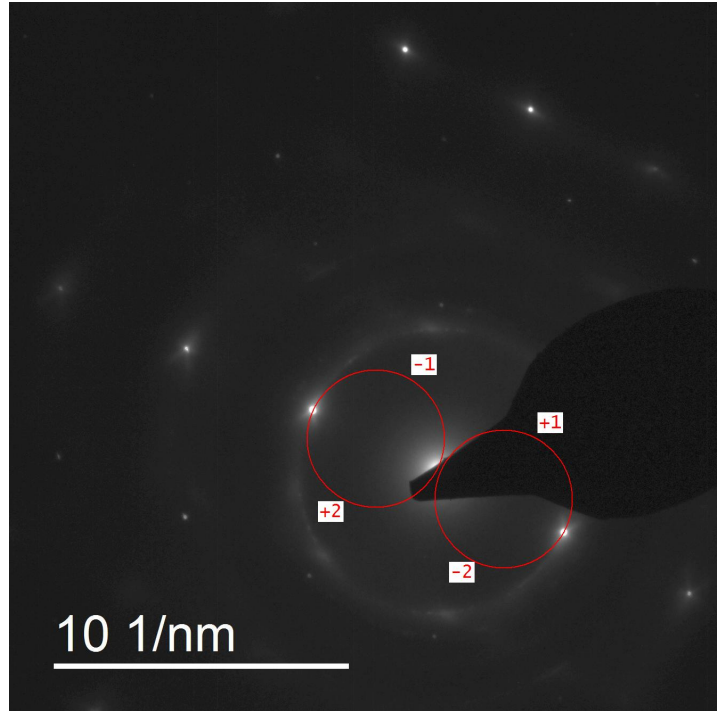


Figure 5.3.: Sketch of the three-beam EMCD setup with the four EMCD positions marked as  $\pm 1$  and  $\pm 2$ .

Another experimental setup uses a systematic row condition in a three-beam case (or even more reflections excited). In this case, there are four positions for the SEA aperture to perform EMCD measurements. A sketch of this setup is shown in figure 5.3. Two positions are on each side of the systematic row, on the Thales-circle amidst the  $\mathbf{0}$  and  $\mathbf{G}$  and amidst the  $\mathbf{0}$  and  $-\mathbf{G}$  reflection, respectively. In an ideal case, two measurement positions, denoted as +1 and +2 as well as -1 and -2 in figure 5.3, would give the same signal at a time. In reality, there exists an asymmetry between the positions at different sides of the systematic row, due to the fact that because of the sample tilt the Laue circle center is positioned at one side of the systematic row. This experimental setup was used for all the measurements reported in this work.

A third method for measuring the EMCD effect makes use of the E-q diagram of the spectrometer. This method allows to acquire the signals with both chiralities at the same time. When switching to the spectrometry mode, the GIF camera records an E-q diagram. The  $q_x$  axis is replaced by the energy-dispersive axis  $E$ , while the  $q_y$  axis is retained. The  $q_x$  information is integrated for each  $q_y$  value. There are two ways to

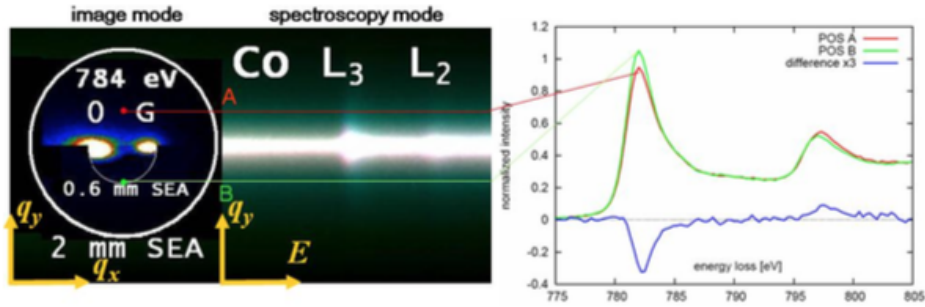


Figure 5.4.: The left part shows an energy filtered diffraction pattern using a slit of 20 eV width at the energy of the Co  $L_{2,3}$  edge. Next to the diffraction pattern the acquired E-q diagram is depicted. The right part shows the acquired EMCD spectra. Images are courtesy of Michael Stöger-Pollach and were taken from [57].

record EMCD spectra using this method. The first one uses a two-beam case with the two reflections aligned parallel to the energy dispersive axis of the EELS spectrometer. The SEA and the camera length are chosen such that both reflections enter the spectrometer. After acquiring the E-q diagram, the EMCD effect can be retrieved by extracting the line spectra at the two EMCD positions from the diagram and comparing them according to equation (5.4). The acquired E-q diagram and EMCD spectra of the Co  $L_{2,3}$  edge using this experimental setup can be seen in figure 5.4. There is another way using a three-beam case. The camera length as well as the size of the SEA are chosen such that the three reflections  $\mathbf{0}$  and  $\pm\mathbf{G}$  enter the spectrometer but now the systematic row including the reflections is set perpendicular to the spectrometer's energy dispersive axis. That way the EMCD positions  $+1$  and  $-1$  from figure 5.3 are measured.

The advantages of the E-q method are that both chiralities can be measured at the same time. This is a huge benefit when investigating a beam sensitive or unstable specimen. Furthermore, the signal-to-noise ratio can be reduced by taking not only one line spectrum for each EMCD position but rather integrating over several lines. A drawback of the method is the need for aligning the diffraction pattern at a certain angle with respect to the energy dispersive axis of the spectrometer. This can be done for example using a rotational sample holder, which would not be available during in-situ investigations using a heating or cooling sample holder. In such cases, one would need to rotate the diffraction pattern using the microscope's projection lens system. This in turn, changes the camera length and also the shape of the beam off the optical axis of

the instrument. One has to keep in mind that the exact effects of changing a single lens of the microscope's lens systems are usually not disclosed due to confidentiality of the manufacturing companies. Some more details on the E-q diagram method can be found in [57].

### 5.3.2. Beam convergence

The theoretical description of EMCD assumes parallel illumination of the sample, as it is used for acquiring diffraction patterns. This would limit the spatial resolution to the size of the used selected area aperture (SAA). In the FEI Tecnai microscopes used in this work, the resolution would therefore be limited to 200 nm. In order to improve not only the spatial resolution but also the signal-to-noise ratio and to gain a higher signal intensity, the beam was somewhat converged on the sample. Thus, the spatial resolution for the reported measurements could be improved such that it was in the region of 10 nm. The convergence was chosen such that the diffraction spots would be smaller than the SEA or the same size at the maximum. This leads to a setting where collection and convergence semi-angle are of the same size about 1 mrad. This setting can be seen in figure 5.5. Changing the convergence of the beam is also altering the positions where the optimal EMCD signal could be recorded. As long as the diffraction spots do not touch each other or even overlap, the standard positions at the Thales-circle are still sufficient. This has also be kept in mind if one uses the scanning mode of the microscope in order to increase spatial resolution. More details on this can be found in section 5.4.2.

In [57] some other acquisition methods, for example the large angle convergent diffraction (LACDIF) and the convergent beam electron diffraction (CBED) method, are described. The CBED method corresponds to the method described above and used throughout this work.

As mentioned in section 5.1, using a converged beam, a spatial resolution down to 2 nm was achieved and discussions are ongoing about how to use aberration-corrected STEM to achieve atomic resolution. It was found that there are two necessary conditions to measure EMCD at the atomic scale [48]: the convergence of the electron beam has to be large enough to create overlapping diffraction discs and the phase of the beam in reciprocal space must not be invariant under the mirror symmetries of the crystal. The second condition can be facilitated by shaping the electron beam using a probe  $C_s$ -

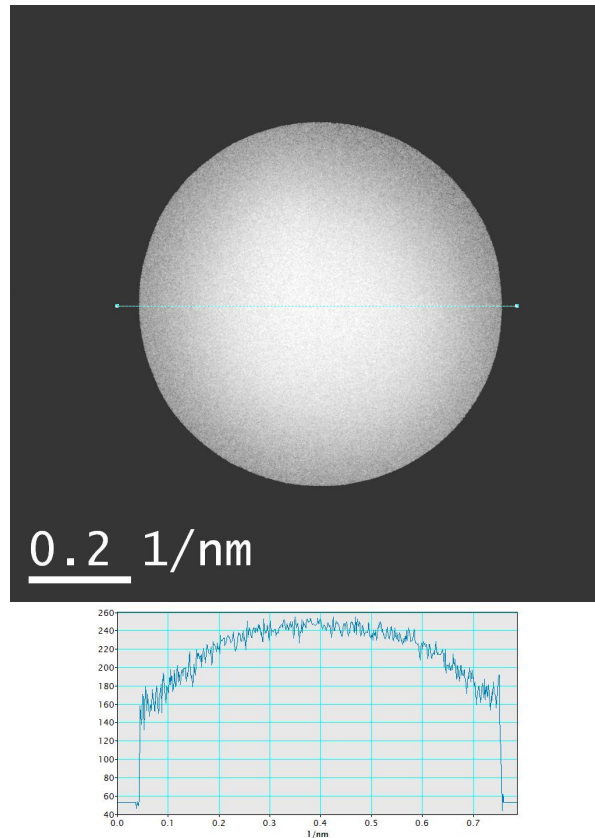


Figure 5.5.: Image of the  $\mathbf{0}$ -reflection with the SEA visible as circular aperture limiting the momentum transfer to  $q \leq 0.35 \text{ nm}^{-1}$ . The collection and convergence semi-angle was  $0.9 \text{ mrad}$ . The bottom part of the figure shows a linescan of the intensity across the aperture.



corrector. Another approach to perform atomic resolution EMCD experiments includes the generation of electron vortex beams, which are carrying orbital angular momentum, using a phase mask. This Ansatz is described for example in [59]. A third way of achieving such a high resolution when mapping spin-polarised transition was reported in [49]. This experiment was performed at the SuperSTEM laboratory in Daresbury. While scanning across the atomic positions, an energy-filtered diffraction pattern would change its shape. By recording these intensity modulations, one could retrieve information about the spin-polarised transition process. Nevertheless, the latter experiment as well as experiments including the generation of vortex beams, suffer from a lack of signal intensity. Thus, beam damage of the sample and the stability of the microscope are crucial effects and have to be dealt with.

## 5.4. Simulations

### 5.4.1. Thickness dependence of the EMCD signal

As shown in section 4.1, dynamical diffraction effects can have a huge impact on EELS measurements. Not only channelling experiments are influenced by these effects, but also EMCD measurements. Therefore, simulations of the EMCD effect as a function of sample thickness were performed for different materials. A list of the calculated materials is given in table 5.1. For the simulations the Bloch wave software package described in [11] was used. A short description of its abilities is also given in [15].

In the input file the crystal structure of the investigated material was given, as well as the experimental settings, which includes zone axis, Laue circle centre and which reflection of the systematic row was used as reference point for the EMCD measurement positions. The given reflection acts as the  $\mathbf{G}$ -reflection, as shown in figure 5.3, in which the four EMCD positions are also shown. Furthermore, the number of incoming and outgoing Bloch waves was chosen. For all simulations 3 incoming and 4 outgoing Bloch waves were used. Increasing the number of Bloch waves does not change the results but results only in higher calculation time. Finally, the calculation of a “thickness map” was set up, using a sample thickness of up to 80 nm and the elemental edge for which the EMCD signal is to be calculated was chosen. To calculate the EMCD signal, the two measurement positions denoted in figure 5.3 as +1 and -1 were used.

Table 5.2 gives the experimental conditions used in the simulations, while figure 5.6

Table 5.1.: Crystal structure of the simulated materials. The structure is taken from [28], the lattice parameter was determined experimentally via diffraction experiments. Details are given in section 6.5.

Material	Space group	$a_{cub}$	Element	Wyckoff position
Ni <sub>2</sub> MnIn	225 $Fm\bar{3}m$	0.607 nm	Ni	8c
			Mn	4b
			In	4a
Ni <sub>2</sub> MnSn	225 $Fm\bar{3}m$	0.599 nm	Ni	8c
			Mn	4b
			Sn	4a
Ni <sub>2</sub> MnGa	225 $Fm\bar{3}m$	0.578 nm	Ni	8c
			Mn	4b
			Ga	4a
Co <sub>2</sub> MnSi	225 $Fm\bar{3}m$	0.565 nm	Co	8c
			Mn	4b
			Si	4a
Co <sub>2</sub> CrAl	225 $Fm\bar{3}m$	0.573 nm	Co	8c
			Cr	4b
			Al	4a

to 5.15 show the resulting thickness dependence of the EMCD signal as given in equation (5.4). It can be seen that for different systematic row conditions the thickness dependence is quite different. In all simulations it can be seen that the EMCD signal can be enhanced or decreased due to the effects of dynamical diffraction. Taking Ni<sub>2</sub>MnIn as an example, in zone axis [001] using a systematic row condition including the (200) reflection, the Ni and Mn EMCD signals show a quite large window of sample thickness in which an optimal effect can be measured. Furthermore, the sign of the signal is reversed for the two elements. Only at a very small sample thickness and at about 65 nm the EMCD signal is diminished or even vanishes. Upon further increasing the sample thickness, the EMCD signal changes its sign. Taking a look on the simulation using the (220) reflection in the systematic row, the EMCD signal is similar for both elemental edges. In contrast to the first simulation, the latter shows a quite large variation of the signal with respect to the sample thickness. The periodicity of between signal maxima and minima is  $\sim 20$  nm. EMCD measurements at sample thicknesses corresponding to signal maxima would reveal a clearly positive EMCD signal while those at the minima would reveal a very small but negative EMCD signal. These results resemble the differ-

Table 5.2.: Scattering conditions used for the simulations shown in this section. The column “ $\mathbf{G}$ -reflection” denotes the reflection which was included in the respective systematic row and used as reference to define the positions of the EMCD measurements.

Zone axis	Laue circle centre	$\mathbf{G}$ -reflection
[0 0 1]	(0 1 2 0)	(2 0 0)
	( $\bar{1}$ 2 1 2 0)	(2 2 0)
[1 1 0]	( $\bar{1}$ 2 1 2 0)	(0 0 2)
	(0 0 1 2)	(2 $\bar{2}$ 0)
	(6 $\bar{6}$ 1 2)	( $\bar{1}$ 1 1)

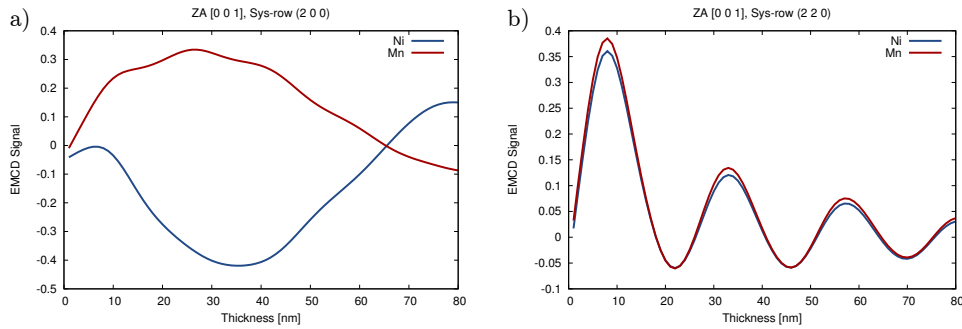


Figure 5.6.: Simulation of the EMCD signal, as defined in equation (5.4), as a function of the sample thickness. A Ni<sub>2</sub>MnIn sample with zone axis [0 0 1] and a systematic row condition including the a) (2 0 0), b) (2 2 0) reflection was used.

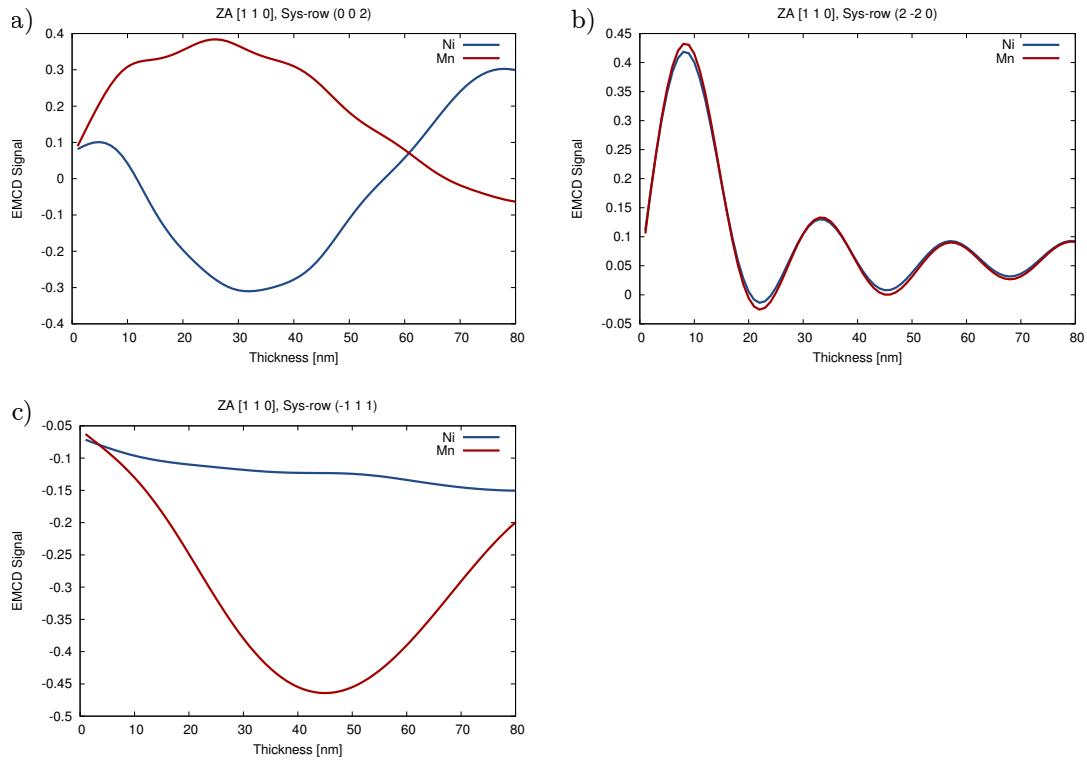


Figure 5.7.: Simulation of the EMCD signal, as defined in equation (5.4), as a function of the sample thickness. A  $\text{Ni}_2\text{MnIn}$  sample with zone axis  $[1\ 1\ 0]$  and a systematic row condition including the a)  $(0\ 0\ 2)$ , b)  $(2\ \bar{2}\ 0)$ , c)  $(\bar{1}\ 1\ 1)$  reflection was used.

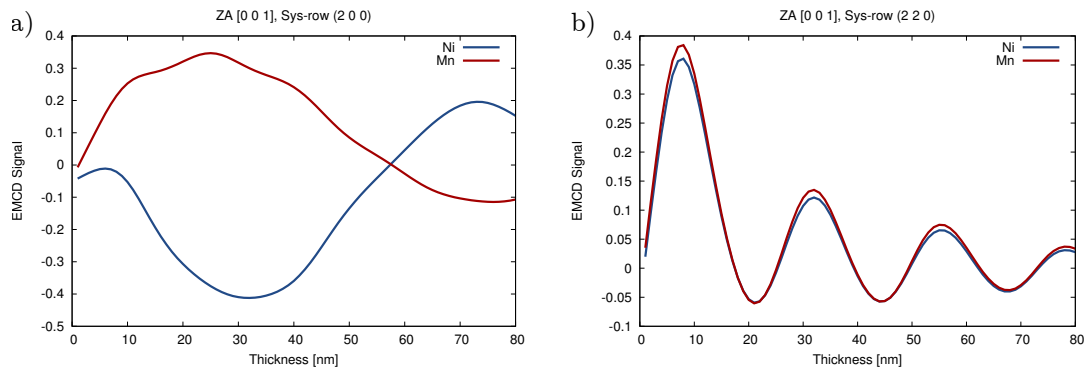


Figure 5.8.: Simulation of the EMCD signal, as defined in equation (5.4), as a function of the sample thickness. A  $\text{Ni}_2\text{MnSn}$  sample with zone axis  $[0\ 0\ 1]$  and a systematic row condition including the a)  $(2\ 0\ 0)$ , b)  $(2\ 2\ 0)$  reflection was used.

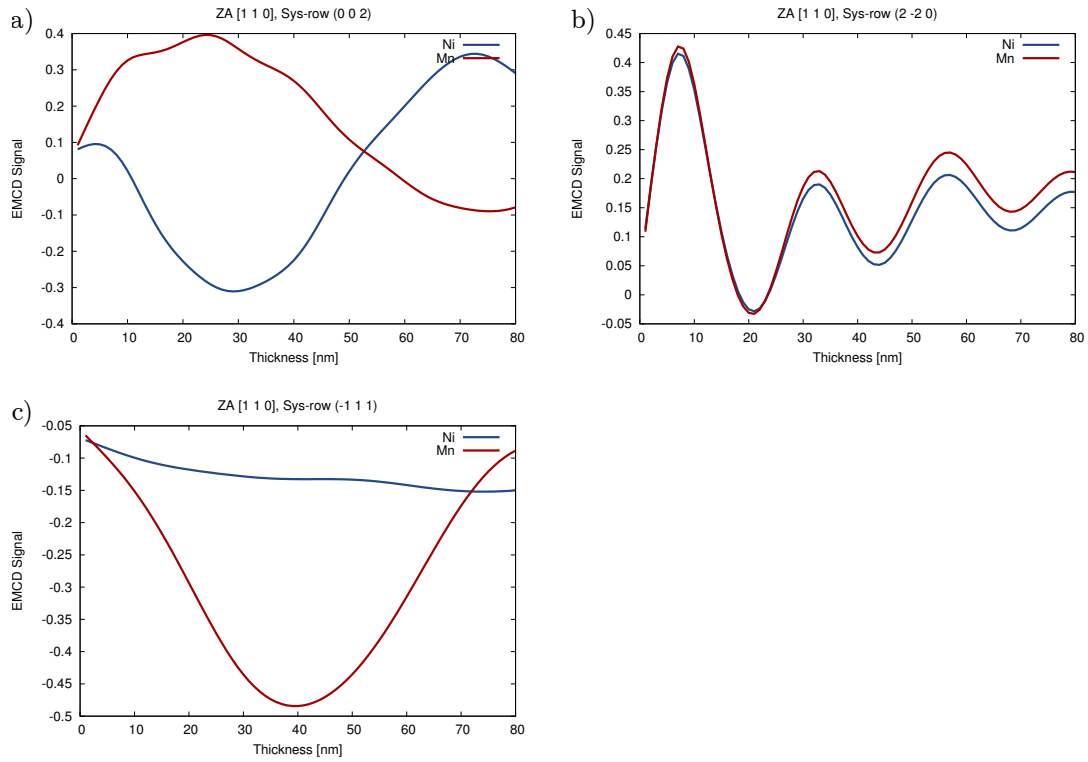


Figure 5.9.: Simulation of the EMCD signal, as defined in equation (5.4), as a function of the sample thickness. A  $\text{Ni}_2\text{MnSn}$  sample with zone axis  $[1\ 1\ 0]$  and a systematic row condition including the a)  $(0\ 0\ 2)$ , b)  $(2\ \bar{2}\ 0)$ , c)  $(\bar{1}\ 1\ 1)$  reflection was used.

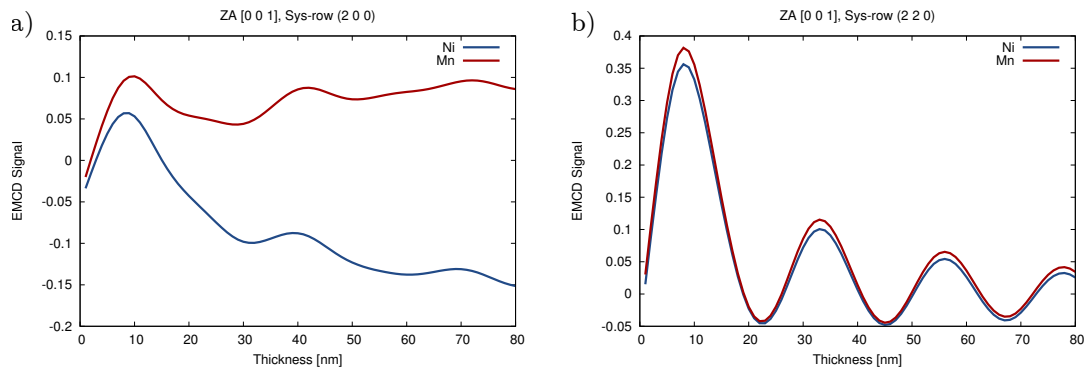


Figure 5.10.: Simulation of the EMCD signal, as defined in equation (5.4), as a function of the sample thickness. A  $\text{Ni}_2\text{MnGa}$  sample with zone axis  $[0\ 0\ 1]$  and a systematic row condition including the a)  $(2\ 0\ 0)$ , b)  $(2\ 2\ 0)$  reflection was used.

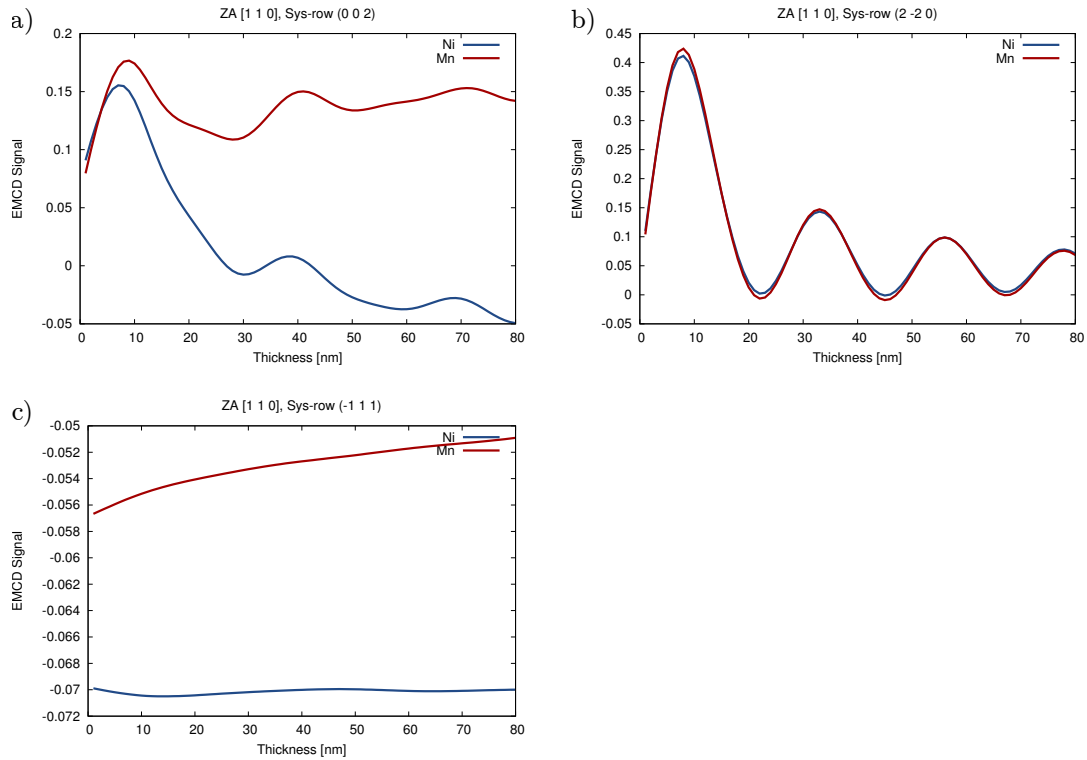


Figure 5.11.: Simulation of the EMCD signal, as defined in equation (5.4), as a function of the sample thickness. A  $\text{Ni}_2\text{MnGa}$  sample with zone axis  $[110]$  and a systematic row condition including the a)  $(002)$ , b)  $(2\bar{2}0)$ , c)  $(\bar{1}11)$  reflection was used.

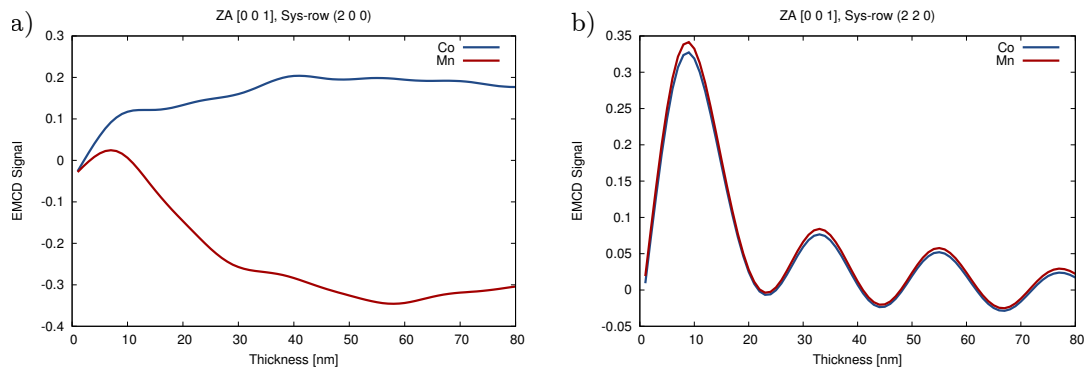


Figure 5.12.: Simulation of the EMCD signal, as defined in equation (5.4), as a function of the sample thickness. A  $\text{Co}_2\text{MnSi}$  sample with zone axis  $[001]$  and a systematic row condition including the a)  $(200)$ , b)  $(220)$  reflection was used.

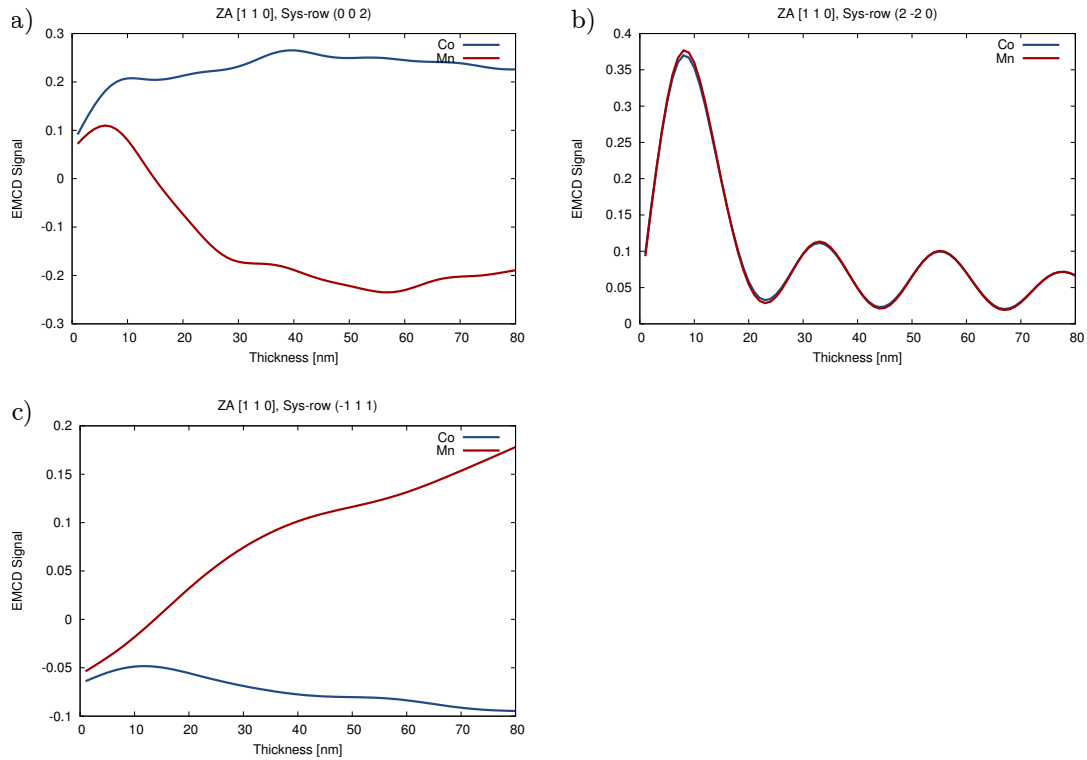


Figure 5.13.: Simulation of the EMCD signal, as defined in equation (5.4), as a function of the sample thickness. A  $\text{Co}_2\text{MnSi}$  sample with zone axis  $[1\ 1\ 0]$  and a systematic row condition including the a)  $(0\ 0\ 2)$ , b)  $(2\ \bar{2}\ 0)$ , c)  $(\bar{1}\ 1\ 1)$  reflection was used.

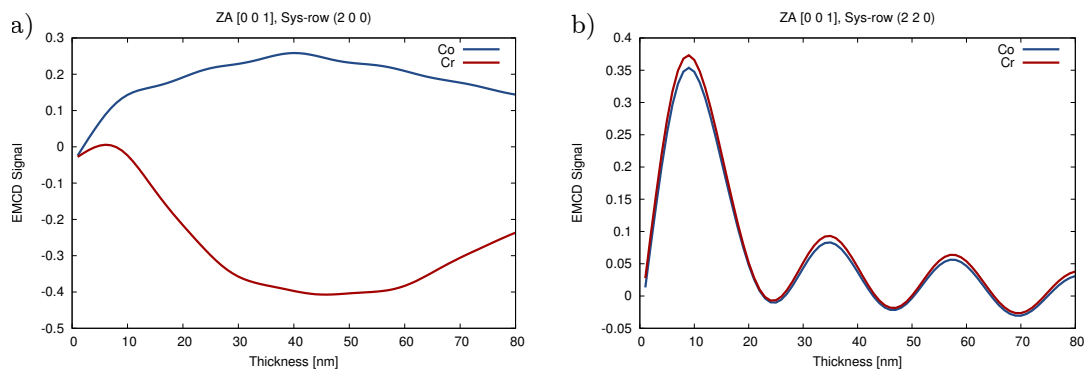


Figure 5.14.: Simulation of the EMCD signal, as defined in equation (5.4), as a function of the sample thickness. A  $\text{Co}_2\text{CrAl}$  sample with zone axis  $[0\ 0\ 1]$  and a systematic row condition including the a)  $(2\ 0\ 0)$ , b)  $(2\ 2\ 0)$  reflection was used.

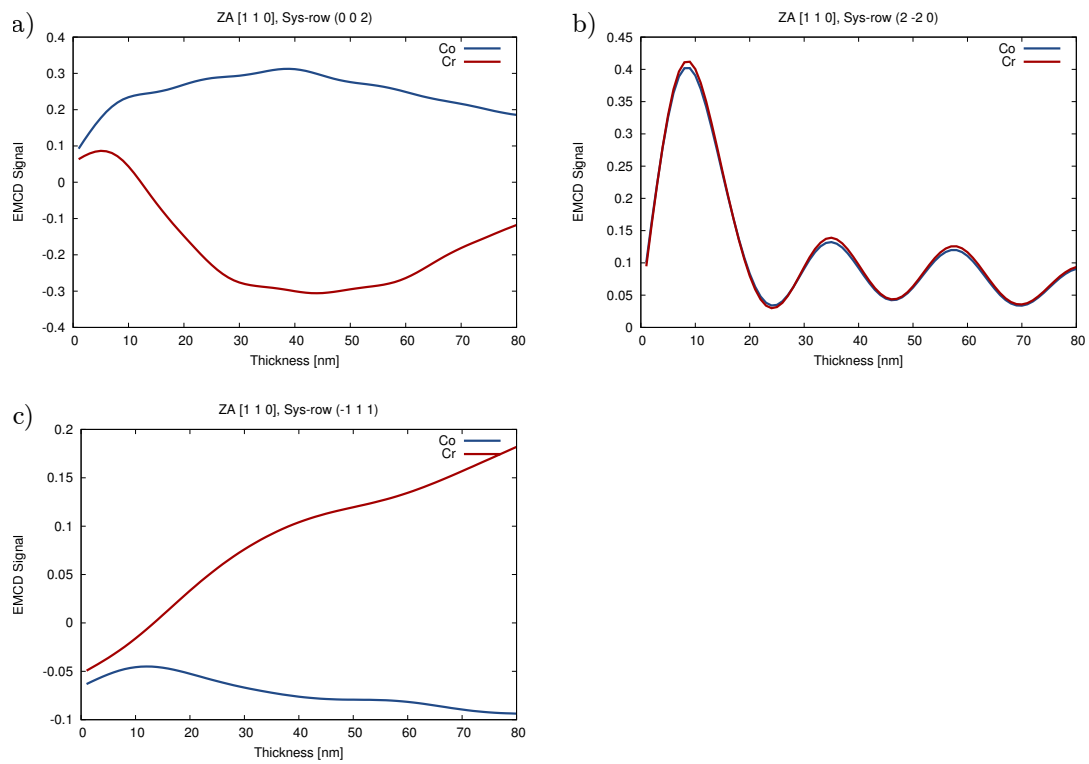


Figure 5.15.: Simulation of the EMCD signal, as defined in equation (5.4), as a function of the sample thickness. A  $\text{Co}_2\text{CrAl}$  sample with zone axis  $[110]$  and a systematic row condition including the a)  $(002)$ , b)  $(2\bar{2}0)$ , c)  $(\bar{1}11)$  reflection was used.



ent dynamical diffraction effects when changing the scattering conditions. Simulations for different materials but the same settings for zone axis and systematic row, exhibit similar results, i.e. similar shapes of the EMCD signal when plotted with respect to the sample thickness.

When for example comparing figures 5.6 and 5.8, one can see that the shape of the plots are the same, only the thickness dependence is shifted for about 10 nm. This can be seen easily when comparing the position of the intersection of the Ni and Mn EMCD signal in the plot a) of both figures. The reason for this similarity can be found in the proximity of In and Sn in the periodic table, thus leading to similar dynamical diffraction effects. When comparing figures 5.6 and 5.7, one can also see that for the same systematic row conditions but different zone axes, the results are also quite similar. The same results as those described above can be seen in the plots of the other calculated materials. The differences in the plots, i.e. in the thickness dependence of the EMCD signal is more pronounced the larger the distance of the elemental constituents of the Heusler alloys in the periodic table is.

In figure 5.16 the simulations of zone axis  $[001]$  and systematic row reflection  $(200)$  are compared for different Heusler alloys. It can be seen that the results are similar for  $\text{Ni}_2\text{MnIn}$  and  $\text{Ni}_2\text{MnSn}$ . The dynamical diffraction effects depend on the scattering conditions and the extinction distance, which in turn shows an elemental dependence. Thus, the results of the simulations are quite similar for the previously mentioned materials, as In and Sn are next to each other in the periodic table. On the contrary, the simulations for the other materials yield quite different results.

For  $\text{Ni}_2\text{MnIn}$ , simulations using 7 incoming and 6 outgoing Bloch waves were performed and compared to the simulations using 3/4 Bloch waves. The comparison for two different scattering conditions is shown in figure 5.17. As can be seen, only minor differences are visible up to a thickness of about 60 nm. Therefore, the simulations using the lower number of Bloch waves are sufficient as predictions to compare with the experimental spectra for samples with a moderate thickness.

### 5.4.2. Effects of beam convergence

As was mentioned in section 5.3, changing the beam convergence alters the experimental conditions for EMCD measurements. While the actual experiments reported in this work were all conducted with a somewhat converged electron beam, the Bloch

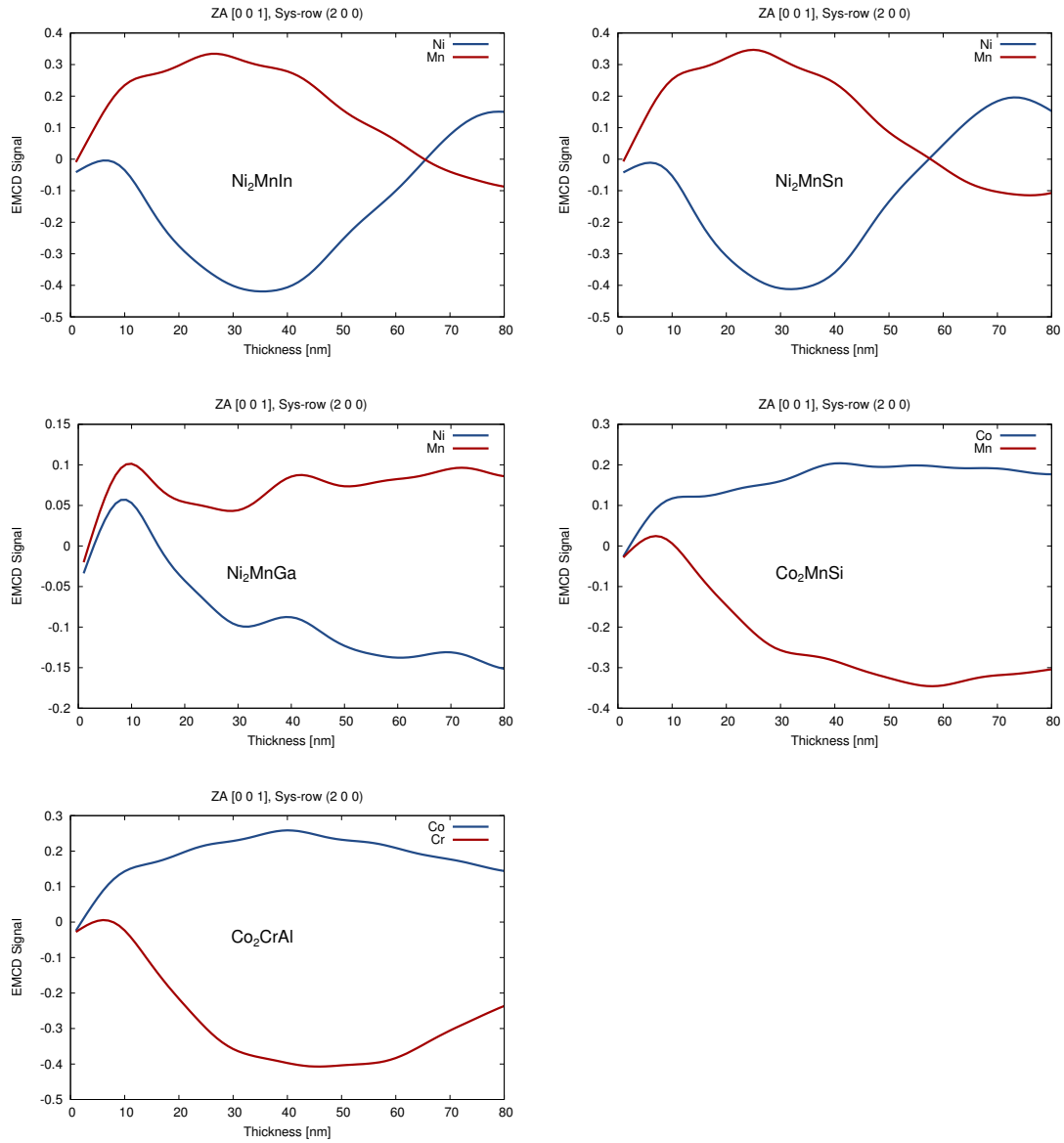


Figure 5.16.: Comparison of the thickness dependent EMCD simulation for different materials. All calculations are made using the same experimental conditions. The scattering geometry uses zone axis [1 0 0] and a systematic row condition including the (200) reflection. In each graph the calculated material is denoted. Thus, the similarities and differences can be figured out easily.

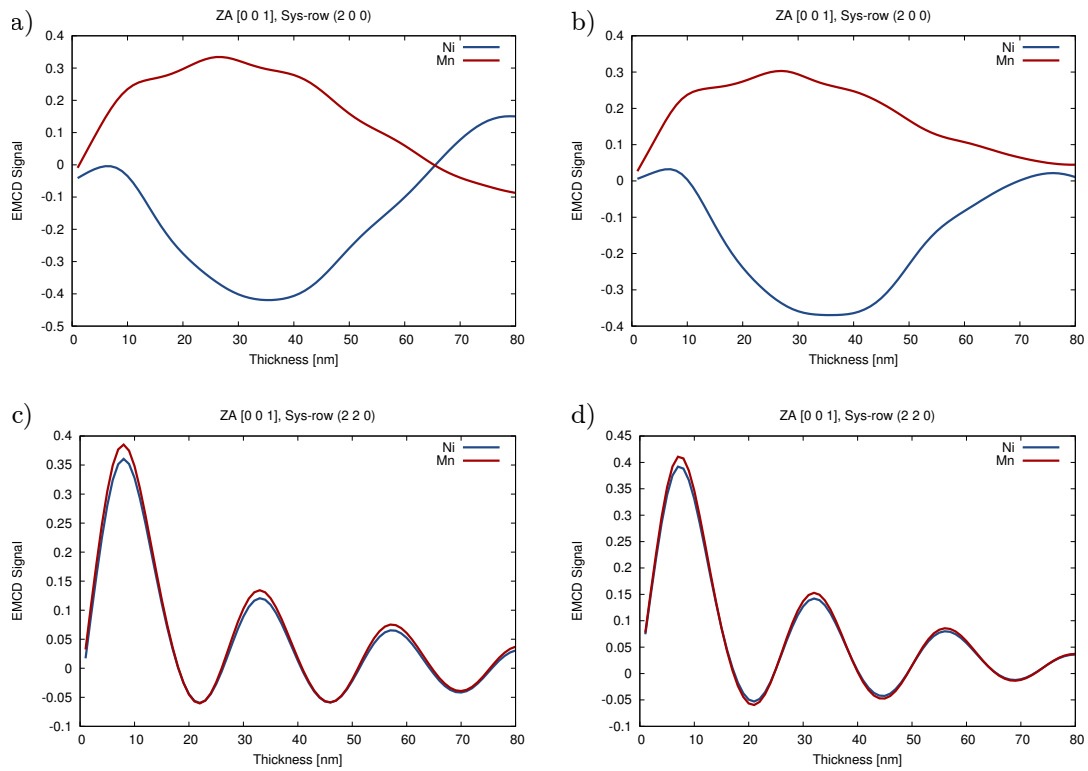


Figure 5.17.: Comparison of the thickness dependent EMCD simulation for a different number of incoming and outgoing Bloch waves. All calculations are made using the zone axis  $[100]$ . Comparing the simulations for a systematic row condition including the  $(200)$  reflection, the calculation shown in a) used 3 incoming and 4 outgoing Bloch waves, while in b) 7 incoming and 6 outgoing Bloch waves were used. The same holds for the simulations shown in c) and d), respectively. It is evident that the results are quite similar, only for thicker sample (60 nm and more), clear differences can be seen.

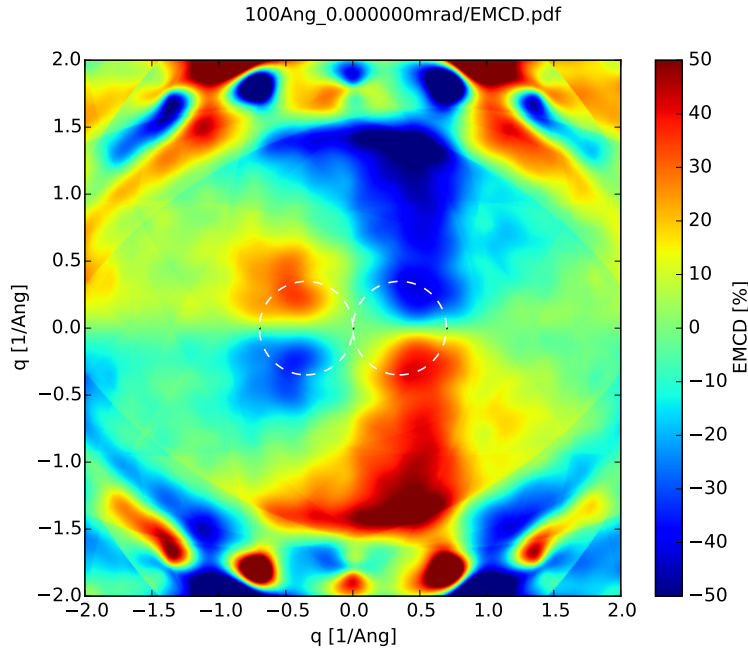


Figure 5.18.: Multislice simulation of the EMCD signal calculated using formula 5.4 if two positions mirrored across the systematic row are compared. The experimental settings for the simulations are given in the text. The beam convergence angle was 0.0 mrad, the centre of the electron beam was located at the position of an atomic column. The transmitted beam and the (200) reflection are marked with black dotted circles, while the Thales-circles for the “standard” EMCD measurement positions are marked with white dashed circles. As can be seen easily, the EMCD position at the thales circle give a good EMCD signal.

wave simulations take a incoming plane wave as granted. Therefore, the effect of beam convergence on the EMCD signal is investigate in order to determine, whether the plane wave approximation is sufficient for comparison with the experiments.

The multislice program *ixchel* was used to do the calculations [16]. A simple bcc-Fe sample was given as input, with a thickness of 100 Å and a step size of 1 Å. The energy loss was set to that of the Fe  $L_3$ -edge at 707 eV. The convergence angle of the electron beam was changed from 0.0 mrad (a plane wave) to 20.0 mrad (used in aberration corrected STEMs with down to 70 pm resolution) in steps of 2.0 mrad. The centre of the electron beam was set to be at the position of an atomic column. The results of some of the simulations are shown exemplarily in figures 5.18 to 5.23. A second series

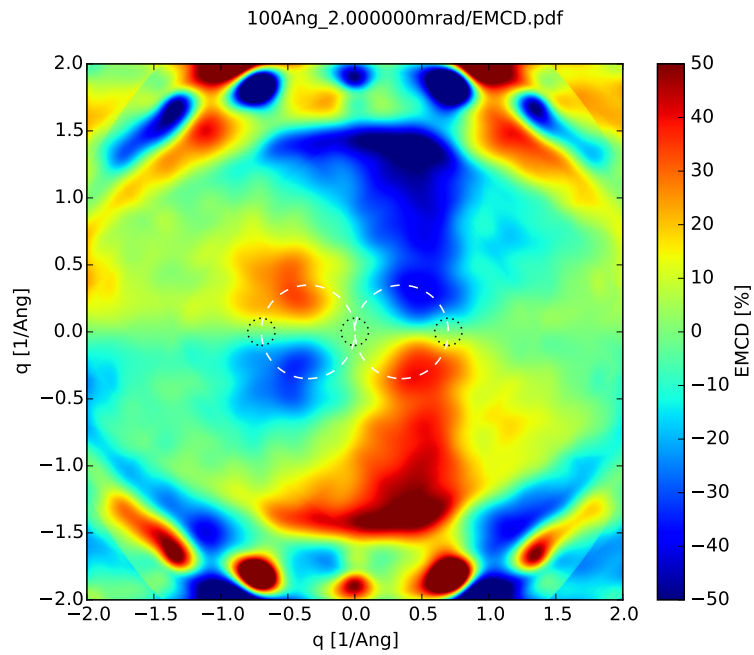


Figure 5.19.: Same as figure 5.18 but the beam convergence angle was changed to 2.0 mrad.

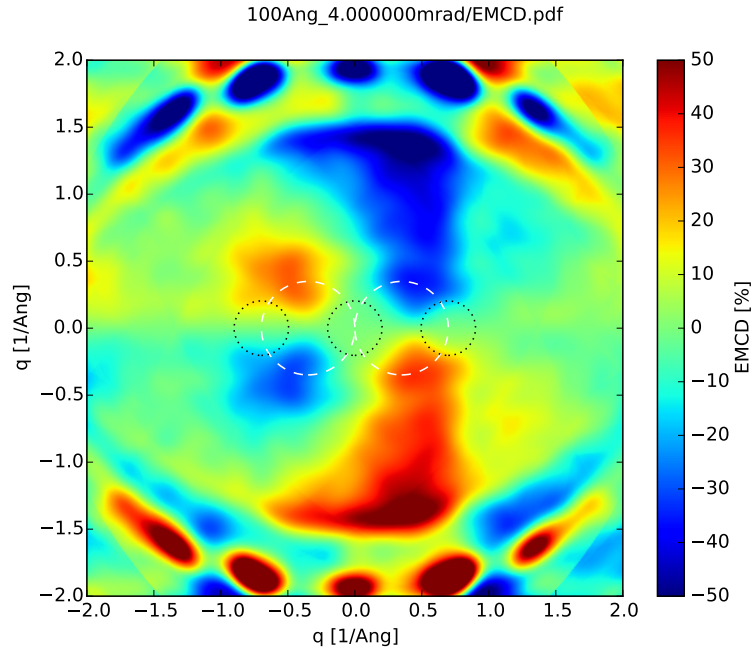


Figure 5.20.: Same as figure 5.18 but the beam convergence angle was changed to 4.0 mrad.

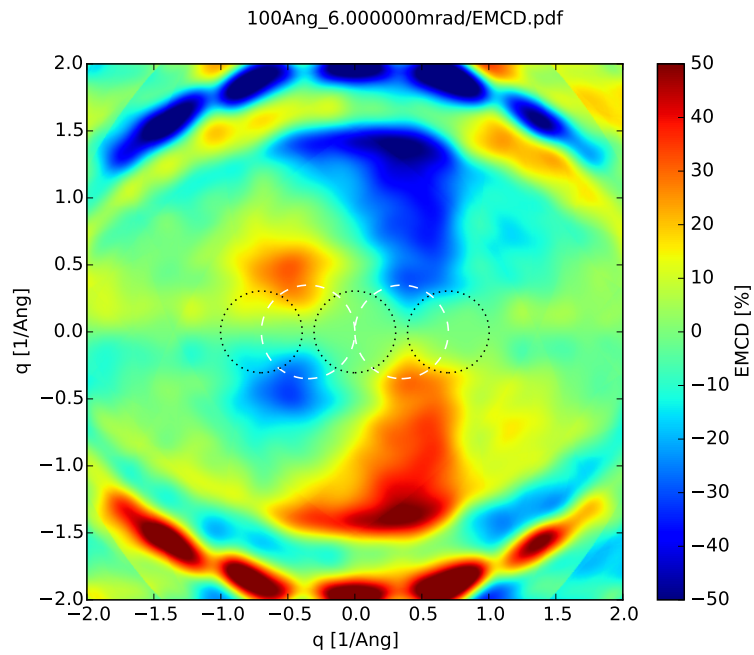


Figure 5.21.: Same as figure 5.18 but the beam convergence angle was changed to 6.0 mrad.

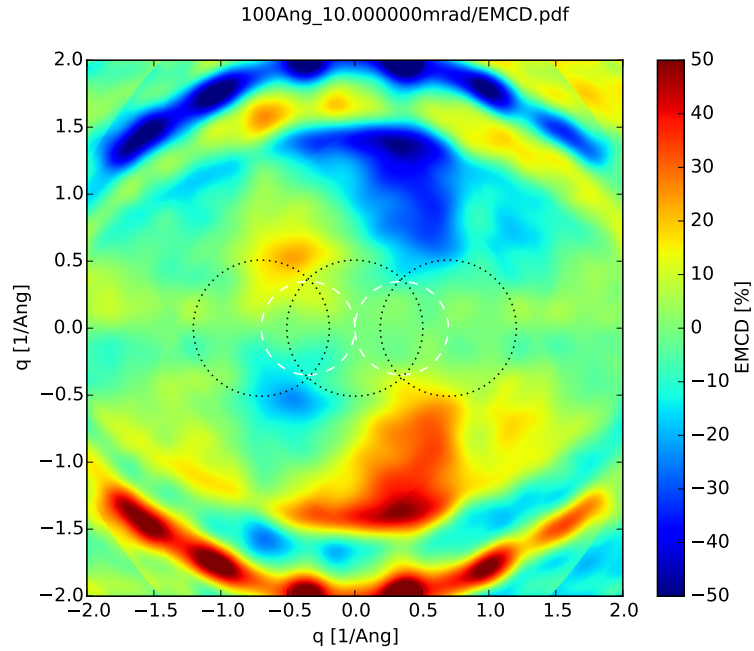


Figure 5.22.: Same as figure 5.18 but the beam convergence angle was changed to 10.0 mrad.

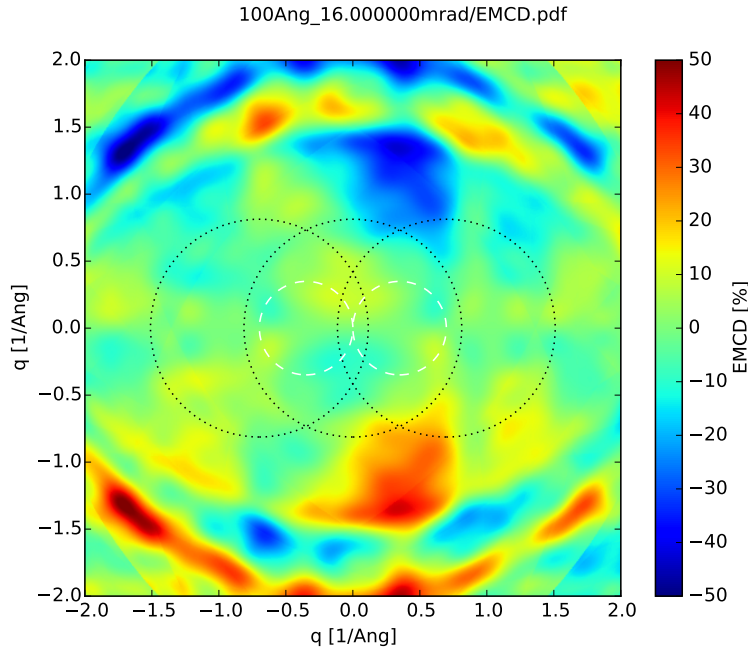


Figure 5.23.: Same as figure 5.18 but the beam convergence angle was changed to 16.0 mrad.

of simulations was performed. The settings were the same except for the centre of the electron beam which was positioned between the atomic columns. Figures 5.24 and 5.25 show the results for convergence angle 0.0 mrad and 16.0 mrad. Comparing figures 5.18 and 5.24, no differences are visible. As these simulations resemble parallel illumination of the sample in the TEM, this is exactly what was expected. However, comparing figures 5.23 and 5.25, one can clearly spot differences in the calculated EMCD signal. This is also expected, as the convergence angle of 16.0 mrad would allow for a spatial resolution in the order of the distance between the atomic columns. When the beam is located at the atomic columns, the “standard” measurement positions at the Thales-circle would not yield a sufficient EMCD signal (see figure 5.23). When the centre of the electron beam is positioned between two atomic columns, the above mentioned “standard” detector positions would result in an EMCD signal with higher intensity compared to the setting shown in figure 5.23. In both cases, the ideal measurement positions are not at the Thales-circle anymore, but just above and below the intersection of the  $\mathbf{0}$  and  $\mathbf{G}$  reflection.

As can be seen from the figures, the plane wave approximation is sufficient for the

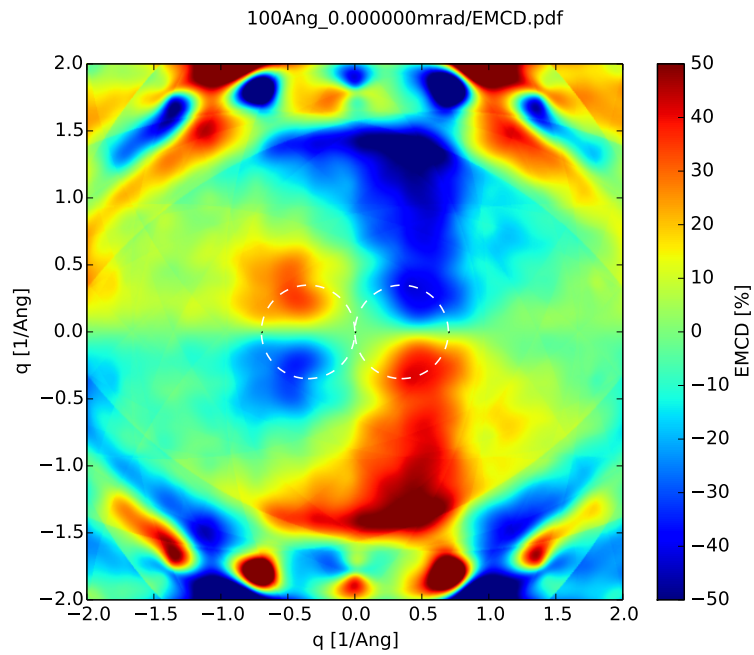


Figure 5.24.: Same as figure 5.18 but the position of the centre of the electron beam was between the atomic columns.

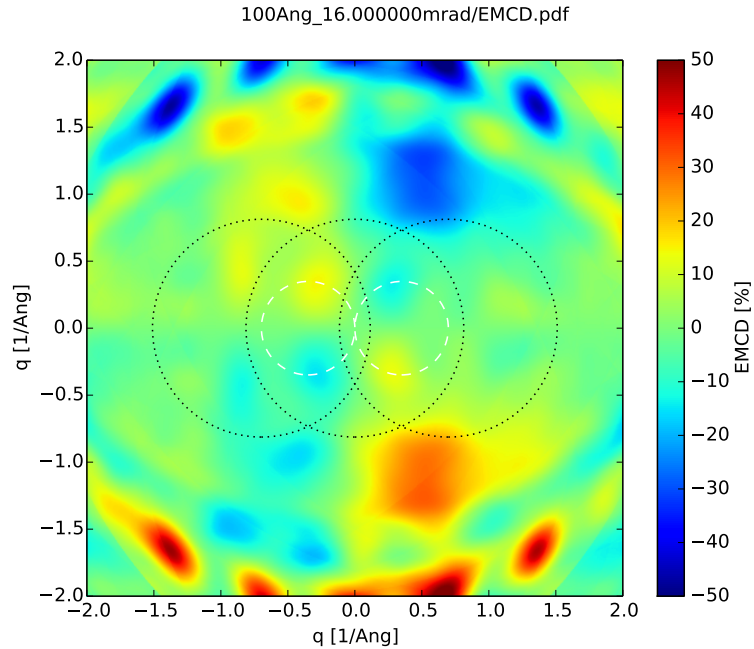


Figure 5.25.: Same as figure 5.24 but the beam convergence angle was changed to 16.0 mrad.



measurements discussed in this work. The convergence angle used in the experiments is in all cases smaller than 2.0 mrad. The simulation for such a convergence angle shows that the measurement positions at the Thales-circle still give a good EMCD signal.

If one would like to conduct EMCD with atomic resolution, one has to take a look at the simulations for 16 mrad. Positioning the EELS detector at the Thales-circle would not yield a sufficient EMCD signal, if any. On the contrary, one would need to take measurements further off the systematic row. As mentioned above, the simulations show that the ideal detector position would be at the intersection of the  $\mathbf{0}$  and  $\mathbf{G}$  reflection. As mentioned in section 5.3.2 atomic resolution EMCD could also be achieved using the generation of vortex beams or investigating variations in the energy filtered diffraction pattern.

## 5.5. Calculating magnetic moments

In order to understand the magnetic behaviour of materials, the magnetic moment of individual atoms is an important quantity to investigate. Sum rules to calculate the spin magnetic moment  $m_s$  and orbital magnetic moment  $m_l$  of an atom can be applied to XMCD spectra [58]. These XMCD sum rules can be written as [60]:

$$\frac{\int_{L_3} \sigma_M(\hbar\omega) d\omega - 2 \int_{L_2} \sigma_M(\hbar\omega) d\omega}{\int_{L_3+L_2} (\sigma_o(\hbar\omega) + \sigma_+(\hbar\omega) + \sigma_-(\hbar\omega)) d\omega} = \frac{2}{3n_h} \langle S_z \rangle + \frac{7}{3n_h} \langle T_z \rangle \quad (5.10)$$

$$\frac{\int_{L_3} \sigma_M(\hbar\omega) d\omega + \int_{L_2} \sigma_M(\hbar\omega) d\omega}{\int_{L_3+L_2} (\sigma_o(\hbar\omega) + \sigma_+(\hbar\omega) + \sigma_-(\hbar\omega)) d\omega} = \frac{\langle L_z \rangle}{2n_h}, \quad (5.11)$$

with  $\langle L_z \rangle$  and  $\langle S_z \rangle$  the ground state expectation values of the orbital momentum and spin momentum operators.  $\langle T_z \rangle$  is the magnetic dipole term. The absorption spectrum with the photon spin parallel to the sample magnetisation is denoted by  $\sigma_+$ ,  $\sigma_-$  is the absorption spectrum with antiparallel orientation of the photon spin. If the photon spin is orthogonal to the magnetisation, the absorption spectrum is described by  $\sigma_0$ . The magnetic dichroic signal is defined as  $\sigma_M = \sigma_+ - \sigma_-$ . As the above formula is valid for excitations into  $d$ -states,  $n_h$  describes the number of valence  $d$  holes.

Soon after the development of the EMCD technique, similar sum rules were derived for use in the TEM [43, 44]. As a recurrent issue for all techniques making use of interferometric EELS, the effect of the crystalline sample itself on the measured spectra

is not negligible. The EMCD sum rules can be written as:

$$\frac{\int_{L_3}(\sigma^+ - \sigma^-)dE - 2 \int_{L_2}(\sigma^+ - \sigma^-)dE}{\int_{L_3+L_2}(\sigma^+ + \sigma^-)dE} = K \left( \frac{2 \langle S_z \rangle}{3 N_h} + \frac{7 \langle T_z \rangle}{3 N_h} \right) \quad (5.12)$$

$$\frac{\int_{L_3+L_2}(\sigma^+ - \sigma^-)dE}{\int_{L_3+L_2}(\sigma^+ + \sigma^-)dE} = K \frac{1 \langle L_z \rangle}{2 N_h}, \quad (5.13)$$

with  $\frac{\langle S_z \rangle}{N_h}$ ,  $\frac{\langle L_z \rangle}{N_h}$  and  $\frac{\langle T_z \rangle}{N_h}$  being the ground-state expectation value of the spin moment, orbital moment and magnetic-dipole operators per electron hole in the  $d$ -bands, respectively. The XMCD and EMCD sum rules look quite similar if they are compared. Nevertheless, there is a quite important difference, which makes calculations much more demanding when using the EMCD sum rules. Only for EMCD there is a coefficient  $K$  which contains all information caused by dynamical diffraction effects in the crystalline sample. As it is an almost hopeless endeavour to accurately describe  $K$  for an actual experiment [44], one can obtain a formulation independent of  $K$  by taking the ratio of the two previous equations:

$$\frac{\int_{L_3}(\sigma^+ - \sigma^-)dE - 2 \int_{L_2}(\sigma^+ - \sigma^-)dE}{\int_{L_3+L_2}(\sigma^+ - \sigma^-)dE} = \frac{4 \langle S_z \rangle + 14 \langle T_z \rangle}{3 \langle L_z \rangle}. \quad (5.14)$$

As the contribution of the magnetic-dipole operator is usually very small [43], equation (5.14) allows a direct evaluation of the ratio  $\frac{\langle L_z \rangle}{\langle S_z \rangle}$  from the acquired EMCD spectra. The spin and orbital magnetic moments can be evaluated as [58]:

$$\frac{m_l}{m_s} = \frac{2}{3} \frac{\int_{L_3+L_2}(\sigma^+ - \sigma^-)dE}{\int_{L_3}(\sigma^+ - \sigma^-)dE - 2 \int_{L_2}(\sigma^+ - \sigma^-)dE}. \quad (5.15)$$

A common problem seen in many EMCD measurements concerns the magnitude and sign of the EMCD effect at the  $L_2$  edge. In XMCD, the effect at the  $L_3$  and  $L_2$  edge show different sign, with the effect at the  $L_2$  edge being smaller in magnitude, which would also be the expectation for EMCD. Apart from dynamical diffraction effects, which influence both L-edges in a similar manner, it can be seen that in many measurements the effect at the  $L_2$  edge is much smaller than expected or even has the same sign as the effect at the  $L_3$  edge. Up to now, this behaviour is not fully understood [57]. Closely related to this effect is the problem of an overestimation of the ratio  $\frac{m_l}{m_s}$  compared to results obtained with XMCD [44, 57, 61, 62]. In [62] these observations are explained to be

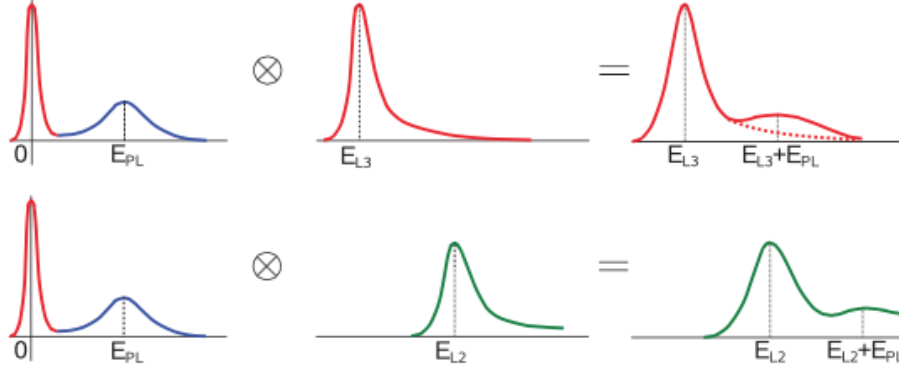


Figure 5.26.: Sketch of the effect of convolution of the low-loss signal with the core-loss signal, leading to an additional peak. If the  $L_2$  edge is near the  $L_3$  edge, it is enhanced with a fraction of plural scattering signal from the  $L_3$  excitation. Taken from [62].

related to multiple scattering effects. The convolution of the core-loss signal ( $L_3$  and  $L_2$  edge) with the low-loss region leads to additional signal intensity (and eventually a double peak structure) a few eV after the  $L_{2,3}$  edge due to the plasmon peak, see figure 5.26. If the  $L_2$  edge is near the  $L_3$  edge, it is enhanced with a fraction of plural scattering signal from the  $L_3$  excitation. The fractions of the measured core-loss signal and their origin can be described as follows:

$$\sigma^+ = \underbrace{N_{L_3} + M_{L_3}}_{L_3} + \underbrace{[N_{L_2} + M_{L_2}]}_{L_2 \text{ net}} + \underbrace{k(N_{L_3} + M_{L_3})}_{\text{plural scattering}} \quad (5.16)$$

$$\sigma^- = \underbrace{N_{L_3} - M_{L_3}}_{L_3} + \underbrace{[N_{L_2} - M_{L_2} + k(N_{L_3} - M_{L_3})]}_{L_2 \text{ total}}, \quad (5.17)$$

with  $N$  and  $M$  denoting the non-magnetic and magnetic fraction of the measured signal and  $k = A_{P1}/A_{ZLP}$  is the ratio of the energy integral of zero-loss peak  $A_{ZLP}$  and plasmon peak  $A_{P1}$  [62]. The EMCD signal (difference spectrum) can be written as

$$\Delta\sigma = \underbrace{2M_{L_3}}_{L_3} + \underbrace{[2M_{L_2} + 2kM_{L_3}]}_{L_2}. \quad (5.18)$$

When evaluating the influence of plural scattering in the EMCD sum rules, one arrives

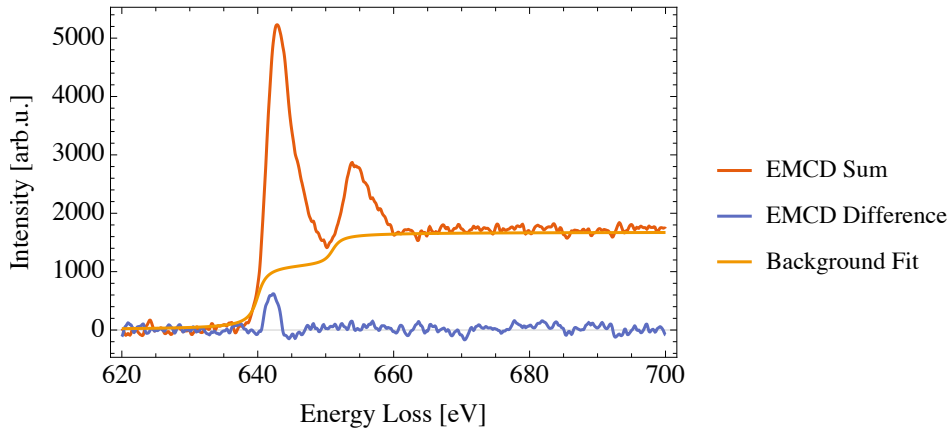


Figure 5.27.: Sum and difference of the Mn  $L_{2,3}$ -edge energy-loss spectra of  $\text{Ni}_2\text{MnIn}$  acquired at the two EMCD positions are shown. Furthermore, the background fit used for the calculation of the magnetic moments is depicted.

at an expression [62]:

$$\left. \frac{m_l}{m_s} \right|_{obs} \approx \left. \frac{m_l}{m_s} \right|_{net} \left( 1 + \frac{4k}{3} \right) + \frac{2k}{9}, \quad (5.19)$$

describing the change of the observed ratio of magnetic moments due to plural scattering effects.

The spin and orbital magnetic moments are calculated for the Mn  $L_{2,3}$ -edge of an  $\text{Ni}_2\text{MnIn}$  Heusler alloy, taken exemplarily for the measured EMCD spectra in this work. In figure 5.27 the sum and difference of the energy-loss spectra acquired at the two EMCD positions are shown, as well as the background fit used to determine the integration limit as described in [63]. For the fit-function the following formula was used [57]:

$$f = h \left[ \frac{2}{3} \left( \frac{1}{2} + \frac{1}{\pi} \arctan \frac{E - L_3}{\delta_E} \right) + \frac{1}{3} \left( \frac{1}{2} + \frac{1}{\pi} \arctan \frac{E - L_2}{\delta_E} \right) \right], \quad (5.20)$$

with  $L_3$  and  $L_2$  the energies of the respective core-loss edges,  $\delta_E$  the energy resolution and  $h$  a fit parameter determined by the intensity of the post-edge background.

Using equation (5.15), the measured spectra yield a ratio of  $m_l/m_s = 1.21 \pm 2.66$ , with an error higher than expected. The value of  $m_l/m_s$  should lie between 0.05 and 0.14, as it was determined by means of XMCD [64]. The errors given for the result of the calculation of  $m_l/m_s$  arise mainly from the spectral noise in the spectra used for evaluation, as described in [65]. Assuming poisson noise and subsequent propagation of

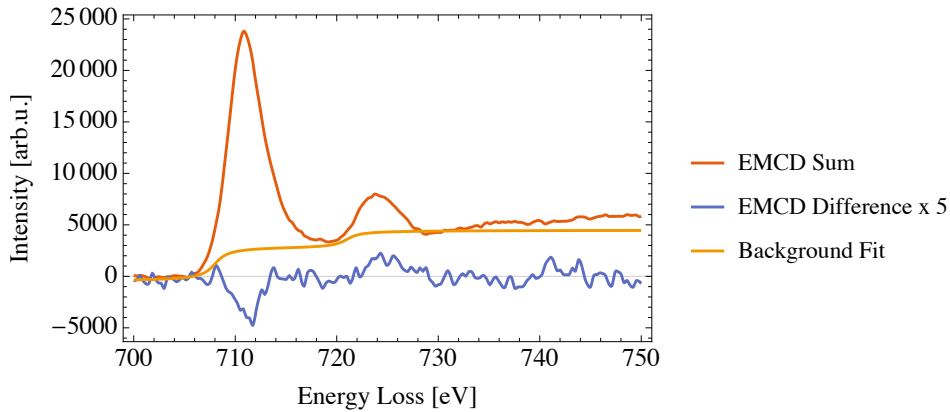


Figure 5.28.: Sum and difference of the Fe  $L_{2,3}$ -edge energy-loss spectra of magnetite acquired at the two EMCD positions are shown. Furthermore, the background fit used for the calculation of the magnetic moments is depicted.

errors in formula (5.15) yield the errors given above. Considering the effect of multiple scattering, equation (5.19) can be used to calculate a corrected value of the ratio of magnetic moments. As the sample thickness was  $\sim 50$  nm, a value of  $k = 0.3$  was assumed, in analogy to [62]. This leads to  $m_l/m_s = 0.66$ , which is still too high.

It can be seen from figure 5.27 that there is no EMCD effect visible at the  $L_2$  edge. The reason for this behaviour is still unclear [57]. Including multiple scattering effects in the calculation improves the determined values for  $m_l/m_s$ , but for measurements exhibiting no EMCD effect at the  $L_2$  edge, the calculated values are still considered to be unreliable.

The sum and difference of the Fe  $L_{2,3}$ -edge energy-loss spectra of magnetite, acquired at the same EMCD positions as above is shown in figure 5.28. The depicted measurements exhibit an EMCD effect at the  $L_3$  edge as well as at the  $L_2$  edge. The ratio of the orbital and spin magnetic moments can be determined as  $m_l/m_s = 0.12 \pm 0.02$  using equation (5.15). This value fits quite good to values acquired by means of DFT simulations [66] ( $m_l/m_s = 0.11$ ) and it is similar to the ratio of the magnetic moments determined by XMCD [66] ( $m_l/m_s = 0.18$ ). Thus, one can see that for magnetite, the methods for calculating the ratio of the orbital and spin magnetic moments from EMCD measurements give satisfying results. It is evident that in contrast to the  $Ni_2MnIn$  measurements shown in figure 5.27, the magnetite experiments exhibit an EMCD effect on both edges,  $L_3$  and  $L_2$  (figure 5.28).

Part III.  
Applications

# 6. EMCD investigation of Heusler alloys

## 6.1. Introduction

The following chapter describes investigations performed as part of a German project called “Ferroic cooling” in which a number of universities and research institutions collaborate. The aim of the project is to investigate and design possible materials for ferroic cooling applications. The most promising materials turned out to be Heusler alloys. Sections 6.2, 6.3 and 6.4 give an overview of Heusler compounds as well as their magnetocaloric properties.

In collaboration with the Bielefeld University, TEM investigations were conducted at the Vienna University of Technology. The goal of these microscopical studies was to characterise the materials produced by the collaborating institutions and to decide whether or not they are suitable for the required tasks in the project. Therefore, beyond standard TEM investigations, EMCD measurements were performed, as it is a versatile method to investigate the magnetic properties of samples on a nanoscale. The technique was applied to a number of Heusler alloys to investigate the change of magnetic moments across a magnetostructural phase transition. The results of these experiments are described in section 6.5. Furthermore, the reliability of the EMCD technique applied to this specific task will be discussed.

## 6.2. Heusler compounds

Heusler alloys are a versatile class of materials as they exhibit a variety of magnetic properties, such as magneto-optical, magneto-structural and magneto-caloric effects [67]. A number of Heusler compounds can be characterised as half-metals, which show a

semiconducting nature for electrons of one spin direction while they are conducting for electrons of the other spin direction. Nota bene: one should not confound half-metals with semi-metals nor with metalloids which in German are referred to as “Halbmetalle”. In general, one can distinguish between Half-Heusler materials with a stoichiometry of 1 : 1 : 1 and (full) Heusler alloys with a 2 : 1 : 1 stoichiometry. The following descriptions will deal with the properties of the full Heusler materials, as only such alloys were in the focus of investigation.

Heusler materials can be described by the formula  $X_2YZ$  with X and Y usually being transition metals and Z as a main group element. These compounds crystallise in the cubic space group  $Fm\bar{3}m$  (space group no. 225), the X-element occupies the Wyckoff position 8c (1/4, 1/4, 1/4), the Y-element position 4a (0, 0, 0) and Z the 4b (1/2, 1/2, 1/2) position. This structure is also referred to as  $L2_1$  structure according to the “Strukturberichte”-nomenclature and the prototype material is  $Cu_2MnAl$  [67]. The described phase is the Heusler’s austenitic or high-temperature state. A schematic of the unit cell is shown in figure 6.1. Upon decreasing the temperature, the compounds can undergo a phase transition into the martensitic state with a number of possible structures [68]. For NiMn based Heusler compounds, especially those with a non-stoichiometric concentration of the Z-element, the transformation results in a tetragonal  $L1_0$  structure, as this is the structure of  $Ni_{50}Mn_{50}$  in its ground state. Moreover, modulated structures can be found below the martensitic transformation temperature  $T_f$ , mostly for compounds with a higher concentration of the Z-element. The most common modulated structures are referred to as “5M” and “7M” or sometimes also called “10M” and “14M”, respectively. The “M” refers to the monoclinicity present in the distortions connected with the modulation [68]. A sketch of the modulated structures can be seen in figure 6.2, a HRTEM image of the austenitic and the martensitic phase in a NiMnSn Heusler is shown in figure 6.3.

According to [68],  $Ni_2MnSn$  is the only stoichiometric Heusler alloy that shows no volume change during the martensitic transition, while other Heusler compounds do show such a volume change. Figure 6.4 shows the dependence of the martensitic transition temperature on the elemental concentration of the Z-element for three different Heusler compounds. The elemental concentration of Z also governs the valence electron concentration per atom ( $e/a$ ). As will be shown, this value is a very important one to characterise the properties of a Heusler compound. Alloys containing different elements but the same valence electron concentration show very similar properties. The



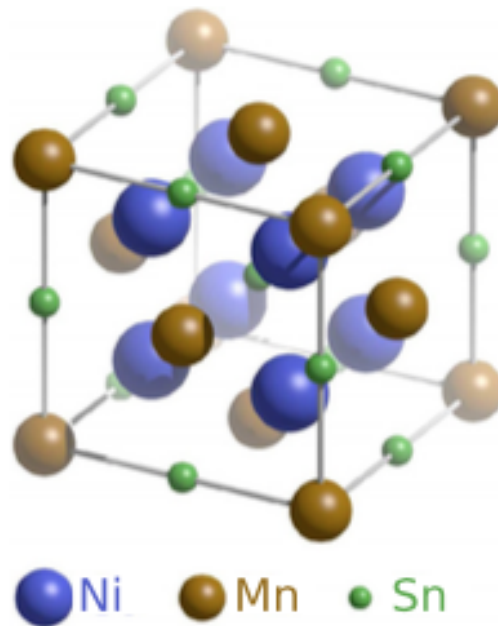


Figure 6.1.: Schematic of the  $Fm\bar{3}m$  structure of Heusler alloys, using  $\text{Ni}_2\text{MnSn}$  as example material. This schematic holds for all stoichiometric Heusler compounds in the austenitic phase with the X element occupying the blue positions, the Y and Z elements the brown and green positions, respectively. This figure was taken from [51].

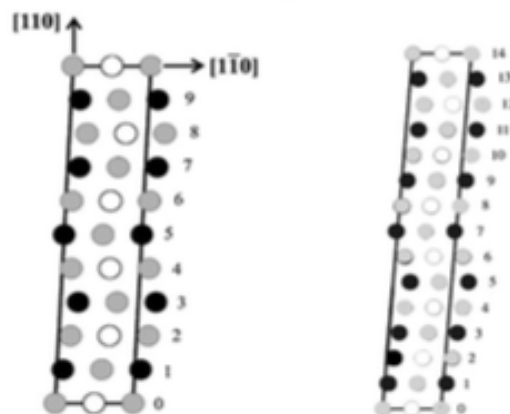


Figure 6.2.: Sketch of the “5M” (left) and “7M” (right) modulated structures in a top view. This figure was adapted from [68].

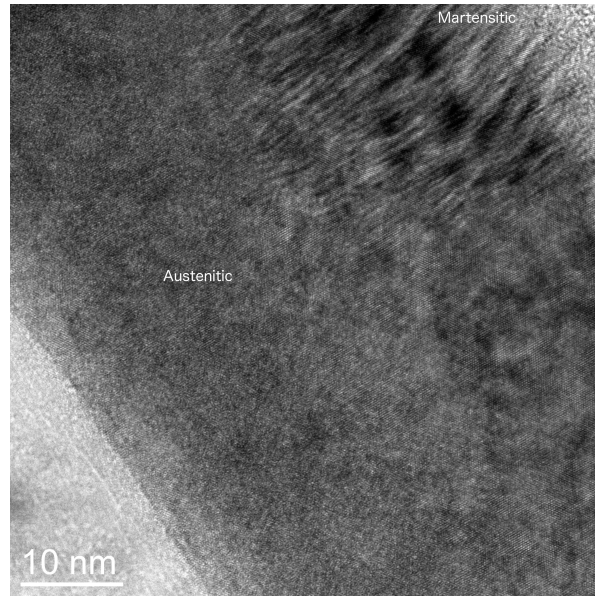


Figure 6.3.: HRTEM image of a  $\text{Ni}_2\text{MnSn}$  Heusler showing martensitic (top) and austenitic regions. The contrast of the modulated structure of the martensitic phase can be seen easily. In the austenitic phase no such modulations are visible.

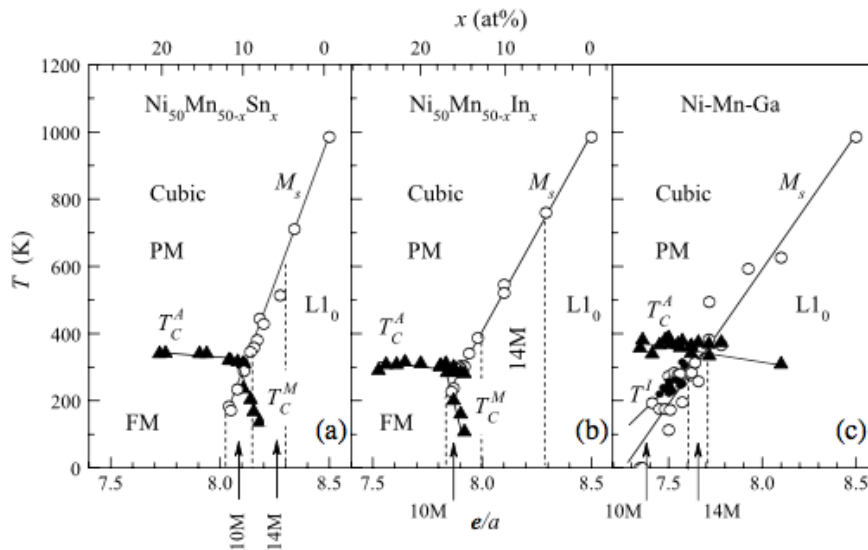


Figure 6.4.: Structural phase diagram of  $\text{NiMnZ}$  Heusler alloys for three different Z-elements: Sn (a), In (b) and Ga (c). On the top edge, the concentration of the Z-element in atomic percent is given, while on the bottom edge the corresponding valence electron concentration per atom ( $e/a$ ) is given. This graph was taken from [68].

figure also shows the regions where the cubic parent structure, the “10M”-modulated, the “14M”-modulated structure and the  $L1_0$  tetragonal phase are formed.

The formation of the energy levels in Heusler compounds is described in [67] using the example of a  $\text{Fe}_2\text{VAl}$  Heusler. The  $s$  and  $p$  orbitals of Fe and Al form hybridised bonding and antibonding  $a_1$  and  $t_2$  levels while the iron’s  $d$  orbitals split into  $e$  and  $t_2$  energy levels. This electronic structure can be seen as that of an  $[\text{FeAl}]$  compound which in turn hybridises with the remaining Fe and V atoms. The  $e$  and  $t_2$  states of the two Fe atoms form then a pair of  $e$  and  $t_{2g}$  states (bonding and antibonding) while the V  $d$  states are inserted inbetween this pair of energy levels close to the Fermi level, also as  $e$  and  $t_{2g}$  states. The density of states near the Fermi level determines the semiconducting and magnetic properties of the Heusler alloy. There happens to be a “24-electron-rule” for Heusler-alloys incorporating more than one transition metal [67]. This rule states that a compound is semiconducting as long as it has 24 valence electrons. Changing the number of the valence electrons turns the Heusler alloy into a paramagnetic or ferromagnetic metal. The electronic structure of a number of Heusler-alloys and their corresponding properties are also described and calculated in [69] using density functional theory. In that work it is shown that in order to calculate the electronic properties using DFT, care has to be taken which kind of exchange-correlation functional is chosen.

Concerning the magnetic properties, similar to the Slater-Pauling rule for binary alloys, an analogue formula can be used to calculate the magnetic moment per formula unit:

$$m_{X_2YZ} = N_V - 24, \quad (6.1)$$

with  $N_V$  the number of valence electrons per formula unit [67]. The Heusler compounds consist of two magnetic sublattices which can show a ferromagnetic or antiferromagnetic interaction.

Even a small atomic disorder in the structure leads to a quite different electronic structure and thus to different magnetic properties. Therefore, analysing the structure of the investigated compounds is crucial to interpret their behaviour. This can be done for example by combining electronic structure calculations and XAS [70]. For the investigated materials in this work, usually x-ray diffraction patterns were recorded by the producing institutions before the beginning of the sample preparation for TEM investigations.

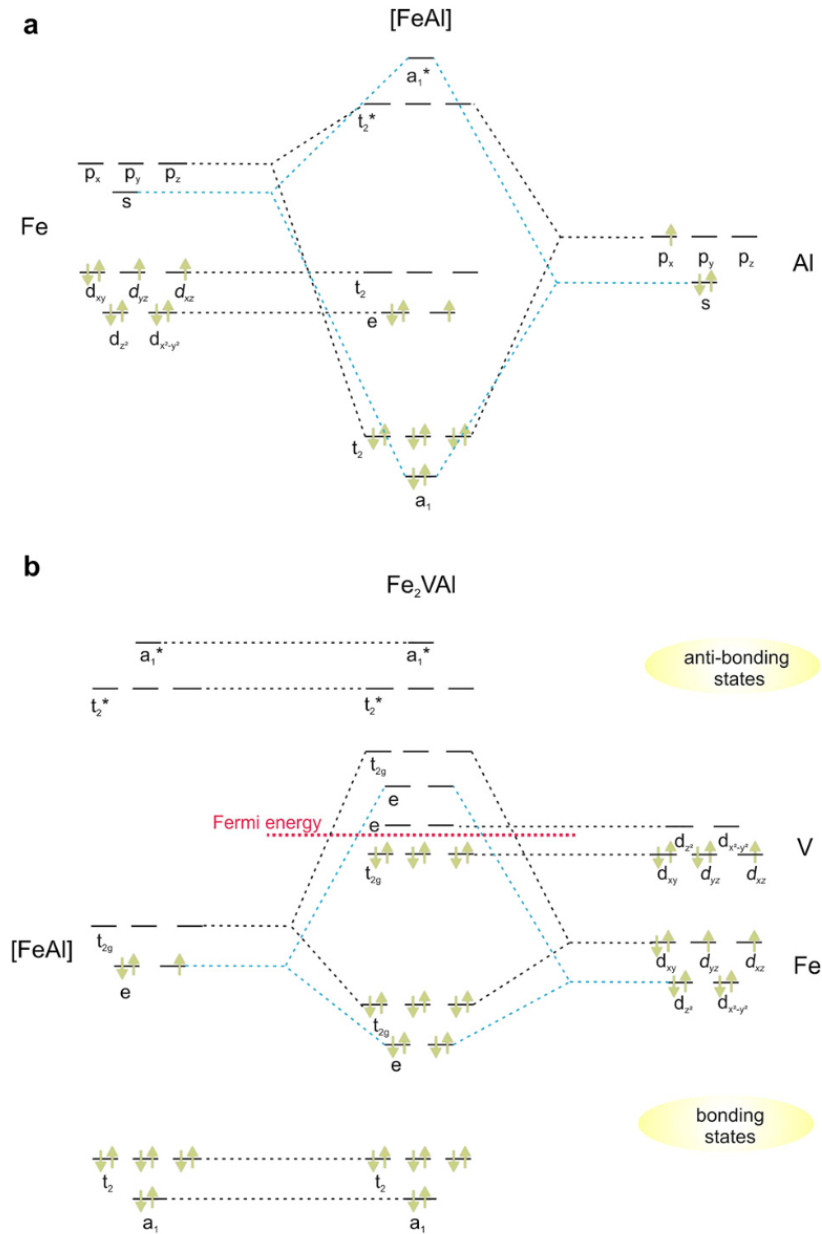


Figure 6.5.: Schematic of the hybridisation of orbitals/energy bands in Heusler materials using the example of  $Fe_2VAI$ . In the upper part (a) the hybridisation of Fe and Al is shown, while in the lower part (b) the hybridised energy bands of the combination of [FeAl] with V and the second Fe atom is depicted. Taken from [67].

### 6.3. Magnetocaloric effect

In a review article [68], the magnetocaloric properties of ferromagnetic Heusler compounds are described in detail using NiMn-based alloys as example materials. Magnetocaloric effects can be found in any magnetic material due to the connection of thermal and magnetic material properties. The effects can be measured as a temperature change (if the process is adiabatic) or an entropy change (if the process is isothermal) when changing an external magnetic field. Heusler-alloys are an interesting class for making use of the magnetocaloric properties, as the observable effects can be tuned by changing the elemental composition of the compounds.

The magnetocaloric effect shows up in the vicinity of the martensitic transition of Heusler compounds. The conventional magnetocaloric effect shows a negative entropy change for this transition, while the inverse effect is defined by a positive entropy change. As an interesting example, Ni<sub>2</sub>MnGa is a material that exhibits the inverse effect for applied magnetic fields below 1 T while it shows the conventional effect for higher field strengths. However, there are other NiMn-based Heusler-alloys showing the inverse magnetocaloric effect for the whole range of the studied magnetic fields [68].

Some general formulations of the magnetocaloric effect are given here, following the deduction in [68] and [71]. In general, a system can be described using generalised displacement variables  $\{\mathbf{X}_i\}$ ,  $i = 1, \dots, n$  and their corresponding conjugated generalised forces or fields  $\{\mathbf{x}_i\}$ ,  $i = 1, \dots, n$ . For example, the conjugated fields for the displacement variables volume, magnetisation and polarisation are pressure, magnetic field and electric field, respectively. The internal energy of the examined system is then

$$U = U(S, \{\mathbf{X}_i\}), \quad (6.2)$$

with  $S$  being the entropy of the system. The temperature as the conjugated variable to the entropy is defined as

$$T = \left( \frac{\partial U}{\partial S} \right)_{\{\mathbf{X}_i\}} \quad (6.3)$$

and the other conjugated general forces or fields are given by

$$\mathbf{x}_i = \left( \frac{\partial U}{\partial \mathbf{X}_i} \right)_{S, \{\mathbf{X}_{j \neq i}\}}. \quad (6.4)$$

The tensorial product  $\mathbf{x}_i \cdot d\mathbf{X}_i$  describes the work connected with a differential change of the generalised displacement caused by the corresponding generalised field.

The dependence of  $\{\mathbf{X}_i\}$  on the entropy gives rise to the observed caloric effects, thus leading to

$$dS = \frac{C}{T}dT + \sum_{i=1}^n \left( \frac{\partial \mathbf{X}_i}{\partial T} \right)_{\mathbf{x}_j=1,\dots,n} \cdot d\mathbf{x}_i, \quad (6.5)$$

making use of the definition of the heat capacity

$$\left( \frac{\partial S}{\partial T} \right)_{\mathbf{x}_j=1,\dots,n} = \frac{C}{T} \quad (6.6)$$

and the generalised Maxwell relations

$$\left( \frac{\partial S}{\partial \mathbf{x}_i} \right)_{T, \mathbf{x}_j \neq i} = \left( \frac{\partial \mathbf{X}_i}{\partial T} \right)_{\mathbf{x}_j=1,\dots,n}. \quad (6.7)$$

The isothermal change of entropy by changing a generalised field  $\mathbf{x}_i$  from a value 0 to  $\mathbf{x}_{i,f}$  is given by

$$\Delta S_{0 \rightarrow \mathbf{x}_{i,f}} = \int_0^{\mathbf{x}_{i,f}} \boldsymbol{\xi}_i \cdot d\mathbf{x}_i, \quad (6.8)$$

while the adiabatic temperature change is described by

$$\Delta T_{0 \rightarrow \mathbf{x}_{i,f}} = - \int_0^{\mathbf{x}_{i,f}} \frac{T}{C} \boldsymbol{\xi}_i \cdot d\mathbf{x}_i, \quad (6.9)$$

with  $\boldsymbol{\xi}_i = \left( \frac{\partial \mathbf{X}_i}{\partial T} \right)_{\mathbf{x}_j=1,\dots,n}$ . The function  $\boldsymbol{\xi}_i$  is called response function and quantifies entropy changes resulting from ordering and disordering effects induced by the corresponding field [68]. For the magnetocaloric effect, the relevant field is the magnetic field  $\mu_0 H$ , the generalised displacement is the magnetisation  $M$  and the response function is described by  $\xi_M = \left( \frac{\partial M}{\partial T} \right)_{H,\dots}$ . The isothermal entropy and adiabatic thermal changes are then given by

$$\Delta S_{0 \rightarrow H_f} = \mu_0 \int_0^{H_f} \xi_M \cdot dH \quad (6.10)$$

and

$$\Delta T_{0 \rightarrow H_f} = -\mu_0 \int_0^{H_f} \frac{T}{C} \xi_M \cdot dH. \quad (6.11)$$

In [68] it is pointed out that the response function  $\xi_M$  in general is negative, giving

the conventional magnetocaloric effect. Nevertheless, positive values for the response function are not thermodynamically forbidden, which in turn gives rise to the inverse magnetocaloric effect where a magnetic field causes increasing entropy and decreasing temperature.

For magnetostructural phase changes where magnetic and structural changes occur, near the transition the magnetisation can be described as [68]:

$$M(H, T) = M_0 + \Delta M(H) \mathcal{F} \left[ \frac{T - T_t(H)}{\Delta T(H)} \right]. \quad (6.12)$$

$M_0$  is assumed to be constant independent of all temperature and field dependencies of the magnetisation outside the transition region and  $\Delta M$  is the change of magnetisation when switching between the low temperature and high temperature phases of the Heusler compound.  $\mathcal{F}$  is a function that varies between 0 and 1 in the interval  $\Delta T(H)$  and  $T_t$  is the estimated transition temperature which is usually taken from experimental magnetisation curves. For an ideal transition no hysteresis would occur leading to  $\Delta T \rightarrow 0$  and  $\lim_{\Delta T \rightarrow 0} \mathcal{F} = \Theta(T - T_t)$ . For the isothermal entropy change one gets

$$\Delta S = \begin{cases} -\frac{\mu_0 \Delta M}{|\alpha|} & \text{for } T \in [T_t(0), T_t(H)], \\ 0 & \text{for } T \notin [T_t(0), T_t(H)], \end{cases} \quad (6.13)$$

with  $\alpha = \frac{dT_t}{dH}$ .  $\alpha$  is related to the magnetic analogon of the Clausius-Clapeyron equation

$$\frac{dT_t}{dH} = -\mu_0 \frac{\Delta M}{\Delta S_t}, \quad (6.14)$$

which indicates that the field-induced entropy change corresponds to the transition entropy change  $\Delta S_t$  [68, 72]. The shift of the transition temperature  $T_t(H)$  with the magnetic field is

$$\Delta T_t = T_t(H) - T_t(0) = -\mu_0 \frac{\Delta M}{\Delta S_t} H. \quad (6.15)$$

For  $\Delta M > 0$  and  $\alpha > 0$  the conventional magnetocaloric effect is present, while for  $\Delta M < 0$  and  $\alpha < 0$  the inverse magnetocaloric effect is observed [68]. The inverse effect can occur, for example, if the magnetisation in the lower temperature phase is lower than

that of the higher temperature phase. The maximal change of temperature is given by

$$\Delta T_{\max} \simeq \frac{T \Delta S_t}{C}. \quad (6.16)$$

Usually, magnetostructural transitions can be observed over a certain temperature range, which can be traced back to the existence of composition gradients, defect structures, etc.

The experimental determination of the field induced entropy change for a temperature  $T$  can be facilitated by the measurement of the magnetisation  $M$  as a function of the field  $H$ . In principal, this corresponds to numerically integrating equation (6.10) [71]. However, in practice, such a procedure would introduce a significant error in the result. Therefore, calculating the entropy change for an average temperature in an interval  $T_{av} = (T_u - T_l)/2$  by measuring two magnetisation isotherms at the temperatures  $T_u$  and  $T_l$  is the method of choice [71]:

$$\Delta S_M(T_{av})_{\Delta H} = \int_{H_I}^{H_F} \left( \frac{\partial M(H)_{T_{av}}}{\partial T} \right)_H dH \quad (6.17)$$

with  $\Delta H = H_F - H_I$ . Another way to determine the entropy change would include the determination of the heat capacity [71]:

$$S(T)_H = \int_0^T \frac{C(T)_H}{T} dT + S_{0,H}, \quad (6.18)$$

with  $S_{0,H}$  as the zero-temperature entropy. The magnetic entropy change for  $\Delta H$  can be calculated as the isothermal difference of equation (6.18) for  $H = H_I$  and  $H = H_F$ :  $\Delta S_M(T)_{\Delta H} = [S(T)_{H_F} - S(T)_{H_I}]_T$ . The adiabatic temperature change can also be calculated as  $\Delta T_{ad}(T)_{\Delta H} \cong [T(S)_{H_F} - T(S)_{H_I}]_S$ , for details see [71].

Temperature dependent measurements of the magnetisation reveal some properties of the investigated Heusler alloys. In figure 6.6 the magnetisation of a NiMnIn Heusler is plotted with respect to the temperature. From the shape of the magnetisation curve a number of important temperature regions can be deduced. When decreasing the temperature of the austenitic Heusler, the magnetisation rises as the ferromagnetic ordering sets in. Upon further decrease of the temperature, at some point the magnetisation also decreases, which marks the beginning of the martensitic transformation. When the transformation is finished, the magnetisation curve reaches a local minimum. Finally,



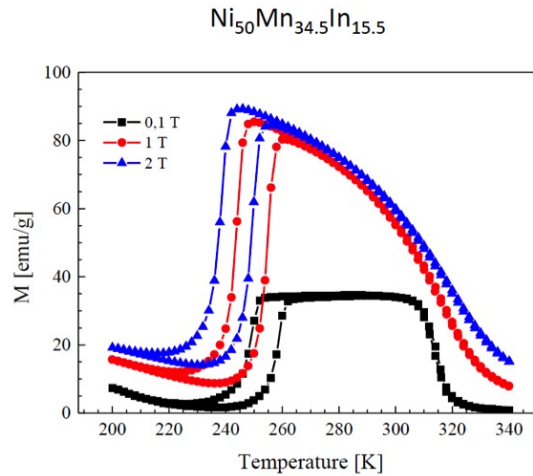


Figure 6.6.: Field cooling and field heating magnetisation measurements of a  $\text{Ni}_{50}\text{Mn}_{34.5}\text{In}_{15.5}$  Heusler compound. Different colours correspond to different magnetic fields in which the measurements were conducted. Data provided by TU Darmstadt.

an increase of the magnetisation is seen, as the ferromagnetic ordering of the martensitic state occurs. When going through this process in the reverse direction by heating up the sample, a hysteresis can be clearly seen. From such measurements, the transformation temperature  $T_t$  can be deduced.

As mentioned in section 6.2, the valence electron concentration per atom ( $e/a$ ) governs the temperature range in which the martensitic transformation occurs. Thus, the transformation temperature is different for Heusler compounds of different elemental composition and also for different concentrations of the constituents if non-stoichiometric compounds are taken into consideration.

## 6.4. Ferroic cooling

The investigations of Heusler alloys reported in this work are part of a priority programme of the “Deutsche Forschungsgemeinschaft” (DFG), which deals with the question of how to use diffusionless transformations in cooling applications most efficiently. The method of choice turned out to be the usage of materials exhibiting a magnetocaloric effect as described in section 6.3. Therefore, a number of different Heusler compounds are in the focus of investigation in order to determine their magnetic properties and

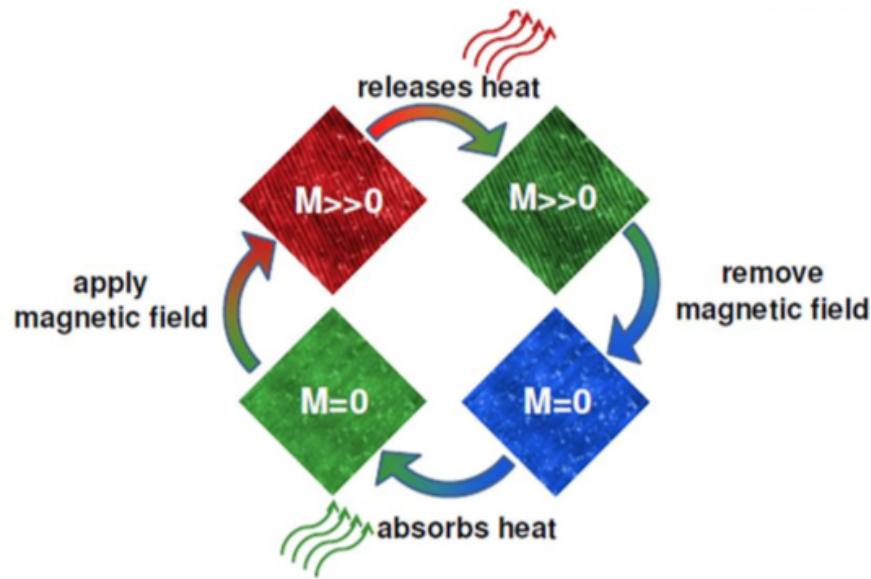


Figure 6.7.: Schematic drawing of the principle of a cooling cycle. Adopted from [73]. The details of the magnetocaloric cooling cycle are described in the text.

suitability for the aforementioned task.

Figure 6.7 shows the principle of a magnetocaloric cooling cycle. Starting at the bottom left, the material is in its austenitic state at a certain temperature. Applying a magnetic field induces the martensitic transformation. For a material exhibiting the conventional magnetocaloric effect, this includes a decrease of the entropy and an increase of temperature. This heat is released to an external reservoir (top right in the sketch). After removal of the external magnetic field, the material cools down as it transforms back in its austenitic state. It can then be connected to the reservoir which has to be cooled. For a material with inverse magnetocaloric properties, the effect of applying and removing the magnetic field would be interchanged.

This process is referred to as “ferroic cooling”. It is noteworthy that the possible temperature change achieved in such a process is in the range of a few Kelvin [73]. The application of this technique is considered to lie in the field of spintronics and nanotechnology.

The goal of the Bielefeld University’s project part was the production and investigation of the magnetic properties of different Heusler alloys. Furthermore, the possibility of the usage of multilayered systems incorporating materials with conventional and inverse

Table 6.1.: Overview of the investigated Heusler-alloys. The given stoichiometry is the nominal one as stated by the producing workgroup.  $T_t$  denotes the transition temperature between the martensitic and the austenitic phase of the Heusler-alloys. The column “Producer” mentions the institution where the respective sample was produced and the column “EMCD” states whether EMCD measurements were performed on the respective sample.

Sample	$T_t$	Producer	EMCD
Ni <sub>2</sub> MnSn	–	IFW Dresden	yes
Ni <sub>52</sub> Mn <sub>33.3</sub> Sn <sub>14.7</sub>	235 K	Uni Bielefeld	yes
Ni <sub>50</sub> Mn <sub>34.5</sub> In <sub>15.5</sub>	120 K	TU Darmstadt	yes
Ni <sub>2</sub> MnSn – Ni <sub>2</sub> MnGa double layer	–	Uni Bielefeld	yes
Ni <sub>49.4</sub> Mn <sub>36.9</sub> Sn <sub>13.7</sub> – gradient	290 K	Uni Bielefeld	yes
Ni <sub>41</sub> Co <sub>10.4</sub> Mn <sub>34.8</sub> Al <sub>13.8</sub>	348 K	Uni Bielefeld	no
Co <sub>2</sub> CrAl on GaAs	–	Uni Bielefeld	no
Ni <sub>56.1</sub> Mn <sub>17.3</sub> Ga <sub>26.6</sub> – gradient	290 K	Uni Bielefeld	no
Sn–Ga–Sn Heusler triple layer	–	Uni Bielefeld	no

magnetocaloric effects was in the focus of the investigation. The tasks reported in this work included the structural and elemental analysis of the produced materials using electron microscopical studies. Furthermore, the technique EMCD was applied to gain more knowledge about the magnetic properties of the investigated materials across the phase transition by performing in-situ EMCD studies while respective heating or cooling of the samples was conducted.

In the next section, an overview of the investigated samples is given, followed by the respective results.

## 6.5. Investigation of Heusler alloys

### 6.5.1. Overview of the investigated samples

A list of the investigated samples is given in table 6.1. The transition temperature  $T_t$  is given for each sample (if applicable), as well as the institution which has produced the respective material. All samples were grown on MgO as a substrate except one, which was grown on GaAs and is marked in the table as such. Furthermore, it is mentioned, whether EMCD measurements were performed on a sample. Those samples, on which EMCD experiments were conducted, are discussed in more detail in the following

subsections. For the other samples, a short discussion is given afterwards.

If not mentioned otherwise, the samples were prepared for TEM analysis by cutting and polishing. This procedure was followed by subsequent thinning using a Gatan PIPS ion mill system. Some of the samples were instead prepared using a focused ion beam (FIB) system (FEI Quanta 200 3D Dual-beam FIB), followed by subsequent milling using a TechnoorgLinda Gentlemill system.

All investigations were performed using a FEI Tecnai G<sup>2</sup> TF20 transmission electron microscope operated at 200 kV. It is equipped with an EDAX Octane SDD EDX detector and a Gatan GIF Tridiem imaging filter. In regular operating conditions, the magnetic field of the objective lens system is about 2 T. This has to be kept in mind for the investigation of the magnetocaloric effect, as this is the field applied to the Heusler samples during measurements.

For all samples reported in this work, a thorough structural and elemental analysis was performed. These investigations included standard TEM imaging, high resolution TEM imaging, acquisition of diffraction patterns, as well as energy dispersive X-ray (EDX) analyses and EELS analyses. Not only is this information important for characterising the Heusler alloys for possible ferroic cooling applications but also necessary for EMCD measurements, as these factors are of great influence on the detected EMCD signal.

The analysis of the EDX data was performed using the TEAM software version 4.2 by EDAX. The analysis of all images, diffraction patterns and EEL spectra was done using the Digital Micrograph software, in its version GMS 2.3 by Gatan.

### 6.5.2. Ni<sub>2</sub>MnSn and Ni<sub>52</sub>Mn<sub>33.3</sub>Sn<sub>14.7</sub>

The Ni<sub>2</sub>MnSn sample provided by the Leibniz Institute for Solid State and Materials Research (IFW) Dresden is ideally suited to compare the experiments with theoretical predictions as its nominal elemental composition is that of a stoichiometric full Heusler alloy. The sample produced at the Bielefeld University has a nominal composition which is not stoichiometric but as it would be used in ferroic cooling applications. Therefore, comparing the results of both samples, the applicability of the methods used for investigation can be studied.

An overview bright field TEM image of the Ni<sub>2</sub>MnSn sample provided by the IFW Dresden is shown in figure 6.8 a) and an overview of the Ni<sub>52</sub>Mn<sub>33.3</sub>Sn<sub>14.7</sub> sample provided by the University of Bielefeld in figure 6.8 b). The Bielefeld sample was prepared for

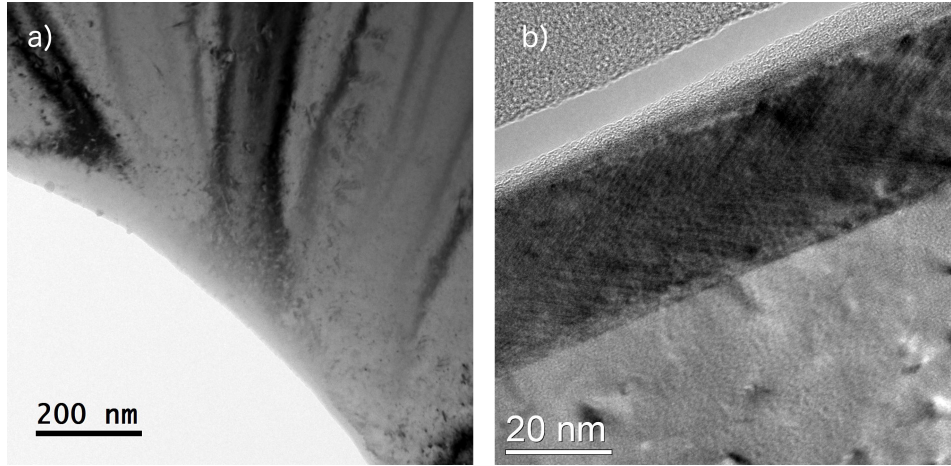


Figure 6.8.: a) Bright field TEM image of the investigated region of the IFW sample ( $\text{Ni}_2\text{MnSn}$ ). b) HRTEM image of the Bielefeld sample ( $\text{Ni}_{52}\text{Mn}_{33.3}\text{Sn}_{14.7}$ ). The bottom area shows the MgO substrate, in the central region of the image the 30 nm thick  $\text{Ni}_{52}\text{Mn}_{33.3}\text{Sn}_{14.7}$  layer is visible and the top region shows residual adhesive from the preparation process. In the Heusler layer the modulated structure of the martensitic phase is evident.

Table 6.2.: Comparison of the nominal and the experimentally determined elemental compositions of the two  $\text{Ni}_2\text{MnSn}$  samples.

	Ni [at%]	Mn [at%]	Sn [at%]
Nominal IFW:	50.00	25.00	25.00
IFW:	$57.30 \pm 5.70$	$24.94 \pm 2.50$	$17.76 \pm 1.80$
Nominal Bielefeld:	52.00	33.30	14.70
Actual Bielefeld:	$59.70 \pm 1.44$	$33.94 \pm 1.00$	$6.34 \pm 1.84$

TEM measurements using a FIB system, while the IFW sample was prepared by “conventional” polishing. It is evident from the images that the IFW sample is in its austenitic phase, while the Bielefeld sample shows a modulated (“fishbone-like”) structure typical for the martensitic phase. The diffraction patterns presented in figure 6.9 give rise to the same conclusion. Both samples were investigated at room temperature which indicates that for the two samples the transition temperature  $T_t$  is different.

The reason for this behaviour can be found in the different elemental composition of the two samples. Table 6.2 lists these elemental compositions as determined by EDX spectrometry and compares it to the nominal one. The IFW sample shows a slightly larger amount of Ni and a lower one of Mn and Sn compared to the nominal values.

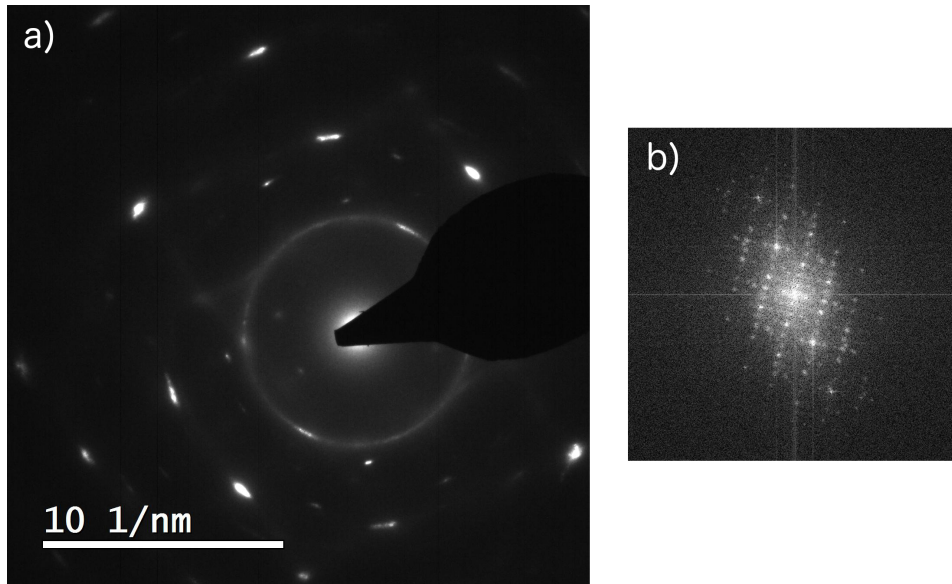


Figure 6.9.: a) Diffraction pattern of the austenitic  $\text{Ni}_2\text{MnSn}$  Heusler sample. b) Diffraction pattern of the martensitic  $\text{Ni}_{52}\text{Mn}_{33.3}\text{Sn}_{14.7}$  sample acquired by means of a FFT of a HRTEM image.

Furthermore, the Bielefeld sample has again a lower concentration of Sn compared to the nominal values while the Ni and Mn concentrations are higher. This would raise the transition temperature compared to the IFW sample (see also the middle panel of figure 6.4).

EMCD measurements of the two samples are compared in table 6.3. For each EMCD measurement the respective sample thickness is given. It was determined using low loss EELS and the log-ratio method. An example for the EMCD measurements on the IFW  $\text{Ni}_2\text{MnSn}$  Heusler alloy is shown in figures 6.10 and 6.11, which correspond to the measurement No. 7 in table 6.3. Background subtraction was performed using a power-law fit, alignment of the spectra was done by the integral over the post-edge background.

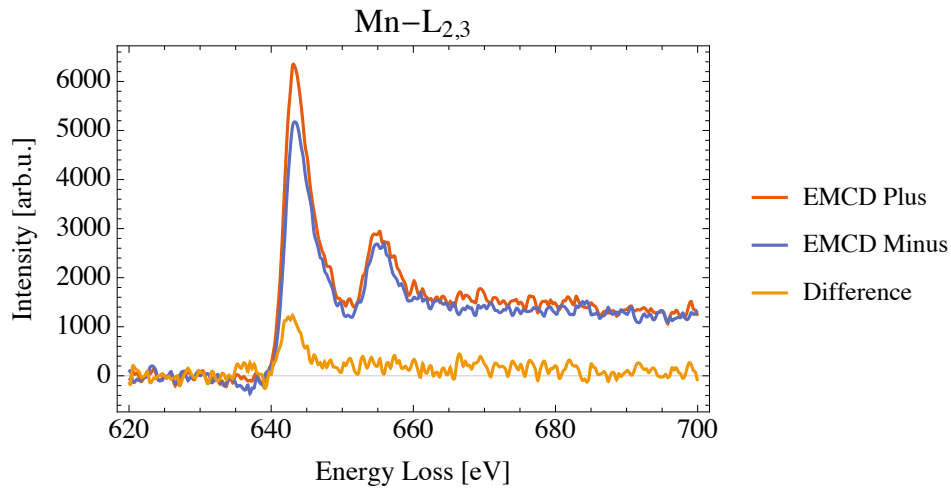
In figure 6.12 and 6.13 the experimentally determined values for the EMCD signal in the IFW sample are plotted and compared to the respective simulations. The simulations were performed using a simulation program developed at the Vienna University of Technology [11]. The actual thickness of the sample lies within a window of 10% around the value determined using low-loss EELS. The standard deviation for the EMCD signal was determined by subsequent propagation of the calculated standard deviations of a

Table 6.3.: Measured EMCD signals on the Mn-L<sub>2,3</sub> edge and the Ni-L<sub>2,3</sub> edge of the two investigated Ni<sub>2</sub>MnSn samples.

IFW sample	Mn: 640 eV	Ni: 855 eV	
Pos.	EMCD signal	EMCD signal	Thickness
1	2.2%	0.9%	28 nm
2	-1.6%	2.3%	28 nm to 43 nm
3	9.3%	2.2%	43 nm
4	-8.8%	9.5%	38 nm
5	-11.9%	-3.0%	29 nm
6	23.1%	6.3%	42 nm
7	19.9%	-0.5%	42 nm
8	19.3%	13.7%	38 nm
9	5.1%	-12.5%	62 nm

Bielefeld sample	Mn: 640 eV	Ni: 855 eV	
Pos.	EMCD signal	EMCD signal	<i>d</i>
1	19.0%	-12.0%	for all pos. ca. 45 nm
2	-2.0%	13.0%	
3	5.0%	5.0%	
4	12.0%	-4.0%	
5	7.0%	-3.0%	
6	4.0%	-16.0%	
7	2.0%	12.0%	

Figure 6.10.: EMCD measurements on the Mn-L<sub>2,3</sub> edge of the Ni<sub>2</sub>MnSn Heusler sample provided by the IFW Dresden. Background subtraction was performed and the spectra were aligned by integral of the post-edge background.

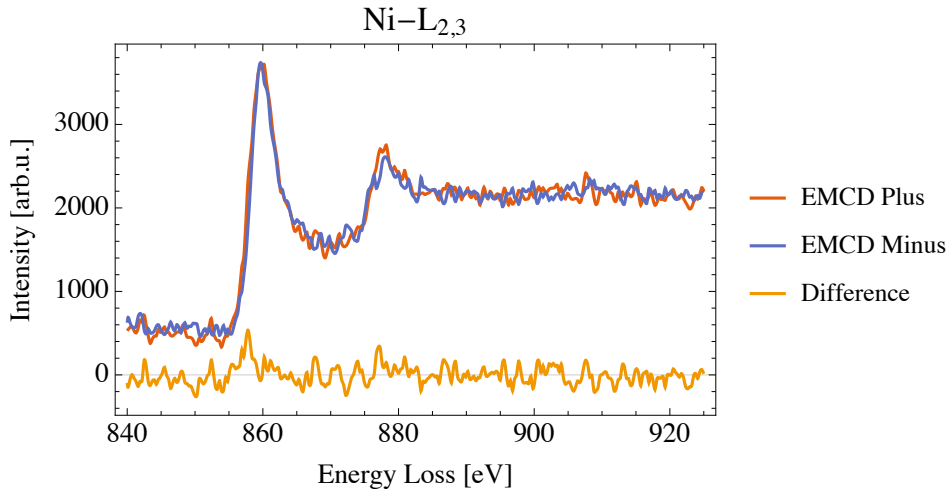


Figure 6.11.: EMCD measurements on the Ni-L<sub>2,3</sub> edge of the IFW Ni<sub>2</sub>MnSn sample. Background subtraction was performed and the spectra were aligned by integral of the post-edge background.

pre-edge background region of the measured spectra. The difference between the two figures is that a different systematic row was set up for the measurements no. 6 to 9 in table 6.3. The measurements conducted with the systematic row including the (2 2 0) reflection (figure 6.12) show a quite good agreement of the Mn EMCD signal with the predictions of the thickness dependence. The Ni EMCD signal, on the contrary, is quite different from the simulated values. The measurements shown in figure 6.13 show a similar behaviour. The Mn measurements follow in general the shape of the simulation. The Ni measurements exhibit far more deviation from the calculated numerical values. Figure 6.14 shows the experimentally determined EMCD signals of the Bielefeld sample in comparison to the simulation. In this case, some of the experimental values for Mn fit to the simulations. Nevertheless, there are more measurements that deviate from the predicted values than with the stoichiometric Ni<sub>2</sub>MnSn sample. For the EMCD measurements at the Ni L<sub>2,3</sub>-edge, the results are quite similar to those of the stoichiometric sample. Only a few measurements correspond to the simulated values.

### 6.5.3. Ni<sub>50</sub>Mn<sub>34.5</sub>In<sub>15.5</sub>

In figure 6.15 an overview of the investigated area of the Ni<sub>50</sub>Mn<sub>34.5</sub>In<sub>15.5</sub> sample is shown together with a high resolution zoom in of the region. The lattice planes are clearly vis-



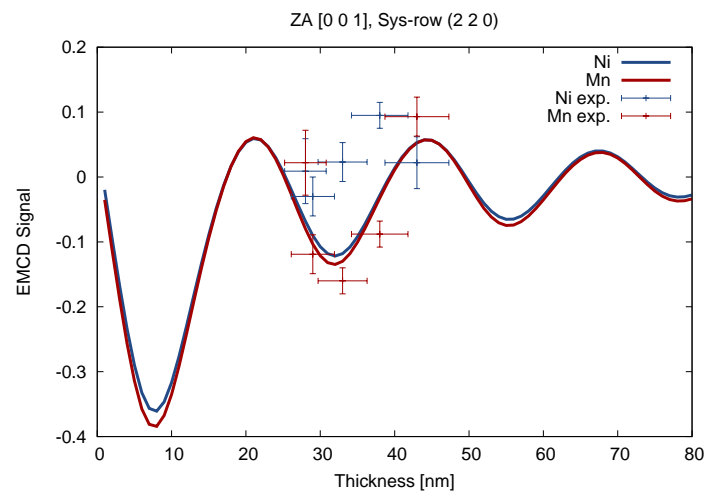


Figure 6.12.: Comparison of the experimentally determined EMCD values of the  $\text{Ni}_2\text{MnSn}$  sample provided by the IFW Dresden with the calculated prediction of the thickness dependence of the EMCD signal.

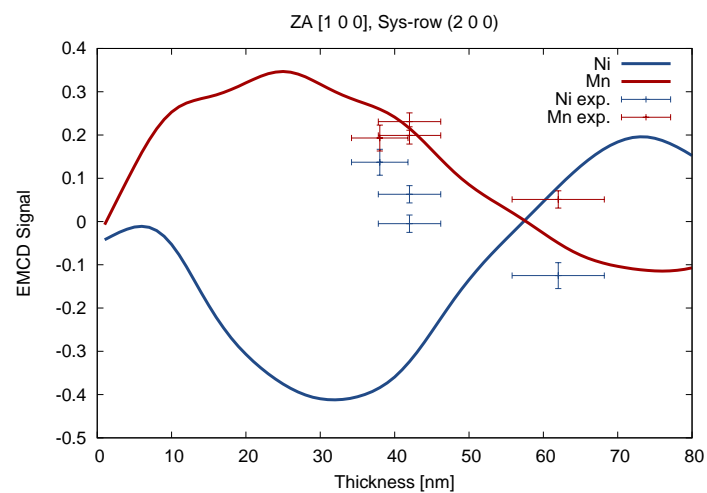


Figure 6.13.: Comparison of the experimentally determined EMCD values of the  $\text{Ni}_2\text{MnSn}$  sample provided by the IFW Dresden with the calculated prediction of the thickness dependence of the EMCD signal.

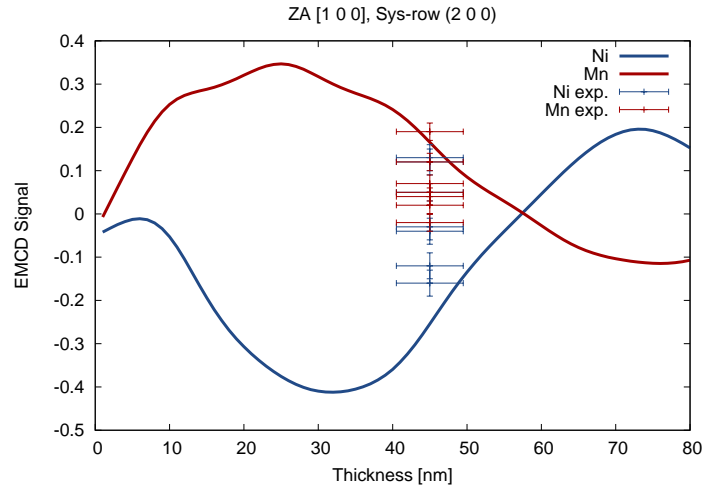


Figure 6.14.: Comparison of the experimentally determined EMCD values of the  $\text{Ni}_{52}\text{Mn}_{33.3}\text{Sn}_{14.7}$  sample provided by the Bielefeld University with the calculated prediction of the thickness dependence of the EMCD signal.

Table 6.4.: Nominal elemental composition of the NiMnIn Heusler alloy compared to the experimentally determined compositions, which were acquired using EDX spectrometry at different positions on the sample.

	Ni [at%]	Mn [at%]	In [at%]
Nominal:	50	34.5	15.5
EDX 2:	$57.45 \pm 5.86$	$19.35 \pm 2.78$	$23.20 \pm 4.20$
EDX 3:	$66.50 \pm 4.53$	$17.14 \pm 2.10$	$16.36 \pm 4.14$

ible in the HRTEM image and no modulations, which are typical for the martensitic phase, are present. This indicates that the Heusler alloy is in its austenitic state at room temperature. This is also indicated by the diffraction pattern shown in figure 6.16. Using EDX analysis, the elemental composition of the sample in two different regions was determined, see table 6.4. The measurements show that in contrast to the nominal composition provided by the TU Darmstadt, the Mn concentration is (significantly) lower than expected, while the Ni concentration is enhanced. Furthermore, the In concentration is very inhomogeneously distributed in the sample. This suggests that the temperature of the martensitic transition  $T_t$  is changed compared to that of the nominal Heusler alloy. Comparing with figure 6.4, a higher amount of In would suggest a decreased transition temperature and vice versa. Furthermore, due to the inhomogeneous

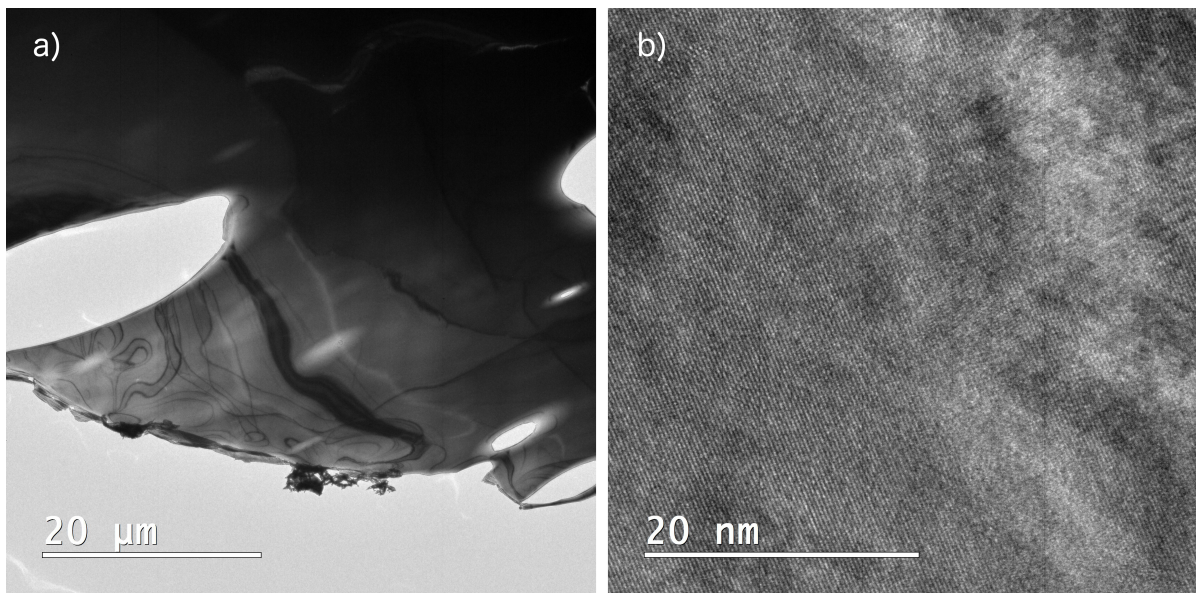


Figure 6.15.: a) Bright field TEM image of the investigated sample region of the  $\text{Ni}_{50}\text{Mn}_{34.5}\text{In}_{15.5}$  sample. The dark contrasts and lines visible in the image are bending contours, the brighter regions indicate smaller sample thickness than the surrounding area. b) High resolution TEM image of the investigated area. The lattice planes are visible. This indicates on the one hand that the sample is crystalline in this region, on the other hand that the sample is in its austenitic state at room temperature as the typical martensitic modulations of the lattice planes are missing.

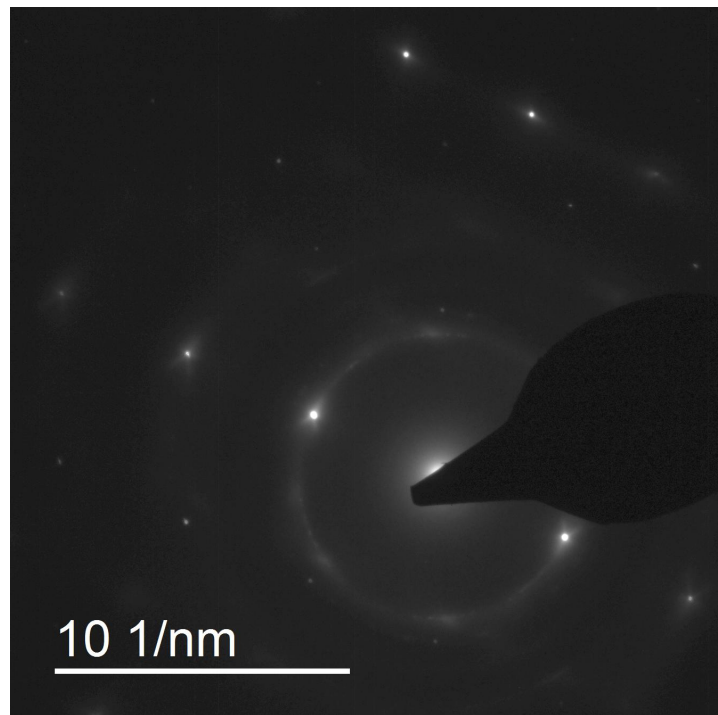


Figure 6.16.: Diffraction pattern of the  $\text{Ni}_{50}\text{Mn}_{34.5}\text{In}_{15.5}$  sample acquired at a camera length of 300 mm. The pattern shows the systematic row conditions that were used for the EMCD measurements. According to the pattern, the sample is slightly tilted out of the the  $[001]$  zone axis and the systematic row includes the  $(2\bar{2}0)$  reflection.

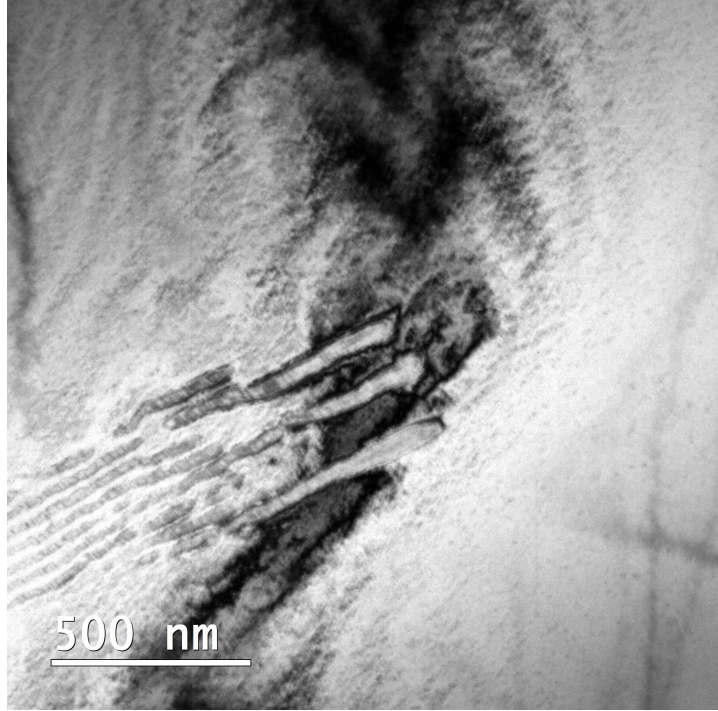


Figure 6.17.: Bright field image of the  $\text{Ni}_{50}\text{Mn}_{34.5}\text{In}_{15.5}$  sample after cooling down to 120 K. The streaks running from the center to the bottom left part of the image are the sample regions which already transformed to the martensitic phase.

elemental distribution, the transition is expected to occur in different sample regions at varying temperatures.

In figure 6.6 field cooling and field heating magnetisation curves, measured in the workgroup of O. Gutfleisch at the TU Darmstadt, are shown. The temperature dependent magnetisation curves measured at different magnetic fields exhibit a thermal hysteresis between 220 K and 260 K. As already mentioned in section 6.3, from magnetisation measurements the martensitic transition temperature  $T_t$  can be determined as  $\sim 240$  K.

For further investigations, the sample was cooled down below the transition temperature  $T_t$  using a Gatan cooling sample holder. In figure 6.17 a bright field image of the investigated sample region at a temperature of 120 K is shown. There are some “lamellae” or streaks visible in the image. These are the sample regions which already transformed to the martensitic state, while the rest of the sample is still in its austenitic phase. There are several reasons, why not the whole sample has transformed

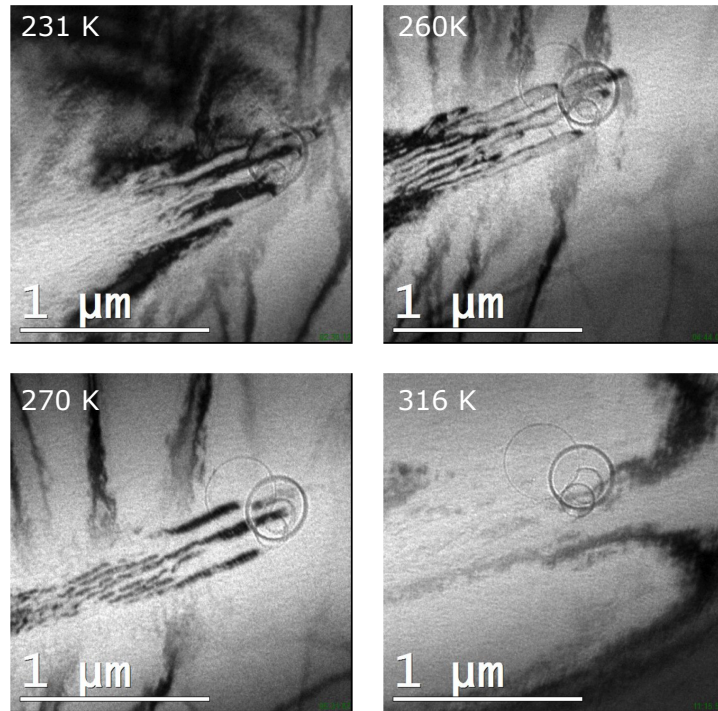


Figure 6.18.: Series of bright field image of the  $\text{Ni}_{50}\text{Mn}_{34.5}\text{In}_{15.5}$  sample taken while heating up to room temperature. The streaks representing the martensitic phase of the sample become fainter while heating up. This indicates that the martensitic phase is transforming back to the austenitic state.

already. One is that, as mentioned above, the elemental composition was determined to be different from the nominal one and quite inhomogeneous. Thus, the actual transition temperature has changed as its value strongly depends on the composition of the Heusler compound. Another fact that has an influence on the observed phase transformation, is that the temperature is measured at the tip of the sample holder and not at the sample itself. Therefore, due to thermal conduction effects, the sample's actual temperature is somewhat higher than the one stated by the sample holder cooling control unit.

Figure 6.18 shows a series of bright field images, recorded during heating the sample back to room temperature. From these images it can be seen that the martensitic streaks are shrinking and fainting until they vanish completely at room temperature. This would indicate that the whole sample region has transformed back to its austenitic state.

EMCD experiments were performed in the TEM mode using a converged beam with a convergence angle of about 1 mrad. The SEA was positioned at the two EMCD positions on the Thales circle spanned by the  $\mathbf{0}$  and  $\mathbf{G}$  reflection of the systematic row (see figure

Table 6.5.: Measured EMCD signals on the Mn-L<sub>2,3</sub> edge and the Ni-L<sub>2,3</sub> edge of the Ni<sub>50</sub>Mn<sub>34.5</sub>In<sub>15.5</sub> sample. The sample temperature is given in the first column, “RT” denotes room temperature.

Sample pos. 1	Mn: 640 eV	Ni: 855 eV	
$T$	EMCD signal	EMCD signal	Comment
RT	0%	-2%	
RT	-13%	-9%	
RT	16%	20%	after cooling
RT	15%	12%	after cooling
RT	-2%	-2%	after cooling
120 K	17%		bad S/N ratio
120 K	5%	-5%	bad S/N ratio
120 K	10%	13%	
240 K	-18%	-24%	
240 K	-7%	-1%	
240 K	7%	-9%	
Sample pos. 2	Mn: 640 eV	Ni: 855 eV	
$T$	EMCD signal	EMCD signal	Comment
RT	1%	0%	
RT	16%	2%	
RT	11%	2%	
RT	1%	4%	after cooling
RT	5%	-3%	after cooling
RT	7%	-2%	after cooling
160 K	2%	4%	
160 K	-2%	8%	bad S/N ratio
160 K	1%	2%	bad S/N ratio

6.16 as well as the nomenclature in figure 5.3 and section 5.3). The beam was converged in order to improve the signal to noise ratio and to reduce the acquisition time. Usually, the maximal beam convergence in the experiments was chosen such that  $\alpha \approx \beta$ , with  $\alpha$  being the convergence semi-angle and  $\beta$  the collection semi-angle. The sample thickness was determined using low loss EEL spectra applying the log-ratio method [3]. The thickness was found to be between 30 nm and 35 nm. Measurements were done at room temperature as well as during cooling the sample. Table 6.5 gives an overview of the measured EMCD signals. The measurements at sample position 1 were performed in a systematic row condition including the  $(2\bar{2}0)$  reflection, while those at position 2 included the  $(200)$  reflection in the systematic row. The values for the EMCD signal



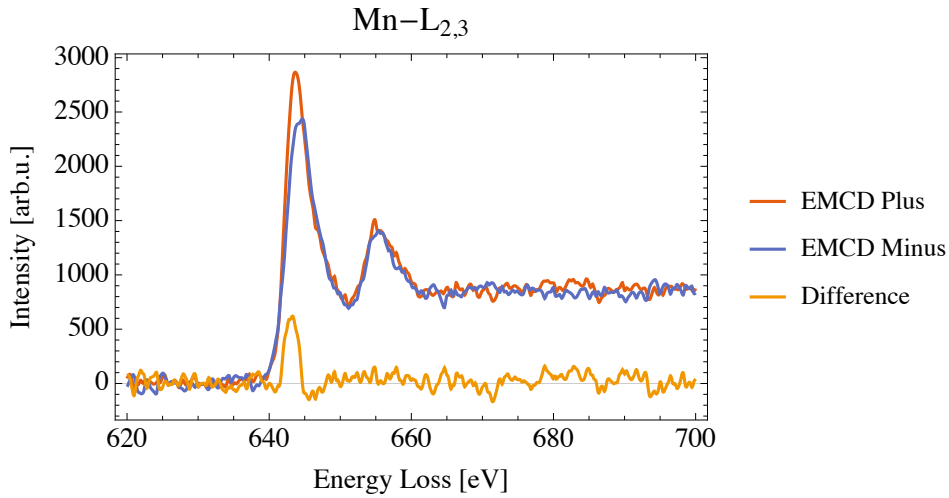


Figure 6.19.: EEL spectra of the Mn- $L_{2,3}$  edge of  $\text{Ni}_{50}\text{Mn}_{34.5}\text{In}_{15.5}$  acquired at the two EMCD positions as given in figure 5.3 (EMCD Plus, EMCD Minus) and the difference spectrum representing the measured EMCD effect. The spectra were acquired at room temperature and exhibit an effect of  $\sim 16\%$ . Background subtraction was performed and the spectra were aligned by the integral of the post-edge background.

were calculated using the formula  $2 \cdot (\sigma^+ - \sigma^-) / (\sigma^+ + \sigma^-)$ , see also section 5.2. From the values given in the table, it can be seen that for measurements performed at the same temperature, in general there are similar results. However, some of the results show EMCD signals far off the other measurements. Furthermore, the S/N ratio is an important factor for the reliability of the calculated EMCD signal. The S/N ratio is worse especially when investigating the cooled sample as the sample stability is also worse when using the cooling sample holder, which requires shorter acquisition times. Keeping all this in mind, one has to perform a large number of EMCD measurements in order to see a trend in the results. In figure 6.19 one of the EMCD measurements at room temperature is shown exemplarily. The spectra of the Mn- $L_{2,3}$  edge taken at the two EMCD positions can be seen, as well as the difference spectrum clearly exhibiting the EMCD effect. The pre-edge background of the spectra was subtracted using a power-law fit [3] and they were aligned by the integral of the post-edge background. The Ni- $L_{2,3}$  edge EMCD spectrum of the same measurement is shown in figure 6.20. In figure 6.21 the experimentally determined EMCD signals of sample position 1 at room temperature are shown in a plot together with a calculation of the thickness dependence of the



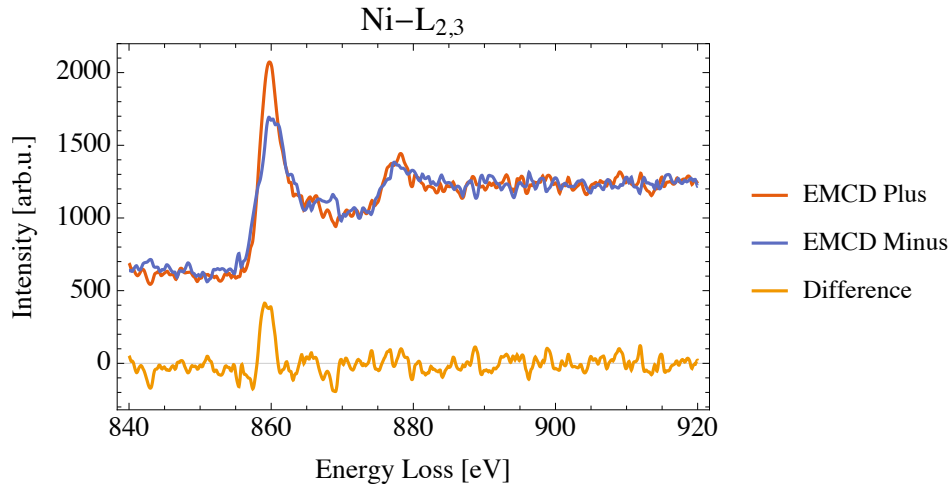


Figure 6.20.: EEL spectra of the Ni- $L_{2,3}$  edge of  $\text{Ni}_{50}\text{Mn}_{34.5}\text{In}_{15.5}$  acquired at the two EMCD positions (EMCD Plus, EMCD Minus) and the difference spectrum representing the measured EMCD effect. The spectra were acquired at room temperature and exhibit an effect of  $\sim 20\%$ . The spectra were aligned by the integral of the post-edge background.

EMCD signal. In figure 6.22 the same is done for the room temperature measurements at sample position 2. In both cases it can be seen that the experimental values differ from the calculated EMCD signal. Nevertheless, a trend can be identified in both cases. In figure 6.22 the values for the EMCD signal for the Ni- $L_{2,3}$  edge and the Mn- $L_{2,3}$  edge are quite similar, which is also the case in the simulation. In figure 6.21 it can be seen that the values for the Mn edge are higher than that for the Ni edge. The actual values for Mn in the experiment are somewhat lower than the prediction of the simulation. For the Ni EMCD signals, the simulation predicts a negative signal of the same magnitude as the positive signal in Mn but the experiments show that the actual values all lie around 0%.

#### 6.5.4. $\text{Ni}_2\text{MnSn}$ – $\text{Ni}_2\text{MnGa}$ double layer

A sample consisting of a Heusler double layer was produced in order to investigate its behaviour at the interface as well as the effect of a Pt barrier layer. The aim was to create two clearly separated Heusler layers without interdiffusion. The sample consists of a MgO substrate on which a sequence of a 30 nm  $\text{Ni}_2\text{MnSn}$  Heusler layer, a 1.5 nm Pt barrier layer and a 30 nm  $\text{Ni}_2\text{MnGa}$  Heusler layer was grown. Figure 6.23 shows an

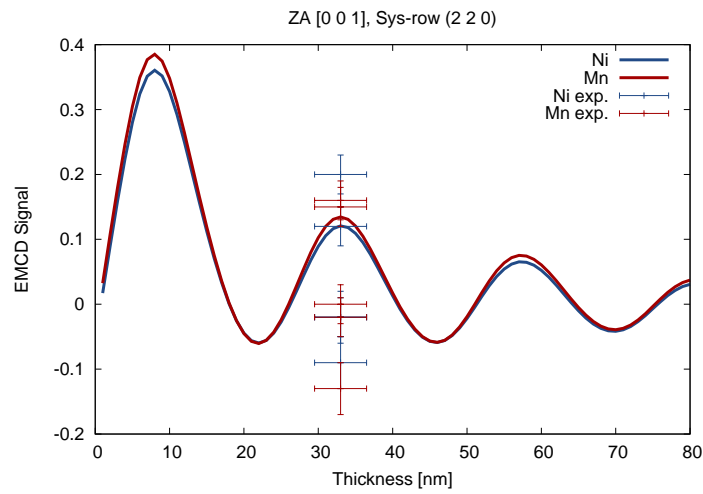


Figure 6.21.: Calculation of the thickness dependence of the EMCD signal in austenitic Ni<sub>2</sub>MnIn. The simulations were performed for a sample slightly tilted out of zone axis [001] and a systematic row condition including the (220) reflection. The experimentally determined values for the EMCD signal given in table 6.5 are marked in the plot.

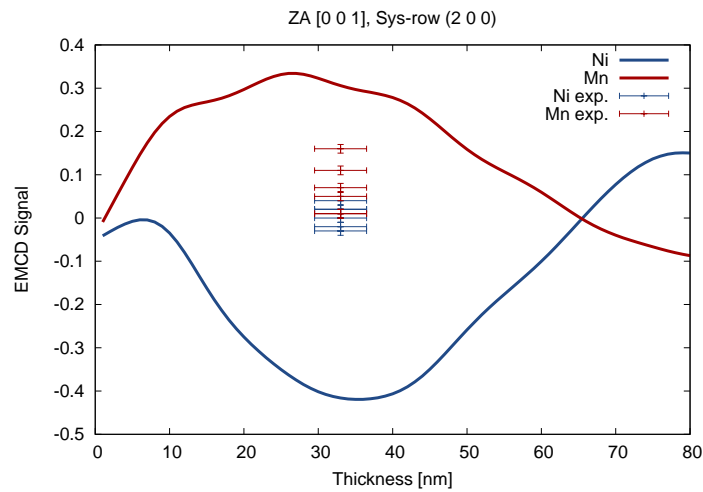


Figure 6.22.: Calculation of the thickness dependence of the EMCD signal in austenitic Ni<sub>2</sub>MnIn. The simulations were performed for a sample slightly tilted out of zone axis [001] and a systematic row condition including the (200) reflection. The experimentally determined values for the EMCD signal given in table 6.5 are marked in the plot.

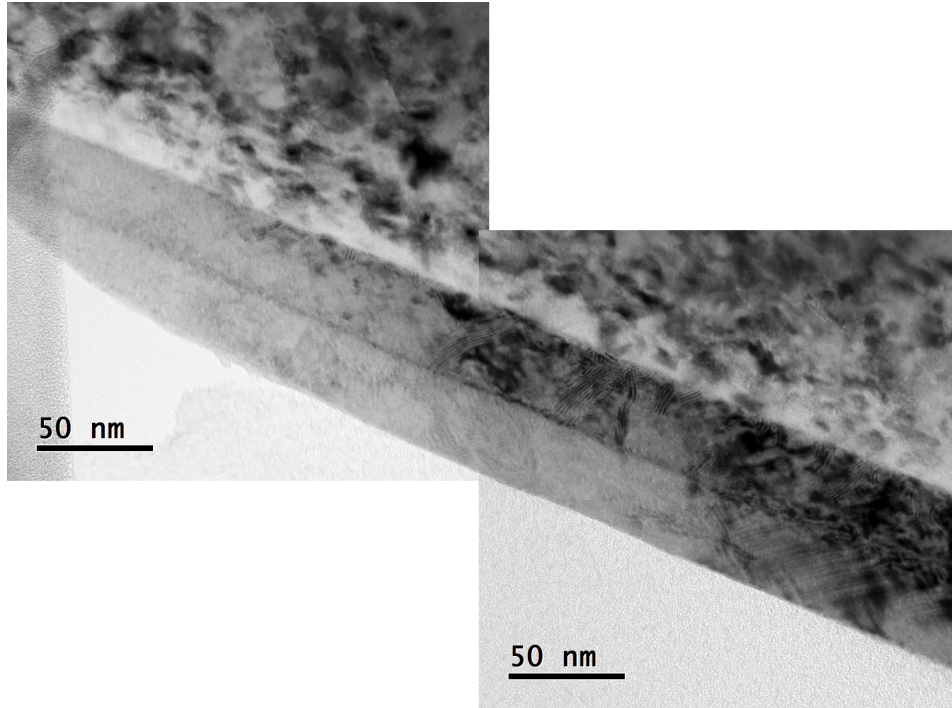


Figure 6.23.: TEM bright field images showing the investigated area of the  $\text{Ni}_2\text{MnSn}$  –  $\text{Ni}_2\text{MnGa}$  double layer sample. On the top the MgO substrate is visible.

overview of the investigated sample. It can be seen that both Heusler layers consist of martensitic and austenitic regions at room temperature. From a high resolution TEM image shown in figure 6.24 it is evident that the martensitic phase can extend across the Pt-barrier layer.

An EDX linescan was performed in order to investigate the actual elemental composition of the Heusler layers but also to verify the functionality of the Pt barrier layer. The results of this linescan are shown in figure 6.25 and in table 6.6. Although the martensitic

Table 6.6.: Comparison of the nominal and the experimentally determined elemental composition of the Heusler layers in the  $\text{Ni}_2\text{MnSn}$  –  $\text{Ni}_2\text{MnGa}$  double layer sample.

	NiMnSn layer			NiMnGa layer		
	Ni [at%]	Mn [at%]	Sn [at%]	Ni [at%]	Mn [at%]	Ga [at%]
Nominal:	50.0	25.0	25.0	50.0	25.0	25.0
EDX:	$44.0 \pm 2.0$	$30.0 \pm 1.5$	$26.0 \pm 2.4$	$59.0 \pm 2.6$	$18.0 \pm 1.9$	$23.0 \pm 2.0$

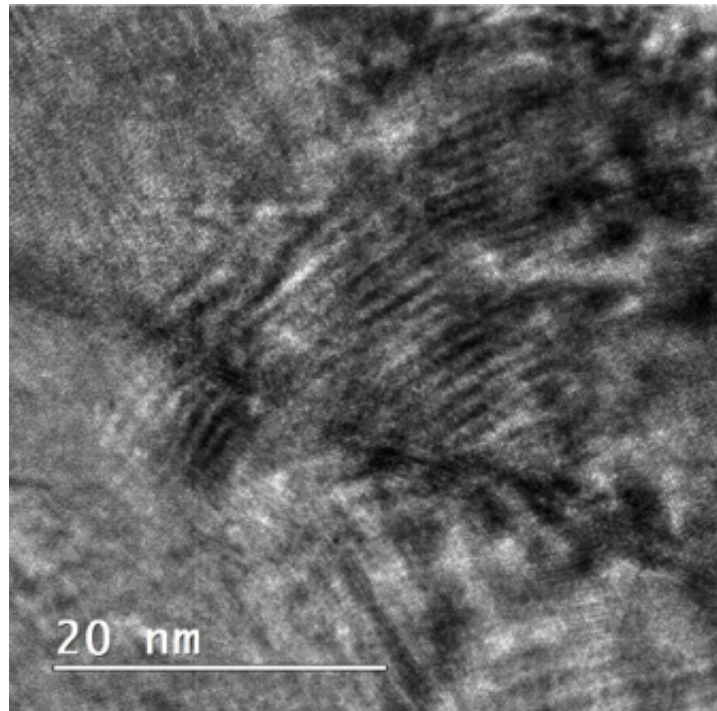


Figure 6.24.: High resolution TEM image of the  $\text{Ni}_2\text{MnSn}$  –  $\text{Ni}_2\text{MnGa}$  double-layer. The martensitic nucleus of the  $\text{Ni}_2\text{MnSn}$  Heusler extends across the Pt barrier layer into the  $\text{Ni}_2\text{MnGa}$  Heusler layer.

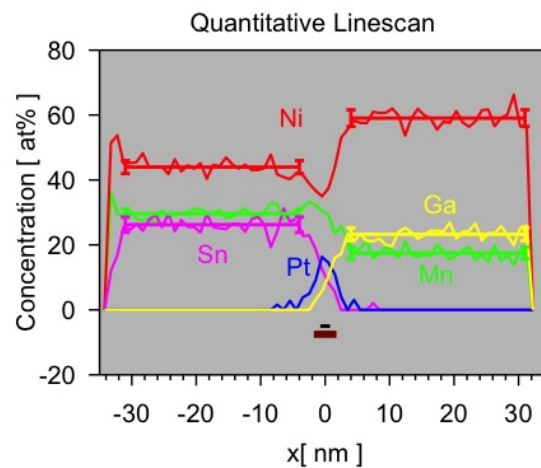


Figure 6.25.: Results of an EDX linescan across the two Heusler layers and the Pt barrier layer of the  $\text{Ni}_2\text{MnSn}$  –  $\text{Ni}_2\text{MnGa}$  double layer sample. It can be seen that the Pt layer efficiently prevents diffusion between the two Heusler layers.

Table 6.7.: Measured EMCD signals on the Mn-L<sub>2,3</sub> edge and the Ni-L<sub>2,3</sub> edge of the two Heusler layers.

Ni <sub>2</sub> MnSn layer	Mn: 640 eV	Ni: 855 eV
Temp.	EMCD signal	EMCD signal
RT	11.8%	-11.4%
473 K	14.2%	15.5%
Ni <sub>2</sub> MnGa layer	Mn: 640 eV	Ni: 855 eV
Temp.	EMCD signal	EMCD signal
RT	11.7%	9.9%
473 K	-17.6%	0.3%

nucleus extends across the Heusler layer interface, the EDX scan shows that no diffusion between the two layers is present, thus illustrating the functionality of the Pt barrier. The sample was heated up to 473 K but no changes in the structure was visible. This leads to the assumption that the local elemental composition in the martensitic regions is such that the transition temperature  $T_t$  is above 473 K.

EMCD measurements were performed in both Heusler layers at room temperature and at elevated temperature. The results are summarised in table 6.7. In figures 6.26 and 6.27 these values are plotted together with the simulations for the Ni and Mn EMCD signals of the two layers. It can be seen that the measurements in the Ni<sub>2</sub>MnGa layer agree quite well with the calculations, while for the Ni<sub>2</sub>MnSn layer the trend (positive signal for Mn, a negative one for Ni) is resembled but the absolute values are too low.

### 6.5.5. Ni<sub>2</sub>MnSn gradient layer

A Ni<sub>2</sub>MnSn Heusler layer with a gradient in its elemental composition was produced by the Bielefeld University in order to investigate the ability of producing such samples with a defined gradient in their elemental composition. This gradient would in turn give rise to a gradient of the phase transition temperature  $T_t$  across the sample. The sample was prepared for TEM investigation by means of a FIB system. An overview bright field image is shown in figure 6.28. The image indicates that austenitic and martensitic regions are present at room temperature at the same time. The MgO substrate is visible in the bottom part of the image, while a protective layer, used in the FIB preparation step, is seen in the top part.

To investigate the gradient in the composition a number of EDX linescans were per-

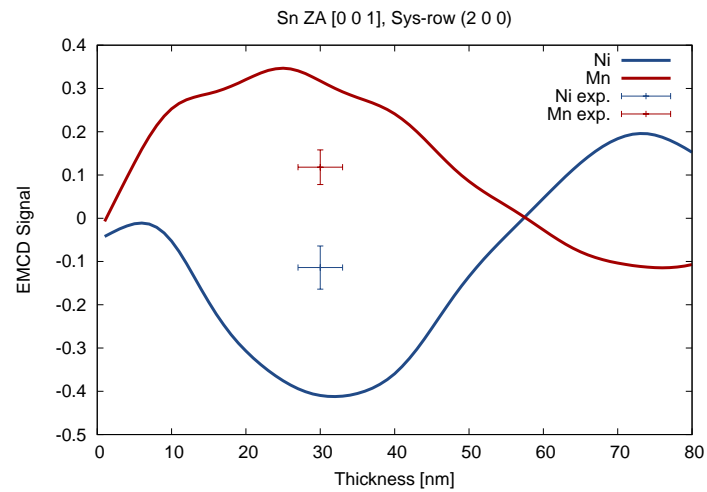


Figure 6.26.: Comparison of the experimentally determined EMCD values of the  $\text{Ni}_2\text{MnSn} - \text{Ni}_2\text{MnGa}$  double-layer with the calculated prediction of the thickness dependence of the EMCD signal in the  $\text{Ni}_2\text{MnSn}$  layer.

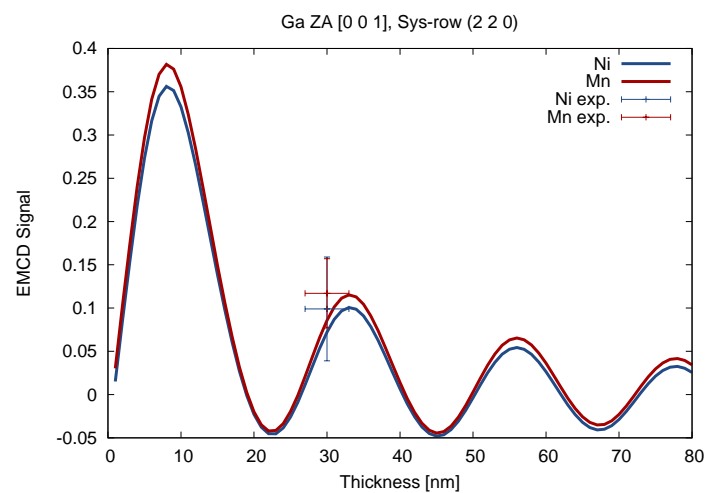


Figure 6.27.: Comparison of the experimentally determined EMCD values of the  $\text{Ni}_2\text{MnSn} - \text{Ni}_2\text{MnGa}$  double-layer with the calculated prediction of the thickness dependence of the EMCD signal in the  $\text{Ni}_2\text{MnGa}$  layer.

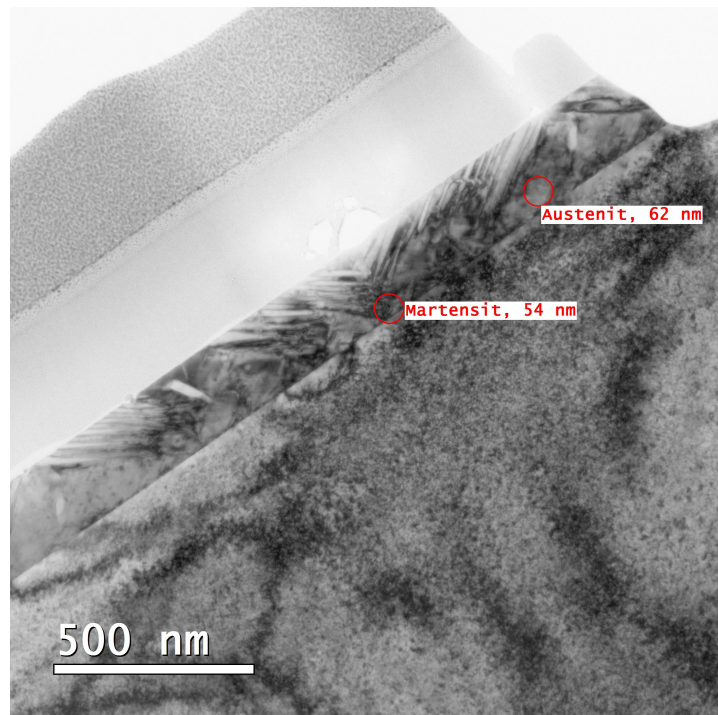


Figure 6.28.: Bright field image showing an overview of the investigated region of the Ni<sub>2</sub>MnSn gradient sample. It can be seen that the sample has martensitic and austenitic areas present at room temperature. The positions of two conducted EMCD measurements is marked in the image and the corresponding sample thickness is given.

Table 6.8.: Elemental composition of the Ni<sub>2</sub>MnSn gradient sample measured with EDX at different positions along the interface with the substrate. The measured gradients along a scan across the layer is also given.

	Ni [at%]	$\nabla[\frac{\text{at}\%}{\mu\text{m}}]$	Mn [at%]	$\nabla[\frac{\text{at}\%}{\mu\text{m}}]$	Sn [at%]	$\nabla[\frac{\text{at}\%}{\mu\text{m}}]$
1:	46.65 ± 1.47	-30.0	28.95 ± 0.93	+2.2	24.41 ± 1.33	+28.0
2:	42.80 ± 0.32	-3.0	28.84 ± 0.35	+3.7	28.36 ± 0.35	-0.8
3:	43.21 ± 0.47	-6.0	29.54 ± 0.85	+1.0	27.25 ± 0.79	+5.1

formed. All scans exhibit a negative gradient in the Ni concentration with the scanning direction from the substrate to the top of the Heusler layer. As with all the other investigated Heusler samples, the elemental composition is inhomogeneous across the layer. The elemental composition at the interface with the substrate, as it was determined using EDX, is listed in table 6.8.

EMCD measurements were conducted at different regions of the sample. In figure 6.28 the positions of two EMCD measurements, which were performed in an austenitic and a martensitic region, is marked. Figure 6.29 shows a bright field image of the sample area where the other two EMCD experiments were performed. For the EELS measurements of the EMCD experiments, the detector was subsequently placed at all four EMCD positions (see section 5.3). The two positions on each side of the systematic row reflections ( $\Delta\sigma_1$  and  $\Delta\sigma_2$ , respectively) were compared to calculate the EMCD signal. The results are given in table 6.9. From the values in the table it can be seen that the measurements on either side of the systematic row reflections result in quite different EMCD signals, although the signals should be the same. The reason for this discrepancy can be found in the not ideal excitation of the systematic row reflections. There is an asymmetry “above” and “below” the systematic row, arising from the Ewald sphere, and the fact that the Laue circle center lies on one side of the systematic row. This leads to different excitations of the reflections (different excitation errors) of the adjacent systematic rows, which in turn affects the measured EELS signal at the four EMCD positions.

### 6.5.6. Other investigated samples

Some more Heusler alloys were investigated in the TEM during the project but no EMCD measurements were performed on these samples. Nevertheless, the results of the TEM



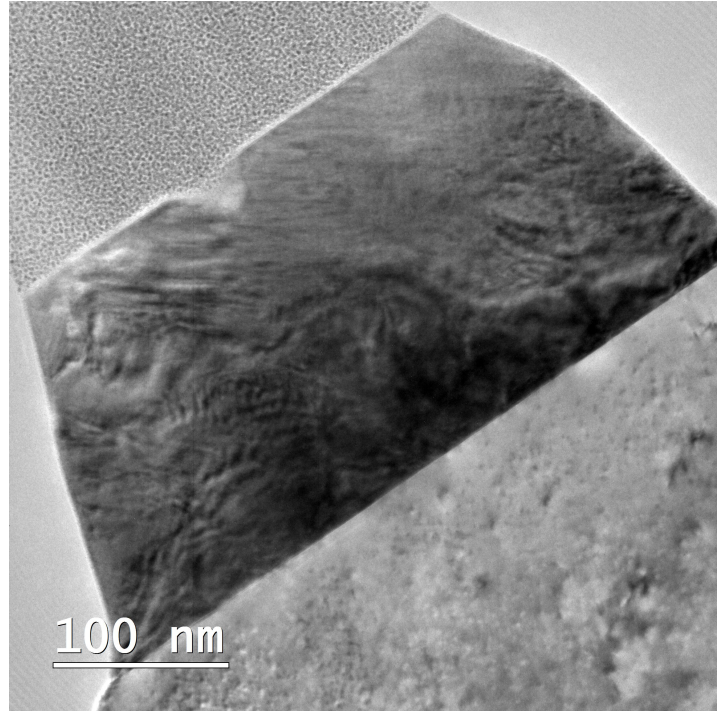


Figure 6.29.: Bright field TEM image of the  $\text{Ni}_2\text{MnSn}$  gradient sample's region where the other two EMCD experiments were performed. The sample thickness was ca. 50 nm

Table 6.9.: Measured EMCD signals on the Mn- $L_{2,3}$  edge and the Ni- $L_{2,3}$  edge of the  $\text{Ni}_2\text{MnSn}$  gradient sample. The signal measured at the EMCD positions on either side of the systematic row ( $\Delta\sigma_1$  and  $\Delta\sigma_2$  respectively, see section 5.3) are denoted respectively in the column "EMCD-Pos.". Sample position 1 and 2 denote the measurements performed in the austenitic and martensitic phase, respectively, shown in figure 6.28. Sample positions 3 and 4 were acquired at the region shown in figure 6.29.

Sample-Pos.	EMCD-Pos.	Mn: 640 eV	Ni: 855 eV	Thickness
		EMCD signal	EMCD signal	
1	$\Delta\sigma_1$	-7.8%	-20.0%	62 nm
1	$\Delta\sigma_2$	-13.9%	13.2%	62 nm
2	$\Delta\sigma_1$	-1.9%	-14.3%	54 nm
2	$\Delta\sigma_2$	-13.0%	4.9%	54 nm
3	$\Delta\sigma_1$	14.6%	-7.3%	50 nm
3	$\Delta\sigma_2$	-3.4%	10.7%	50 nm
4	$\Delta\sigma_1$	-14.3%	-20.9%	50 nm
4	$\Delta\sigma_2$	0.1%	10.8%	50 nm

Table 6.10.: Comparison of the nominal and the experimentally determined elemental composition of the sample. EDX 1 and 2 refer to the measurements at different NiCoMnAl Heusler samples.

	Ni [at%]	Co [at%]	Mn [at%]	Al [at%]
Nominal:	41.00	10.40	34.80	13.80
EDX 1:	$36.50 \pm 3.70$	$6.90 \pm 1.50$	$30.90 \pm 3.60$	$25.70 \pm 3.50$
EDX 2:	$55.44 \pm 3.68$	$9.06 \pm 2.41$	$27.85 \pm 3.44$	$7.65 \pm 3.19$

investigation of two samples is described in the following section, as it shows why these samples are not suitable for ferroic cooling applications.

In the NiCoMnAl sample no phase transition could be triggered in the investigated temperature range. Figure 6.30 shows diffraction patterns recorded at different temperatures during heating the sample. No significant change could be observed indicating that no phase transition occurred. As became clear from EDX measurements, the stoichiometry of the samples was quite different to the nominal elemental composition (table 6.10). This shifted the transition temperature to a region, which was not reached during our investigation.

The CoCrAl sample grown on GaAs showed that the GaAs substrate is not suitable to produce Heusler alloys for ferroic cooling applications. A lot of the Heusler material diffused into the substrate resulting in a large change of stoichiometry as well as an inhomogeneous elemental distribution in the Heusler layer. Figure 6.31 shows a combination of an HAADF STEM image and an EDX elemental map, from which the polycrystalline structure and the measured elemental composition of the sample can be deduced. A similar segregation into different phases as can be seen in figure 6.31 was also reported for other Heusler alloys including Cr and Co [74, 75].

## 6.6. Interpretation

### 6.6.1. Results of the investigations

In the previous sections, the results of the TEM investigations of Heusler alloys designed for the “Ferroic cooling” project were shown. EMCD was applied in the course of these investigations to gain information about the magnetic properties of the different Heusler materials, especially across the martensitic phase transition. To our knowledge, it is

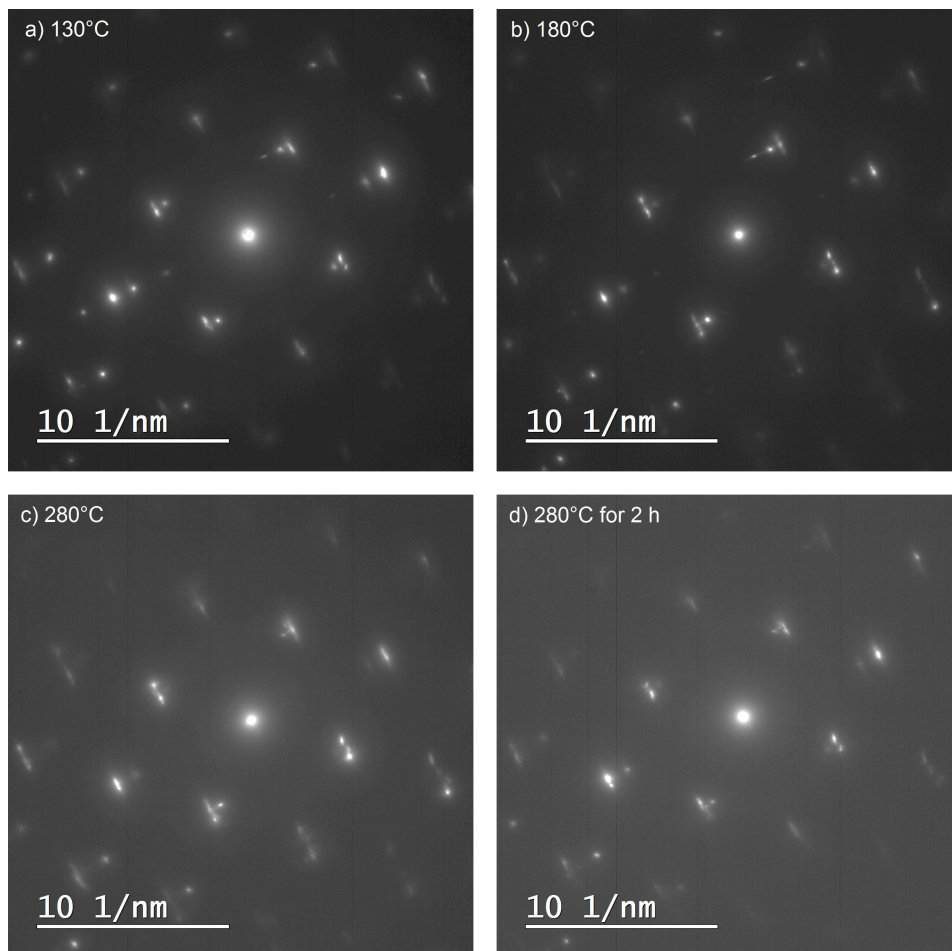


Figure 6.30.: Diffraction pattern of the NiCoMnAl Heusler-alloy at different temperatures, ranging from 130 °C to 280 °C. The patterns were acquired in-situ during heating up the sample. No significant change in the patterns is seen, indicating that no transformation into the austenitic phase takes place.

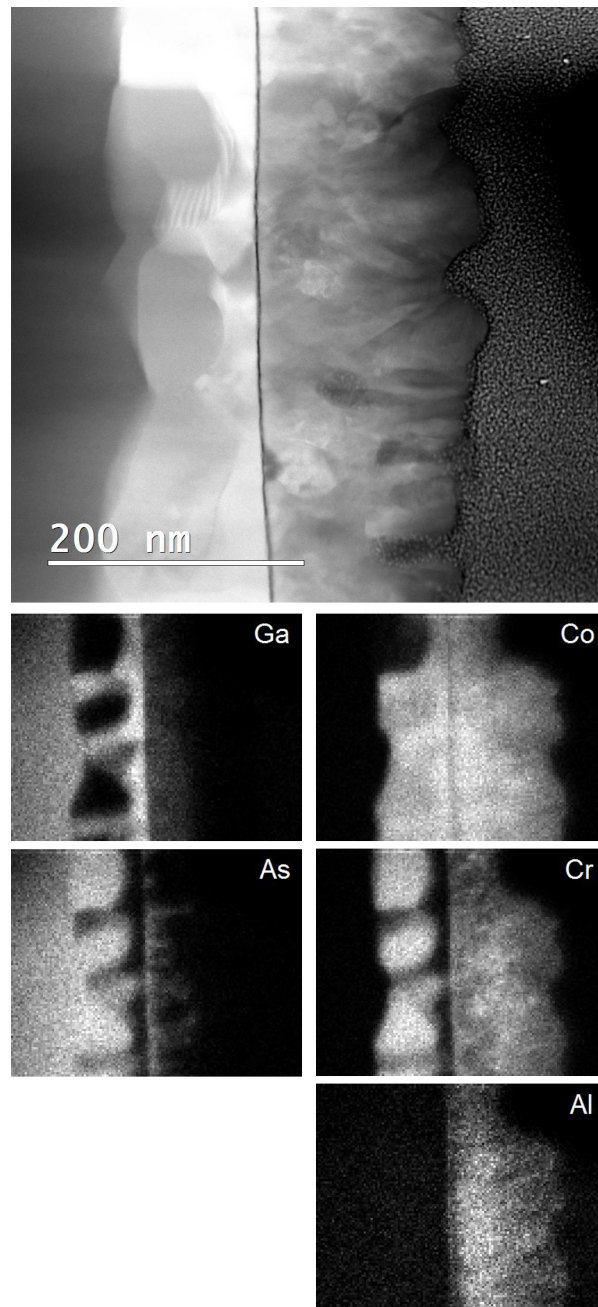


Figure 6.31.: Top: HAADF STEM image of a CoCrAl Heusler compound grown on GaAs substrate. Bottom: Elemental maps of the sample as obtained by means of EDX mapping. The diffusion of Co and Cr into the substrate can be seen clearly.

the first time that EMCD was applied as part of a thorough electron microscopical investigation for such a large number of different materials.

An important finding of the analytical TEM investigation was that the elemental composition of the Heusler alloys is quite inhomogeneous and, therefore, the properties of the materials (e.g. transition temperature) are different across the samples. When it comes to the interpretation of the EMCD results, one has to keep in mind that EMCD is a local investigation method. The spatial resolution depends on the illuminated sample region, which is the same region from which the magnetic information is retrieved. As the samples are inhomogeneous in their composition, the measured EMCD signal is in turn different for each measurement position in a sample. Furthermore, the comparability with the calculated predictions strongly depends on the elemental composition. The simulations were performed for the nominal composition of the Heusler alloys. If the composition changes, the elements are distributed statistically across the atomic positions. This can not be modelled with the simulation software used in this work. Furthermore, it would require a completely different Ansatz for the calculations.

The comparison of the experimental results with the simulations shows that if the elemental composition is similar to the nominal Heusler composition, the match is quite good, but it becomes worse if the composition of the material changes. Additionally, it can be seen that the results for the Mn EMCD signal show better agreement with the calculations than the Ni EMCD signal. This observation is related to the fact that the Ni in the investigated Heusler alloys is not fully spin-polarised. There are only a few Heusler materials exhibiting an almost full spin-polarisation. One of which is  $\text{Co}_2\text{MnSi}$  [76]. The simulations account for a fully saturated magnetisation. If this is not the case in the investigated material and if, for example, the easy axis does not correspond with the  $z$ -axis of the TEM, the absolute value of the measured EMCD effect would be smaller than for a fully saturated case.

The effect of beam damage also influences the measured EMCD spectra. In some cases the electron beam drilled a hole during the measurements, essentially making those useless. Whether the electron beam has changed the sample during the measurements can be checked easily by taking a look onto the pre-edge background of the spectra. The background changes for example when the thickness of the sample position has changed. Only those spectra whose background at the two EMCD measurement positions look the same were taken for evaluation.

### 6.6.2. Proposed workflow for EMCD experiments

Despite the difficulties mentioned in the previous section, it is possible to employ EMCD as part of a thorough electron microscopical study of magnetic materials, as long one keeps in mind a few things. Therefore, a possible workflow for EMCD studies is proposed: At first, the structure of the investigated material has to be studied in detail. This can be facilitated e.g. by a combination of bright field and high resolution imaging as well as the acquisition of diffraction patterns. Secondly, the elemental composition of the sample has to be known. Therefore EDX and EELS analyses are necessary. In case of possibly inhomogeneous compositions, this has to be done in a sufficient number of sample regions. With this information, detailed simulations of the EMCD signal in the investigated material should be done. From the results of these calculations one can find ideal settings for the EMCD experiments, such as sample orientation and sample thickness. The actual EMCD measurements have to be performed by carefully observing stability of the sample and the microscope as well as paying attention to beam induced sample damage. The thus acquired EMCD spectra can then be compared with the performed simulations in order to interpret the results.

# 7. EMCD investigation of magnetite

## 7.1. The Verwey transition in magnetite

Magnetite is of interest in physics as well as in chemistry, for example because of its surface chemistry [77, 78]. To design the catalytic function of metal nanoparticles, a suitable support material has to be chosen. There is a number of supports that interact with the metal particles by the so-called strong metal support interaction (SMSI). As the full understanding of the SMSI is still missing, these materials are under investigation, for example using aberration corrected transmission electron microscopy. To that end, the interface of magnetite and Pt-nanoparticles were studied [78].

Not only the chemical properties of magnetite are interesting, also the investigation of the magnetic properties is worthwhile. The material exhibits a Verwey transition, named after E.J.W. Verwey, at 125 K [79]. Magnetite exhibits a drop in its magnetisation if cooled down below the transition temperature. Alongside the magnetism, also the electronic properties and the structure changes. The mechanism of the transformation is still under discussion. The question remains, whether the electronic transition is driven by the structural change or vice versa [80]. At the transition temperature the cubic phase changes to a monoclinic phase inducing a twinned structure in the material. The first real space images of the magnetite surface in the transformed state were recorded using scanning tunneling microscopy and are reported in [80]. Furthermore, the change of the magnetic domains during cooling and heating across the Verwey transition and their interaction with crystallographic twins were investigated using Lorentz transmission electron microscopy [81].

In the following section, an in-situ TEM investigation of magnetite is reported in which the change of the magnetic properties were investigated on the nanoscale using EMCD.

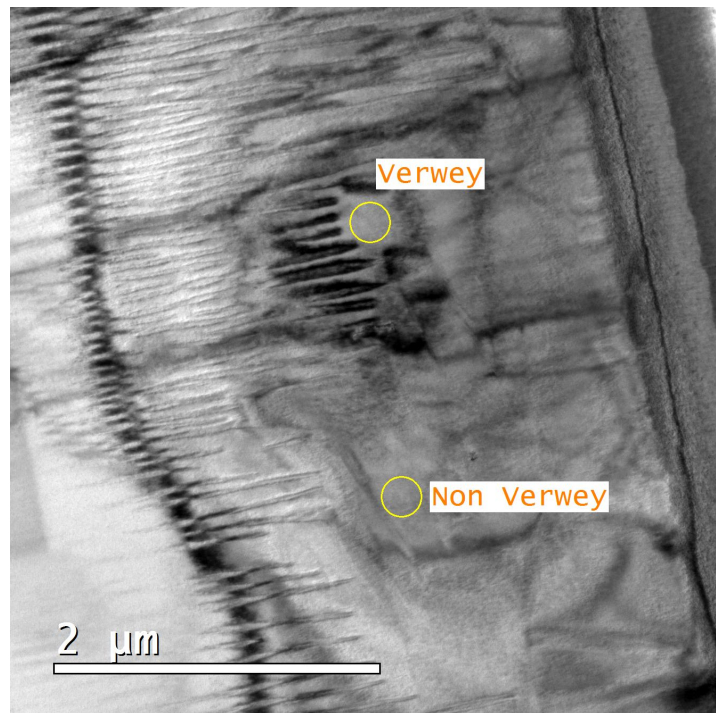


Figure 7.1.: Bright field overview image of the magnetite sample. The streaks in the left hand area mark the transformed regions. Two investigated areas are marked with circles and it is noted whether the region was already transformed or not. This was checked using diffraction patterns.

## 7.2. In-situ EMCD investigation

A magnetite sample was prepared for TEM investigation by means of a FIB system and subsequent thinning using an ion milling system “Gentlemill” (see also section 6.5.1). A cooling holder was used to examine the sample at room temperature and at a temperature below 125 K, at which the Verwey transition takes place. In figure 7.1 a bright field overview image of the sample at a temperature of 89 K is shown. On the left hand side of the image a number of streaks can be seen, indicating the transformed regions. According to [80] these regions exhibit a twinned structure, induced by the structural changes of the Verwey transition. In the image, two areas are marked with circles, representing the position of the acquired EMCD spectra. In both regions diffraction patterns were acquired, showing that one of them already transformed, while the other one is still in the state before the Verwey transition. The diffraction patterns are shown in figure 7.2. The fact that not the whole sample exhibits the transformed state indicates that there are



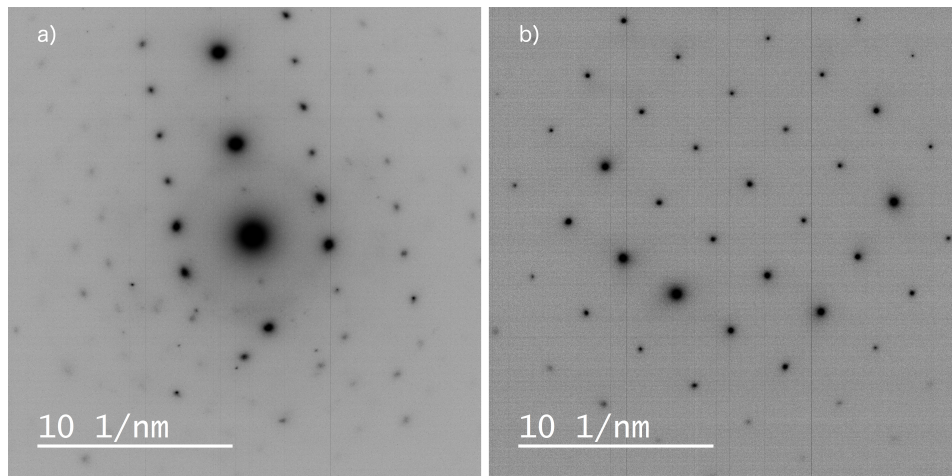


Figure 7.2.: a) Diffraction pattern acquired in  $[100]$  zone axis of the sample region marked with “Verwey” in figure 7.1. b) Diffraction pattern acquired in  $[100]$  zone axis at the region marked with “Non-Verwey” in figure 7.1, exhibiting the diffraction pattern of cubic  $\text{Fe}_3\text{O}_4$ .

variations from the perfect magnetite stoichiometry  $\text{Fe}_3\text{O}_4$  across the sample [79, 80].

The corresponding EMCD measurements of the two regions are shown in figures 7.3 and 7.4. In both cases, the raw spectral data of both measurement positions were compared. The spectra were aligned at the energy of the Fe  $L_3$ -edge in order to compensate for small energy drifts in the spectrometer. It can be seen that the pre-edge as well as the post-edge background fit almost perfectly. In figure 7.4 an EMCD effect is clearly visible, while in figure 7.3 the effect has vanished. These measurements were repeated at different sample positions as well as after additional heating and cooling cycles of the sample, triggering the Verwey transitions. In all measurements, the same result was found indicating vanishing magnetic moments below the Verwey transition temperature. The calculation of the ratio of the orbital and spin magnetic moments  $m_l/m_s$  from the acquired EMCD spectra is described in section 5.5.

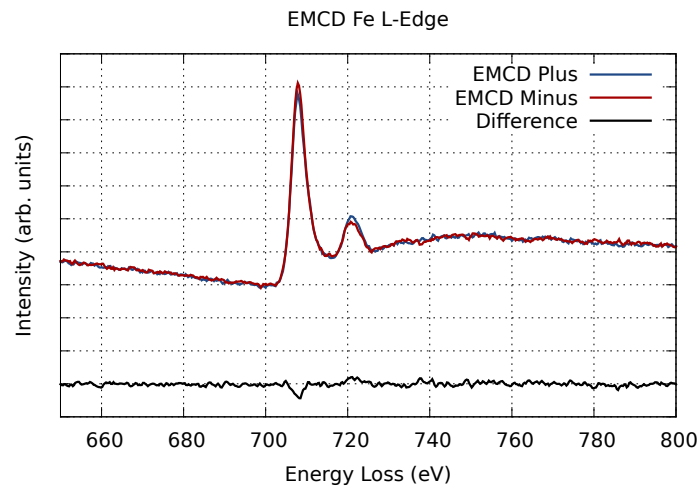


Figure 7.3.: EMCD spectra acquired in the non transformed sample region. The sample was tilted out of the  $[100]$  zone axis into a systematic row condition including the  $(022)$  reflection. The raw spectra were aligned at the the Fe  $L_3$ -edge and compared. The difference spectrum, exhibiting the EMCD effect, is also shown.

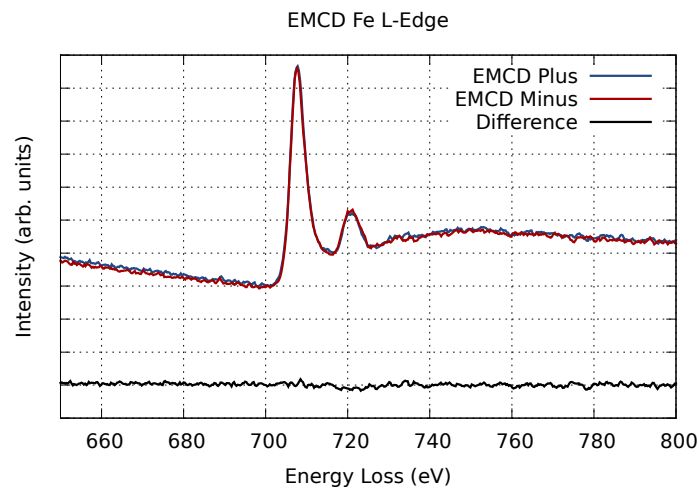


Figure 7.4.: EMCD spectra acquired in the transformed sample region. The sample was tilted out of the  $[100]$  zone axis into a systematic row condition including the  $(022)$  reflection. The raw spectra were aligned at the Fe  $L_3$ -edge and compared. No EMCD effect was visible, indicating vanishing magnetic moments below the Verwey transition temperature of 125 K.

# 8. ELCE investigation of rutile

## 8.1. The crystal structure of rutile

Parts of the following sections are based on [17]. Rutile ( $\text{TiO}_2$ ) was investigated because due to the symmetry of the orbitals caused by its tetragonal unit cell, it is suitable to examine the site-specificity of the ionisation edge fine-structure using channelling effects. In figure 8.1, a schematic of the rutile unit cell is shown. The arrows depict each atom's local coordinate system as it is used in the DFT simulation software package WIEN2k. The crystallographic structure's space group gives rise to the fact that the local coordinate systems of some of the oxygen atoms are rotated by  $90^\circ$  with respect to those of the other oxygen atoms. A detailed description of the bonding situation in rutile as well as a visualisation using electron density plots is given in [82], where it is shown that the metal atoms in the structure are octahedrally coordinated by anions. Therefore, the titanium atoms show an  $e_g$ - $t_{2g}$  splitting. Although the octahedra are slightly distorted, it is still justified to use the “ $e_g$ ” and “ $t_{2g}$ ” classification rather than that of a lower symmetry. The difference in the distance of the top/bottom vertices and the basal vertices from the centre is about 1.7% [82]. Due to the hybridisation between Ti and O orbitals, the splitting can also be seen in the oxygen projected partial density of states (pDOS), which is plotted in figure 8.2. This gives rise to the assumption that by using distinct channelling conditions, the influence of different orbitals on the measured energy-loss spectra can be varied.

## 8.2. Simulations

The oxygen pDOS was calculated using the density functional theory (DFT) simulation package WIEN2k [12]. The parameters of the unit cell for the calculation can be found in table 4.1.

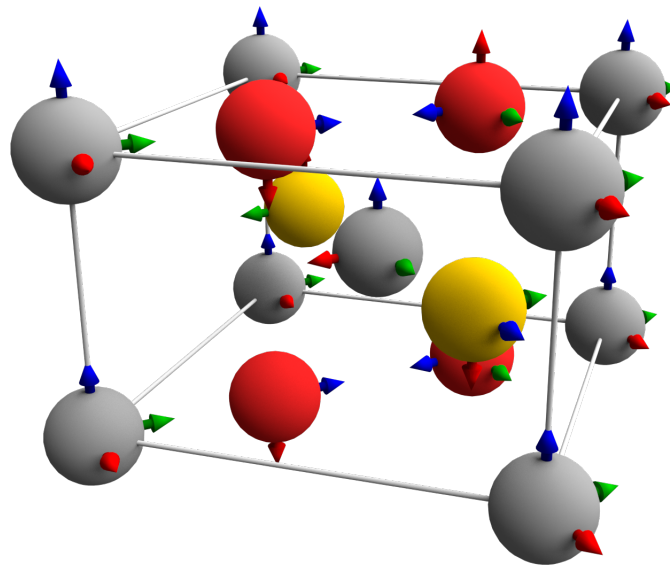


Figure 8.1.: Schematic of the rutile unit cell. Titanium atoms are plotted in grey while oxygen atoms are plotted in red and yellow. The arrows depict each atom's local coordinate system due to the structure's symmetry (red:  $x$ -axis, green:  $y$ -axis, blue:  $z$ -axis).

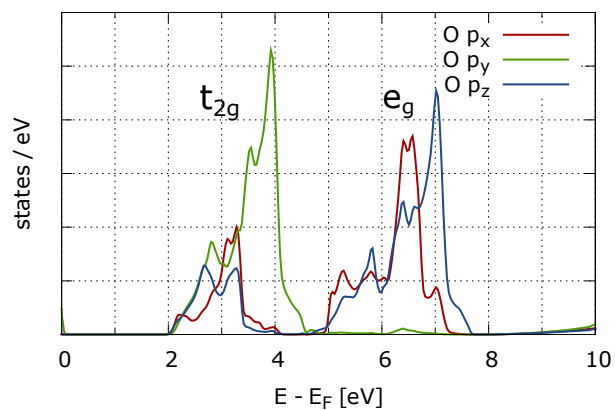


Figure 8.2.: Oxygen projected density of states of rutile above the Fermi-energy. The calculation was performed using WIEN2k.

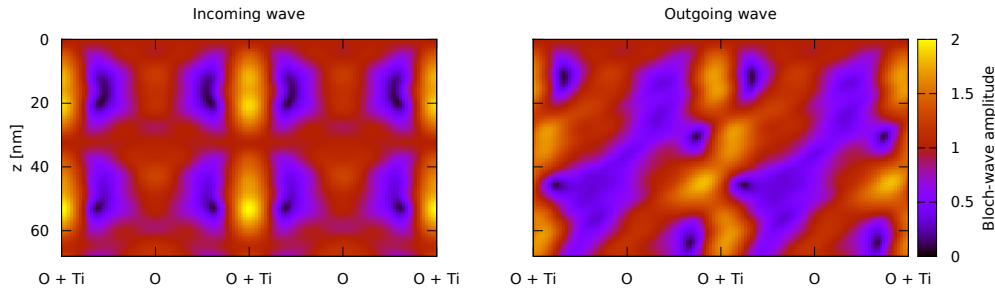


Figure 8.3.: Calculation of the Bloch wave amplitudes in a 70 nm thick rutile crystal. The simulations were performed for a specimen that was tilted out of the  $[1\ 1\ 0]$  zone axis in order to obtain a systematic row condition including the  $G = (1\ \bar{1}\ 0)$  diffraction spot. The vertical axes correspond to the  $(4\bar{4}0)$  planes. Left: Incoming electron wave. Right: Outgoing electron wave. The detector is at a position displaced from the origin of the diffraction pattern in the direction of  $G$ , at a position  $1/3$  of the distance to this reflection.

For the calculation, 1000 k-points were used and the value for  $R_{\text{MT}}K_{\text{max}}$  was set to 7. The muffin tin radii  $R_{\text{MT}}$  for the oxygen and titanium atoms were chosen to be 1.72 a.u. and 1.94 a.u., respectively. Due to calculational details (using DFT, the calculation of L-edges is not as reliable as calculating K-edges [83]), in the following work we keep the focus on the oxygen K-edge, see [84] and [83].

A combination of two simulation software packages was applied to calculate the effects of different channelling conditions on the measured oxygen K-edge electron energy-loss spectra. The first program package uses the Bloch wave formalism for treating elastic scattering [11], while it uses the mixed dynamic form factor (MDFF) [6] to describe inelastic scattering events. The DDSCS used in the Bloch wave program is calculated as given in equation (3.36). For more details on this formula see section 3.2.3 and for example [5, 16, 42].

Using the program, the distribution of the Bloch waves inside a crystal can be calculated. In figure 8.3 (left), the Bloch wave distribution of the incoming electron wave in 70 nm thick rutile in  $[1\ 1\ 0]$  projection is plotted. In figure 8.3 (right), the Bloch wave distribution of the outgoing electron wave that reaches the EELS detector is plotted for the same crystal specifications. The details of the experimental setup were chosen such that, starting from the  $[1\ 1\ 0]$  zone axis, a systematic row condition including the  $(1\ \bar{1}\ 0)$

diffraction spot was established by tilting the specimen. A combination of 5 incoming and 4 outgoing Bloch waves was used.

One can easily see that for the two electron waves the amplitude distribution inside the crystal shows distinct changes. As the interaction of the beam electrons with the sample happens mainly at the regions in the crystal where the amplitudes have their maxima, interpretation of the measured spectra is not straightforward any more. Therefore, detailed simulations are necessary for measurement interpretation. In order to simulate the effects on the energy-loss spectra caused by these changes of the amplitude distribution, the MDFF, as given in equation (3.46), has to be calculated.

In order to investigate the changes in the ionisation edge fine-structure, WIEN2k was used to describe the target states occurring in the MDFF. The MDFF needed in the first simulation package was calculated based on the XDOS and the wave functions of the target electron by TELNES.3 subroutines implemented in WIEN2k, see [9, 27, 41].

For the simulations on rutile shown in this work, the crystallographic data as given in Table 4.1 was used in the input file for the Bloch wave program. For the simulation of the oxygen K-edge energy-loss spectra in the desired energy range of 525 eV to 539 eV, the wave functions of the target electrons and the cross-density of states at a certain energy-loss value have to be extracted from a previous WIEN2k calculation. Then, the DDSCS for this energy-loss value is calculated using the Bloch wave program. Finally, these steps were repeated until the desired energy-loss range was covered.

When changing the channelling conditions, the amplitudes of the Bloch waves inside the crystal are altered (see also section 4.1). This in turn changes how much different columns of oxygen atoms are probed when investigating the oxygen K-edge ELNES. A sketch of the scattering conditions is shown in figure 8.4. For dipole allowed transitions in the scattering process, those states that lie parallel to the momentum transfer vector  $\mathbf{q}$  (in figure 8.4 the vectors  $\mathbf{q}$  and  $\mathbf{q}'$ ) are probed predominantly, as can be seen from the inner product of the momentum transfer vector and the position vector in the exponential function in  $\langle f | e^{i\mathbf{q}\cdot\mathbf{R}} | i \rangle$ , which is part of equation (3.29). Thus, by changing either the channelling conditions or the direction of the momentum transfer vectors, different states can be probed. In our case, changing the channelling conditions, such that adjacent columns of oxygen atoms would be probed differently (conditions “A” and “B” in figure 8.5) and keeping the momentum transfer vectors, would result in probing predominantly the states that lie in the same direction but in different columns. (e.g. as depicted in figure 8.5 the “blue” states in the yellow column and the “green” states in

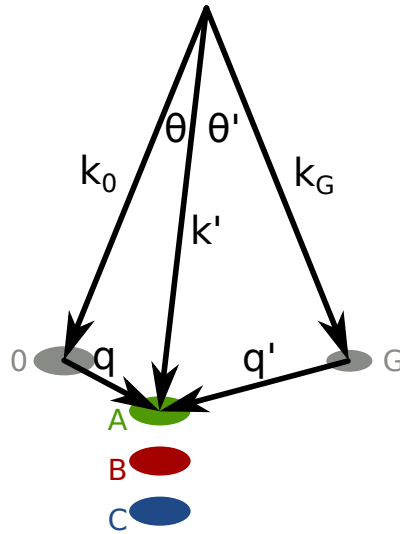


Figure 8.4.: Sketch of the scattering geometry.  $k_0$ ,  $k_G$  and  $k'$  are momentum vectors, while  $q$  and  $q'$  are momentum transfer vectors.  $\theta$  and  $\theta'$  are the corresponding scattering angles.  $0$  and  $G$  denote Bragg reflections, while “A”, “B” and “C” depict the detector positions as they were used in the experiments.

the red column). While keeping the channelling conditions the same but changing the direction of the momentum transfer vector would result in probing different states in the same column. Usually, a combination of both effects is observed in the experimental measurements. This is because in the actual experiment we change the position of the spectrometer entrance aperture with respect to the diffraction pattern by shifting the pattern. This shift changes the direction of the outgoing electron wave and therefore changes the channelling conditions. At the same time, the direction of the momentum transfer vector is changed, as it always “points” from the diffraction spots to the position of the SEA.

To elucidate the measured effects, a short “back of the envelope” calculation is done. As a starting point, the MDFFF as shown in equation (3.29) is taken. The transition matrix elements in dipole approximation [85] read

$$r_{lm} = \sum_{i,f} \langle i|r_l|f\rangle \langle f|r_m|i\rangle \delta(E_{|f\rangle} - E_{|i\rangle} - E), \quad (8.1)$$

with the transition matrix

$$\hat{R} = \{r_{lm}\}. \quad (8.2)$$

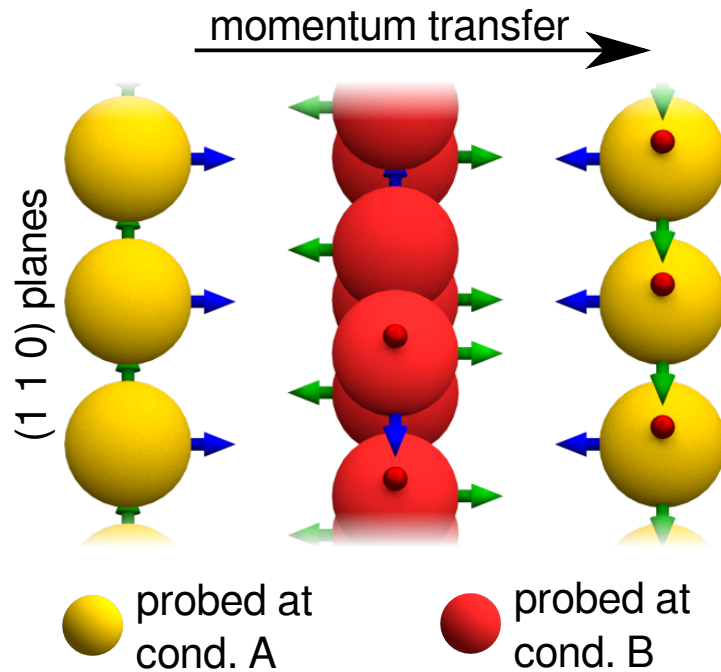


Figure 8.5.: Sketch of the (110) planes in the rutile crystal and the local coordinate systems of the oxygen atoms (x-axis – red, y-axis – green and z-axis – blue arrows). These coordinate systems correspond to the directions in which the  $p_x$ ,  $p_y$  and  $p_z$  states lie. By using different channelling conditions, different oxygen columns (red or yellow, respectively) are probed predominantly. In each case, the states parallel to the momentum transfer vector (in figure 8.4 the vectors  $\mathbf{q}$  and  $\mathbf{q}'$ ) give the dominant contribution. For the direction in the actual experiment see figure 8.4.



Thus, the MDFF can be written as

$$S(\mathbf{Q}, \mathbf{Q}', E) = \mathbf{Q} \hat{R} \mathbf{Q}'. \quad (8.3)$$

One can find an orientation of the rutile crystal in which the transition matrix becomes diagonal with the diagonal elements  $p_x^2$ ,  $p_y^2$  and  $p_z^2$  [23]. The MDFF for scattering events in one of the oxygen columns shown in figure 8.5 reads:

$$S_1(\mathbf{Q}, \mathbf{Q}', E) = \mathbf{Q} \begin{pmatrix} p_y^2 & 0 & 0 \\ 0 & p_z^2 & 0 \\ 0 & 0 & p_x^2 \end{pmatrix} \mathbf{Q}', \quad (8.4)$$

while the MDFF for the other oxygen column is given by

$$S_2(\mathbf{Q}, \mathbf{Q}', E) = \mathbf{Q} \begin{pmatrix} p_z^2 & 0 & 0 \\ 0 & p_y^2 & 0 \\ 0 & 0 & p_x^2 \end{pmatrix} \mathbf{Q}'. \quad (8.5)$$

The choice of  $p_x^2$ ,  $p_y^2$  and  $p_z^2$  was made corresponding to the coordinate system shown in figure 8.5. For the scattering conditions depicted in figure 8.4, the EELS detector was placed at  $1/3$  of the distance  $\mathbf{g}$  between the  $\mathbf{0}$  and  $\mathbf{G}$  reflections. For the three measurements, it was additionally shifted  $0.1g$ ,  $0.2g$  and  $0.3g$  away from the systematic row (conditions “A”, “B” and “C”). Thus, one gets for the MDFF in the different atomic columns:

$$S_1(\mathbf{Q}, \mathbf{Q}', E) = -\frac{2}{9}g^2 \cdot p_y^2 + c^2 g^2 \cdot p_z^2 + q_E^2 \cdot p_x^2 \quad (8.6)$$

and

$$S_2(\mathbf{Q}, \mathbf{Q}', E) = -\frac{2}{9}g^3 \cdot p_z^2 + c^2 g^2 \cdot p_y^2 + q_E^2 \cdot p_x^2, \quad (8.7)$$

with  $c^2$  a number changing with the different detector positions, in the given example  $c^2 = \{0.01, 0.04, 0.09\}$ . The factor  $-2/9$  arises from the fact that  $q_x = 1/3$  and  $q'_x = -2/3$ , while  $q_E$  is the characteristic momentum transfer for the oxygen K-edge in this example.

In order to model the effects of different channelling conditions, the MDFFs of the two oxygen columns have to be summed with prefactors taking different excitations due to channelling into account. For example, a hypothetical channelling condition in

which only the column labelled with subscript 1 is probed (thus  $S_2(\mathbf{Q}, \mathbf{Q}', E)$  does not contribute), would lead to the following MDFFs:

$$S_1(\mathbf{Q}, \mathbf{Q}', E) = g^2 \cdot \begin{cases} -2/9p_y^2 + 0.01p_z^2 + 0.16p_x^2 & \text{for detector position A} \\ -2/9p_y^2 + 0.04p_z^2 + 0.16p_x^2 & \text{for detector position B} \\ -2/9p_y^2 + 0.09p_z^2 + 0.16p_x^2 & \text{for detector position C.} \end{cases} \quad (8.8)$$

The prefactor 0.16 arises from the fact that  $g = g_{(1\bar{1}0)} \approx 9.7 \text{ nm}^{-1}$ , thus  $q_E \approx 4.34 \text{ nm}^{-1} \approx 0.4 \cdot g$ . Note that the negative contribution of  $p_y$  states in this example should not cause any concern, as only the interference terms are described by equation (8.8).

Comparing the above results with figure 8.2, it becomes clear that the measured energy-loss spectra would exhibit an increasing contribution of  $p_z$ -states when changing from detector position A to position C. For different channelling conditions, one needs to take into account the contribution of  $S_2(\mathbf{Q}, \mathbf{Q}', E)$  as well. However, the basic underlying principle remains the same.

### 8.3. Experimental setup

The rutile sample was prepared in  $[1\ 1\ 0]$  zone axis using a focused ion beam (FIB) and subsequently thinned using a GATAN PIPS ion mill. The experiments were conducted using a FEI TECNAI G2 TF20 operated at 200 kV and a FEI TITAN operated at 300 kV. Both instruments have a Gatan GIF Tridiem attached.

The specimen was tilted out of the  $[1\ 1\ 0]$  zone axis in order to obtain a systematic row condition including the  $(1\bar{1}0)$  diffraction spot. Different channelling conditions were established by shifting the diffraction pattern such that the position of the SEA was changed with respect to the diffraction spots. Due to the Lorentzian behaviour of the DDSCS, the intensity of the acquired energy-loss spectra decreases very fast when moving the SEA away from the diffraction spots [86]. By increasing the convergence angle, sufficient intensity was gained. As a consequence, the diffraction spots were spread so that the convergence semi-angle was approximately equal to the collection semi-angle (in our experiments about 1 mrad). Under these conditions, the experimental spectra are still comparable to the simulated ones, for which an incoming plane wave was assumed. A more convergent beam would require a different calculation (e.g. multislice simulations).

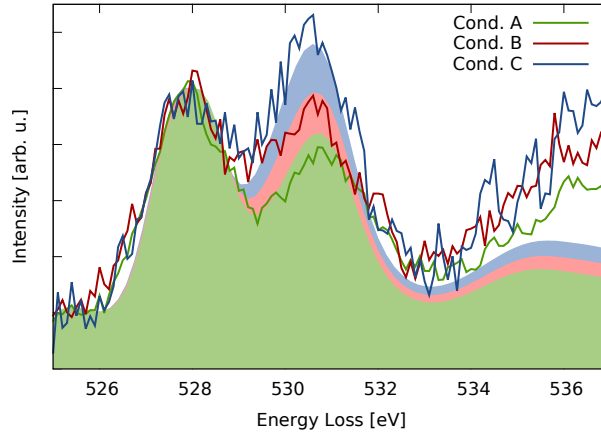


Figure 8.6.: Simulated electron energy-loss spectra calculated using the experimental parameters described in the previous section depicted as filled areas. The experimental spectra are plotted in the corresponding colour on top of the simulated ones. The spectra are all normalised to the maximum of the first peak for easier comparison.

A sketch of the scattering geometry is shown in figure 8.4. Three different measurement positions are marked “A” to “C”. The SEA was placed a third of the distance between the 0 and the G reflection away from the 0 reflection ( $0.3\overline{0G}$ ) and shifted  $0.1\overline{0G}$ ,  $0.2\overline{0G}$  and  $0.3\overline{0G}$  perpendicular to the systematic row for measurement positions “A”, “B” and “C”, respectively.

The energy-loss spectra were acquired using a 2.0 mm SEA, a dispersion of 0.2 eV per pixel and an acquisition time of 30 s. The spectral resolution was determined to be 1.0 eV by measuring the full width at half maximum of the zero loss peak. The specimen thickness of  $\sim 70$  nm was determined using low loss EELS and the Log-ratio method [3].

## 8.4. Results

Figure 8.6 shows, as filled areas, the calculated spectra as they arise from the three measurement positions depicted in figure 8.4. In order to facilitate comparison of the three spectra, they are normalised to the maximum of the first peak, which is necessary as the total intensities for the different detector positions are different. It can be seen that by changing the scattering conditions, the relative heights of the peaks at energy-losses of about 528 eV (corresponding to  $E_F + 4$  eV in figure 8.2) and about 531 eV

(corresponding to  $E_F + 7$  eV in figure 8.2) can be inverted. As mentioned above, this is due to the change of the direction of the momentum transfer vector  $\mathbf{q}$  and the subsequent change of the influence of the probed orbitals. At position “A”, the  $p_y$  orbitals are probed predominantly while at position “C”, the influence of the  $p_x$  and  $p_z$  orbitals is increased. At scattering condition “B”, both orbitals contribute such that the fine-structure exhibits two equally high peaks.

The experimentally acquired spectra are plotted on top of the simulations. The measured spectra are also normalised to the maxima of the first peaks. The inversion of the peak height by using scattering conditions “A” and “C” can be seen clearly. The calculated spectra match the changes in the peak heights as well as the relative intensities of the peaks around 528 eV and around 531 eV of the experimental spectra very well.

Thus, ELCE can be used to investigate and interpret the site-specific ionisation edge fine-structure in terms of orbitals and their influence on the energy-loss spectra at different scattering conditions. It therefore illustrates new possibilities for chemical and structural analyses in the TEM using interferometric EELS.

Part IV.  
Summary

# 9. Conclusion and Outlook

## 9.1. Summary

In the TEM, coherence effects can be observed every time phase contrast imaging is used, for example when acquiring high resolution TEM images. Such interferometry in the TEM does not have to be implemented in a sophisticated experimental setup, it rather “happens” automatically when investigating a crystalline sample. Going beyond elastic scattering effects, coherence in inelastic scattering processes have been studied for more than 30 years. Those investigations subsequently led to the conception of interferometric EELS. The techniques EMCD and ELCE can be seen as special cases of interferometric EELS, which are best described using the concept of the MDFF. In order to simulate and interpret the results of these two techniques, a unified theory including the combination of electronic structure calculations and elastic scattering calculations has to be used.

In this work, EMCD was applied in the context of a thorough TEM investigation of Heusler alloys produced for “ferroic cooling” applications. As EMCD is a local analytical technique, it gives information about the sample’s magnetic properties on a nm scale. At the same time, the results are therefore strongly dependent on the local elemental composition of the sample. It has been shown that many of the investigated Heusler alloys are very inhomogeneous in their composition, with a stoichiometry different from the standard full Heusler alloy. Therefore, the simulations of the EMCD measurement and the actual experimental spectra show a discrepancy for these materials. For those materials, on the other hand, that are similar to the standard Heusler alloys, the prediction of the simulations and the experimental spectra fit quite well.

Multislice simulations were performed to investigate the influence of beam convergence on the measured EMCD spectra. In the actual experiments, the beam is slightly converged in order to enhance the signal-to-noise ratio and thus reduce the acquisition time, which is crucial for beam sensitive materials. Furthermore, a converged beam also

enhances the spatial resolution of the EMCD measurements. It was shown that for convergence angles up to 2.0 mrad one can achieve sufficient EMCD signal intensity at the “standard” EMCD positions on the Thales-circle. Only for higher convergence angles alternative measurement positions have to be used.

Concerning the calculation of the ratio  $m_l/m_s$  of the spin and orbital magnetic moment, it was discussed that multiple scattering effects influence the retrieved values. For samples thicker than 10 nm, plural scattering causes erroneous values for  $m_l/m_s$ . An EMCD measurement of the Mn  $L_{2,3}$ -edge of an  $\text{Ni}_2\text{MnIn}$  Heusler was used exemplarily to calculate  $m_l/m_s$  and investigate the effect of sample thickness. However, even when accounting for plural scattering due to the sample thickness of about 50 nm, the calculated value was far too high. The reason for this is the fact that the EMCD effect at the  $L_2$ -edge is in many cases not visible or has the same sign as the EMCD effect at the  $L_3$ -edge. The cause for this behaviour is still under discussion. One aspect contributing to this are artefacts from plasmon scattering, as described above. Calculating the ratio  $m_l/m_s$  for magnetite on the contrary gives results in agreement with simulations and XMCD measurements. For this material an EMCD effect with opposite sign is visible at both, the  $L_2$  and  $L_3$  edge.

EMCD measurements were also used to investigate the Verwey transition in magnetite. According to the expected behaviour, the EMCD measurements show vanishing magnetic moments after cooling down below the Verwey transition temperature.

ELCE was used to site-specifically investigate the change of the fine-structure when free states of different character ( $p_x$ ,  $p_y$  and  $p_z$  in the example discussed) are probed. It was shown that the experimental spectra and a combined Bloch wave and DFT simulation exhibit excellent agreement. Thus, the technique is an ideal means to site-specifically investigate the chemical environment (in the sense of probing particular final states) of materials.

Concluding, one can say that the description of EMCD and ELCE under a unified theory, combining the simulation of dynamical diffraction effects and electronic structure calculations, is necessary for an accurate interpretation of experimental spectra. Using the currently implemented software, this works fine for stoichiometric samples and the experimental spectra show very good agreement with the calculations.

## 9.2. Future experiments and theoretical approaches

Concerning EMCD, the trend is the same as the general one in electron microscopy: higher spatial resolution using TEMs and STEMs with sophisticated aberration correction systems are of interest. As has been shown in the multislice simulations, when using a highly converged beam (as it is present in atomic resolution STEM investigations) the standard EMCD positions cannot be used any more. A measurement position further away from the systematic row has to be used. Alternatively, one could change the phase of the electron beam using an aberration correction system for the condenser lenses. Other possibilities to achieve atomic resolution for EMCD would need the generation of Vortex beams or the investigating variation in the energy filtered diffraction pattern. Studying surfaces and interfaces using EMCD would be worthwhile to gain information about the change of magnetic properties at the surface/interface compared to the bulk material.

ELCE can be used in future experiments to investigate the bonding situation in materials that are used for catalysis. Thus, information about the catalytic active sites could be retrieved, which in turn would enhance the understanding of the catalytic processes. As ELCE makes use of the sample's periodic structure, there would be no need for highly focused probes. Thus, such investigations would circumvent the problems of beam damage or contamination of the sample as they frequently occur when performing atomic resolved STEM.

Concerning the simulations two tasks can be coped with in future works. On the one hand, the used DFT simulations are not sufficient for calculating states of highly correlated electron systems and, for example, the L-edges of transition metal oxides. These L-edges are of interest in EMCD measurements. Thus, a method beyond DFT e.g. using the Bethe-Salpeter-Equation (BSE) could improve the situation. On the other hand it was shown that the calculations for stoichiometric systems do not fit to measurements in off-stoichiometric materials. Therefore, different means to calculate such systems with a statistical distribution of the elements inside the unit cell would be desirable. The question remains, to what extent such systems would still fulfil the necessary periodicity in order to use a Bloch wave Ansatz and channelling experiments. As an alternative, simulation programs that do not need a periodic structure (for example FEFF or ORCA) could be implemented.



# List of Abbreviations

ALCHEMI	— Atom Location by Channelling Enhanced Microanalysis
CBED	— Convergent Beam Electron Diffraction
CCD	— Charge-Coupled Device
DDSCS	— Double Differential Scattering Cross-Section
DFE	— Dynamic Form Factor
DFT	— Density Functional Theory
DOS	— Density of States
EDX	— Energy Dispersive X-ray
EELS	— Electron Energy-Loss Spectrometry
ELCE	— Energy Losses by Channelled Electrons
ELNES	— Energy-Loss Near Edge Structure
EMCD	— Energy-Loss Magnetic Chiral Dichroism
FEG	— Field Emission Gun
LACDIF	— Large Angle Convergent Diffraction
LCC	— Laue Circle Centre
MDFE	— Mixed Dynamic Form Factor
pDOS	— Partial Density of States
SAA	— Selected Area Aperture

SEA	— Spectrometer Entrance Aperture
STEM	— Scanning Transmission Electron Microscope
S/N	— Signal-to-noise
TEM	— Transmission Electron Microscope
USTEM	— University Service Centre for Transmission Electron Microscopy
XANES	— X-ray Absorption Near Edge Structure
XAS	— X-ray Absorption Spectroscopy
XDOS	— Cross Density of States
XMCD	— X-ray Magnetic Circular Dichroism

# List of Figures

1.1. Schematic of a transmission electron microscope. . . . .	5
2.1. Sketch illustrating the exact Bragg condition in which the Ewald sphere intersects a reciprocal lattice point. . . . .	11
2.2. Description of the excitation error and the origin of the “relrods”. . . . .	12
2.3. Sketch of the dispersion surface and its construction. . . . .	17
2.4. The thickness dependence of the transmitted and reflected beam in a two-beam case. . . . .	19
3.1. Realisation of a Mach-Zehnder interferometer using a crystalline sample.	26
4.1. Comparison of the Bloch wave amplitudes, as given in equation (2.15), in NiO and rutile. . . . .	33
4.2. Map of Bloch wave amplitudes in rutile. The Laue circle centre position is at $(00\bar{2}0)$ . . . . .	34
4.3. Map of Bloch wave amplitudes in rutile. The Laue circle centre is tilted along the systematic row direction a fourth of the distance between $\mathbf{0}$ and $\mathbf{G}$ reflection. . . . .	34
4.4. Map of Bloch wave amplitudes in rutile. The Laue circle centre is tilted along the systematic row direction half of the distance between $\mathbf{0}$ and $\mathbf{G}$ reflection. . . . .	35
4.5. Map of Bloch wave amplitudes in rutile. The Laue circle centre is tilted along the systematic row direction 3/4 of the distance between $\mathbf{0}$ and $\mathbf{G}$ reflection. . . . .	36
4.6. Map of Bloch wave amplitudes in rutile. . . . .	37
4.7. Calculated intensities of inelastic scattering in rutile. The Laue circle centre was placed at $(00\bar{2}0)$ . . . . .	38

---

4.8.	Calculated instensities of inelastic scattering in rutile. The detector was placed at a point $1/2$ of the distance between $\mathbf{0}$ and $\mathbf{G}$ reflection. . . . .	38
4.9.	Calculated instensities of inelastic scattering in rutile. The detector was placed at a point $0.6$ of the distance between $\mathbf{0}$ and $\mathbf{G}$ reflection. . . . .	39
4.10.	Calculated instensities of inelastic scattering in rutile. The detector was placed at a point $3/4$ of the distance between $\mathbf{0}$ and $\mathbf{G}$ reflection. . . . .	39
5.1.	Equivalency of a circular polarised electric field caused by photons and electrons. . . . .	43
5.2.	Sketch of the setup for an EMCD experiment using a two-beam case. . .	45
5.3.	Sketch of the three-beam EMCD setup with the four EMCD positions marked as $\pm 1$ and $\pm 2$ . . . . .	46
5.4.	Energy filtered diffraction pattern and E-q diagram. . . . .	47
5.5.	Image of the $\mathbf{0}$ -reflection with the SEA visible as circular aperture. . . . .	49
5.6.	Simulation of the EMCD signal as a function of the sample thickness for a $\text{Ni}_2\text{MnIn}$ sample with zone axis $[001]$ . . . . .	52
5.7.	Simulation of the EMCD signal as a function of the sample thickness for a $\text{Ni}_2\text{MnIn}$ sample with zone axis $[110]$ . . . . .	53
5.8.	Simulation of the EMCD signal as a function of the sample thickness for a $\text{Ni}_2\text{MnSn}$ sample with zone axis $[001]$ . . . . .	53
5.9.	Simulation of the EMCD signal as a function of the sample thickness for a $\text{Ni}_2\text{MnSn}$ sample with zone axis $[110]$ . . . . .	54
5.10.	Simulation of the EMCD signal as a function of the sample thickness for a $\text{Ni}_2\text{MnGa}$ sample with zone axis $[001]$ . . . . .	54
5.11.	Simulation of the EMCD signal as a function of the sample thickness for a $\text{Ni}_2\text{MnGa}$ sample with zone axis $[110]$ . . . . .	55
5.12.	Simulation of the EMCD signal as a function of the sample thickness for a $\text{Co}_2\text{MnSi}$ sample with zone axis $[001]$ . . . . .	55
5.13.	Simulation of the EMCD signal as a function of the sample thickness for a $\text{Co}_2\text{MnSi}$ sample with zone axis $[110]$ . . . . .	56
5.14.	Simulation of the EMCD signal as a function of the sample thickness for a $\text{Co}_2\text{CrAl}$ sample with zone axis $[001]$ . . . . .	56
5.15.	Simulation of the EMCD signal as a function of the sample thickness for a $\text{Co}_2\text{CrAl}$ sample with zone axis $[110]$ . . . . .	57

---

5.16. Comparison of the thickness dependent EMCD simulation for different materials. . . . .	59
5.17. Comparison of the thickness dependent EMCD simulation for a different number of incoming and outgoing Bloch waves. . . . .	60
5.18. Multislice simulation of the EMCD signal. The beam convergence angle was 0.0 mrad, the centre of the electron beam was located at the position of an atomic column. . . . .	61
5.19. Same as figure 5.18 but the beam convergence angle was changed to 2.0 mrad. . . . .	62
5.20. Same as figure 5.18 but the beam convergence angle was changed to 4.0 mrad. . . . .	62
5.21. Same as figure 5.18 but the beam convergence angle was changed to 6.0 mrad. . . . .	63
5.22. Same as figure 5.18 but the beam convergence angle was changed to 10.0 mrad. . . . .	63
5.23. Same as figure 5.18 but the beam convergence angle was changed to 16.0 mrad. . . . .	64
5.24. Same as figure 5.18 but the position of the centre of the electron beam was between the atomic columns. . . . .	65
5.25. Same as figure 5.24 but the beam convergence angle was changed to 16.0 mrad. . . . .	65
5.26. Sketch of the effect of convolution of the low-loss signal with the core-loss signal. . . . .	68
5.27. Sum and difference of the Mn $L_{2,3}$ -edge energy-loss spectra of $\text{Ni}_2\text{MnIn}$ . . . . .	69
5.28. Sum and difference of the Fe $L_{2,3}$ -edge energy-loss spectra of magnetite. . . . .	70
6.1. Schematic of the $Fm\bar{3}m$ structure of Heusler alloys, using $\text{Ni}_2\text{MnSn}$ as example material. . . . .	74
6.2. Sketch of the “5M” (left) and “7M” (right) modulated structures in a top view. . . . .	74
6.3. HRTEM image of a $\text{Ni}_2\text{MnSn}$ Heusler showing martensitic (top) and austenitic regions. . . . .	75
6.4. Structural phase diagram of $\text{NiMnZ}$ Heusler alloys for three different Z-elements: Sn (a), In (b) and Ga (c). . . . .	75

---

6.5. Schematic of the hybridisation of orbitals/energy bands in Heusler materials using the example of $\text{Fe}_2\text{VAl}$ . . . . .	77
6.6. Field cooling and field heating magnetisation measurements of a $\text{Ni}_{50}\text{Mn}_{34.5}\text{In}_{15.5}$ Heusler compound. . . . .	82
6.7. Schematic drawing of the principle of a cooling cycle. . . . .	83
6.8. Bright field TEM image of the IFW $\text{Ni}_2\text{MnSn}$ sample and HRTEM image of the Bielefeld $\text{Ni}_{52}\text{Mn}_{33.3}\text{Sn}_{14.7}$ sample. . . . .	86
6.9. Diffraction patterns of the two $\text{Ni}_2\text{MnSn}$ samples. . . . .	87
6.10. EMCD measurements on the Mn- $L_{2,3}$ edge of the IFW $\text{Ni}_2\text{MnSn}$ Heusler sample. . . . .	88
6.11. EMCD measurements on the Ni- $L_{2,3}$ edge of the IFW $\text{Ni}_2\text{MnSn}$ sample. . . . .	89
6.12. Comparison of the experimentally determined EMCD values of the $\text{Ni}_2\text{MnSn}$ sample with the calculated prediction. . . . .	90
6.13. Comparison of the experimentally determined EMCD values of the $\text{Ni}_2\text{MnSn}$ sample with the calculated prediction. . . . .	90
6.14. Comparison of the experimentally determined EMCD values of the Bielefeld $\text{Ni}_{52}\text{Mn}_{33.3}\text{Sn}_{14.7}$ sample with the calculated prediction . . . . .	91
6.15. Bright field TEM image of the $\text{Ni}_{50}\text{Mn}_{34.5}\text{In}_{15.5}$ sample. . . . .	92
6.16. Diffraction pattern of the $\text{Ni}_{50}\text{Mn}_{34.5}\text{In}_{15.5}$ sample. . . . .	93
6.17. Bright field image of the $\text{Ni}_{50}\text{Mn}_{34.5}\text{In}_{15.5}$ sample after cooling down to 120 K. . . . .	94
6.18. Series of bright field image of the $\text{Ni}_{50}\text{Mn}_{34.5}\text{In}_{15.5}$ sample taken while heating up to room temperature. . . . .	95
6.19. EEL spectra of the Mn- $L_{2,3}$ edge of $\text{Ni}_{50}\text{Mn}_{34.5}\text{In}_{15.5}$ . . . . .	97
6.20. EEL spectra of the Ni- $L_{2,3}$ edge of $\text{Ni}_{50}\text{Mn}_{34.5}\text{In}_{15.5}$ . . . . .	98
6.21. Calculation of the thickness dependence of the EMCD signal in austenitic $\text{Ni}_2\text{MnIn}$ . . . . .	99
6.22. Calculation of the thickness dependence of the EMCD signal in austenitic $\text{Ni}_2\text{MnIn}$ . . . . .	99
6.23. TEM bright field images of the $\text{Ni}_2\text{MnSn} - \text{Ni}_2\text{MnGa}$ double layer sample. . . . .	100
6.24. High resolution TEM image of the $\text{Ni}_2\text{MnSn} - \text{Ni}_2\text{MnGa}$ double-layer. . . . .	101
6.25. Results of an EDX linescan across the two Heusler layers and the Pt barrier layer. . . . .	101

---

6.26. Comparison of the experimentally determined EMCD values of the Ni <sub>2</sub> MnSn – Ni <sub>2</sub> MnGa double-layer with the calculated prediction. . . . .	103
6.27. Comparison of the experimentally determined EMCD values of the Ni <sub>2</sub> MnSn – Ni <sub>2</sub> MnGa double-layer with the calculated prediction. . . . .	103
6.28. Bright field image of the Ni <sub>2</sub> MnSn gradient sample. . . . .	104
6.29. Bright field TEM image of the Ni <sub>2</sub> MnSn gradient sample's region where the other two EMCD experiments were performed. . . . .	106
6.30. Diffraction pattern of the NiCoMnAl Heusler-alloy at different temperat- ures. . . . .	108
6.31. HAADF STEM image and elemental maps of the CoCrAl sample. . . . .	109
7.1. Bright field overview image of the magnetite sample. . . . .	113
7.2. Diffraction patterns of the magnetite sample. . . . .	114
7.3. EMCD spectra acquired in the non transformed sample region. . . . .	115
7.4. EMCD spectra acquired in the transformed sample region. . . . .	115
8.1. Schematic of the rutile unit cell. . . . .	117
8.2. Oxygen projected density of states of rutile above the Fermi-energy. . . . .	117
8.3. Calculation of the Bloch wave amplitudes in a 70 nm thick rutile crystal. . . . .	118
8.4. Sketch of the scattering geometry. . . . .	120
8.5. Sketch of the (110) planes in the rutile crystal and the local coordinate systems of the oxygen atoms. . . . .	121
8.6. Simulated electron energy-loss spectra, the experimental spectra are plot- ted on top of the simulated ones. . . . .	124

# List of Tables

2.1. Extinction distances for 100 keV electrons in different elements. . . . .	14
4.1. Crystallographic data of NiO and TiO <sub>2</sub> as it was used for the conducted simulations. . . . .	32
5.1. Crystal structure of the simulated materials. . . . .	51
5.2. Scattering conditions used for the simulations shown in this section. . . .	52
6.1. Overview of the investigated Heusler-alloys. . . . .	84
6.2. Comparison of the nominal and the experimentally determined elemental compositions of the two Ni <sub>2</sub> MnSn samples. . . . .	86
6.3. Measured EMCD signals on the Mn-L <sub>2,3</sub> edge and the Ni-L <sub>2,3</sub> edge of the two investigated Ni <sub>2</sub> MnSn samples. . . . .	88
6.4. Nominal elemental composition of the NiMnIn Heusler alloy compared to the experimentally determined compositions. . . . .	91
6.5. Measured EMCD signals on the Mn-L <sub>2,3</sub> edge and the Ni-L <sub>2,3</sub> edge of the Ni <sub>50</sub> Mn <sub>34.5</sub> In <sub>15.5</sub> sample. . . . .	96
6.6. Comparison of the nominal and the experimentally determined elemental composition of the Heusler layers in the Ni <sub>2</sub> MnSn – Ni <sub>2</sub> MnGa double layer sample. . . . .	100
6.7. Measured EMCD signals on the Mn-L <sub>2,3</sub> edge and the Ni-L <sub>2,3</sub> edge of the two Heusler layers. . . . .	102
6.8. Elemental composition and composition gradients of the Ni <sub>2</sub> MnSn gradient sample. . . . .	105
6.9. Measured EMCD signals on the Mn-L <sub>2,3</sub> edge and the Ni-L <sub>2,3</sub> edge of the Ni <sub>2</sub> MnSn gradient sample. . . . .	106
6.10. Comparison of the nominal and the experimentally determined elemental composition of the NiCoMnAl sample. . . . .	107



# Bibliography

- [1] Williams, D.B., Carter, C.B. *Transmission Electron Microscopy*. Springer Science+Business Media, 2009. ISBN 978-0-387-76501-3.
- [2] Reimer, L., Kohl, H. *Transmission Electron Microscopy*, volume 36 of *Springer Series in Optical Sciences*. Springer-Verlag Berlin Heidelberg New York Tokyo, 2008. ISBN 3-540-11794-6. doi: 10.1007/987-0-387-40093-8.
- [3] Egerton, R.F. *Electron Energy-Loss Spectroscopy in the Electron Microscope*. Plenum Press New York, second edition, 1996. ISBN 0-306-45223-5.
- [4] Fowler, R.H., Nordheim, L. *Electron emission in intense electric fields*. Proceedings of the Royal Society of London A: Mathematical, Physical and Engineering Sciences, 119(781):173–181, 1928. ISSN 0950-1207. doi: 10.1098/rspa.1928.0091.
- [5] Nelhiebel, M. *Effects of crystal orientation and interferometry in electron energy loss spectroscopy*. Ph.D. thesis, École Centrale Paris, 1999.
- [6] Kohl, H., Rose, H. *Theory of Image Formation by Inelastically Scattered Electrons in the Electron Microscope*. In P.W. Hawkes, editor, *Advances in Electronics and Electron Physics*, volume 65 of *Advances in Electronics and Electron Physics*, pages 173 – 227. Academic Press, 1985. doi: 10.1016/S0065-2539(08)60878-1.
- [7] Allen, L.J., Josefsson, T.W. *Inelastic scattering of fast electrons by crystals*. Phys. Rev. B, 52(5):3184–3198, 1995.
- [8] Allen, L.J., Bell, D.C., Josefsson, T.W., Spargo, A.E.C., Dudarev, S.L. *Inner-shell ionization cross sections and aperture size in electron energy-loss spectroscopy*. Phys. Rev. B, 56:9–11, 1997. doi: 10.1103/PhysRevB.56.9.

- 
- [9] Nelhiebel, M., Louf, P.H., Schattschneider, P., Blaha, P., Schwarz, K., Jouffrey, B. *Theory of orientation-sensitive near-edge fine-structure core-level spectroscopy*. Phys. Rev. B, 59(20):12807–12814, 1999.
- [10] Nelhiebel, M., Schattschneider, P., Jouffrey, B. *Observation of ionization in a crystal interferometer*. Phys. Rev. Lett., 85(9):1847–1850, 2000.
- [11] Löffler, S., Schattschneider, P. *A software package for the simulation of energy-loss magnetic chiral dichroism*. Ultramicroscopy, 110(7):831–835, 2010. ISSN 0304-3991.
- [12] Blaha, P., Schwarz, K., Madsen, G.K.H., Kvasnicka, D., Luitz, J. *Wien2k, an augmented plane wave + local orbitals program for calculating crystal properties*. Technische Universität Wien, Austria, 2001. ISBN 3-9501031-1-2.
- [13] Singh, D.J., Nordstrom, L., editors. *Planewaves, Pseudopotentials, and the LAPW Method*. Springer, second edition, 2006. ISBN 0-387-28780-9.
- [14] Hébert, C. *Practical aspects of running the WIEN2k code for electron spectroscopy*. Micron, 38(1):12–28, 2007. ISSN 0968-4328.
- [15] Hetaba, W. *Fine Structure and Site Specific Energy Loss Spectra of NiO*. Master's thesis, Vienna University of Technology, 2011.
- [16] Löffler, S., Motsch, V., Schattschneider, P. *A pure state decomposition approach of the mixed dynamic form factor for mapping atomic orbitals*. Ultramicroscopy, 131(0):39 – 45, 2013. ISSN 0304-3991. doi: 10.1016/j.ultramic.2013.03.021.
- [17] Hetaba, W., Löffler, S., Willinger, M.G., Schuster, M.E., Schlögl, R., Schattschneider, P. *Site-specific ionisation edge fine-structure of rutile in the electron microscope*. Micron, 63:15 – 19, 2014. ISSN 0968-4328. doi: 10.1016/j.micron.2014.02.008.
- [18] Kittel, C. *Einführung in die Festkörperphysik*. Oldenbourg Verlag, 2006. ISBN 3-486-57723-9.
- [19] Howie, A., Whelan, M.J. *Diffraction Contrast of Electron Microscope Images of Crystal Lattice Defects. II. The Development of a Dynamical Theory*. Proceedings of the Royal Society of London. Series A, Mathematical and Physical Sciences, 263(1313):217–237, 1961. ISSN 00804630.

- 
- [20] Howie, A., Whelan, M.J. *Diffraction Contrast of Electron Microscope Images of Crystal Lattice Defects. III. Results and Experimental Confirmation of the Dynamical Theory of Dislocation Image Contrast*. Proceedings of the Royal Society of London. Series A, Mathematical and Physical Sciences, 267(1329):206–230, 1962. ISSN 00804630.
- [21] Bethe, H. *Theorie der Beugung von Elektronen an Kristallen*. Annalen der Physik, 392(17):55–129, 1928. ISSN 1521-3889. doi: 10.1002/andp.19283921704.
- [22] Krivanek, O., Disko, M., Taftø, J., Spence, J. *Electron energy loss spectroscopy as a probe of the local atomic environment*. Ultramicroscopy, 9(3):249–254, 1982. ISSN 0304-3991.
- [23] Löffler, S. *Study of real space wave functions with electron energy loss spectrometry*. Ph.D. thesis, Technische Universität Wien, 2013.
- [24] Pogany, A.P., Turner, P.S. *Reciprocity in electron diffraction and microscopy*. Acta Crystallographica Section A, 24(1):103–109, 1968. doi: 10.1107/S0567739468000136.
- [25] Schattschneider, P. *Fundamentals of Inelastic Electron Scattering*. Springer-Verlag Wien New York, 1986. ISBN 3-211-81937-1.
- [26] Schattschneider, P., Nelhiebel, M., Jouffrey, B. *Density matrix of inelastically scattered fast electrons*. Phys. Rev. B, 59(16):10959–10969, 1999.
- [27] Rusz, J., Rubino, S., Schattschneider, P. *First-principles theory of chiral dichroism in electron microscopy applied to 3d ferromagnets*. Phys. Rev. B, 75(21):214425, 2007.
- [28] Villars, P., Calvert, L., editors. *Pearson’s Handbook of Crystallographic Data for Intermetallic Phases*. ASM International, 1996. ISBN 0-87170-416-1.
- [29] Taftø, J., Spence, J. *Atomic site determination using the channeling effect in electron-induced X-ray emission*. Ultramicroscopy, 9(3):243–247, 1982. ISSN 0304-3991.

- [30] Taftø, J., Spence, J.C.H. *Crystal Site Location of Iron and Trace Elements in a Magnesium-Iron Olivine by a New Crystallographic Technique*. *Science*, 218(4567):49–51, 1982. doi: 10.1126/science.218.4567.49.
- [31] Spence, J., Taftø, J. *ALCHEMI: a new technique for locating atoms in small crystals*. *Journal of Microscopy*, 130(Pt 2):147–154, 1983. ISSN 0022-2720.
- [32] Taftø, J., Krivanek, O. *Characteristic energy losses from channeled 100 keV electrons*. *Nuclear Instruments and Methods in Physics Research*, 194(1-3):153–158, 1982. ISSN 0167-5087.
- [33] Taftø, J., Liliental, Z. *Studies of the cation atom distribution in  $ZnCr_xFe_{2-x}O_4$  spinels using the channeling effect in electron-induced X-ray emission*. *J. Appl. Cryst.*, 15(3):260–265, 1982. ISSN 1600-5767.
- [34] Taftø, J., Krivanek, O.L. *Site-Specific Valence Determination by Electron Energy-Loss Spectroscopy*. *Phys. Rev. Lett.*, 48(8):560–563, 1982.
- [35] Nüchter, W., Sigle, W. *Electron channelling: A method in real-space crystallography and a comparison with the atomic location by channelling-enhanced microanalysis*. *Philosophical Magazine A*, 71(1):165–186, 1995. ISSN 0141-8610.
- [36] Arai, S., Muto, S., Sasaki, T., Tatsumi, K., Ukyo, Y., Kuroda, K., Saka, H. *Novel valence state of cerium in  $Ce_2Zr_2O_{7.5}$  elucidated by electron energy-loss spectroscopy under electron channeling conditions*. *Solid State Commun.*, 135(11-12):664–667, 2005. ISSN 0038-1098.
- [37] Tatsumi, K., Sasano, Y., Muto, S., Yoshida, T., Sasaki, T., Horibuchi, K., Takeuchi, Y., Ukyo, Y. *Local atomic and electronic structures around Mg and Al dopants in  $LiNiO_2$  electrodes studied by XANES and ELNES and first-principles calculations*. *Phys. Rev. B*, 78(4):045108, 2008.
- [38] Tatsumi, K., Muto, S., Yamamoto, Y., Ikeno, H., Yoshioka, S., Tanaka, I. *Site-specific electronic structure analysis by channeling EELS and first-principles calculations*. *Ultramicroscopy*, 106(11-12):1019–1023, 2006. ISSN 0304-3991.
- [39] Yamamoto, Y., Tatsumi, K., Muto, S. *Site-Selective Electronic Structure of Aluminum in Oxide Ceramics Obtained by TEM-EELS Analysis Using the Elec-*

- tron Standing-Wave Method*. Materials Transactions, 48(10):2590–2594, 2007. doi: 10.2320/matertrans.MD200707.
- [40] Hébert, C., Schattschneider, P. *A proposal for dichroic experiments in the electron microscope*. Ultramicroscopy, 96(3-4):463–468, 2003. ISSN 0304-3991.
- [41] Schattschneider, P., Rubino, S., Hébert, C., Rusz, J., Kuneš, J., Novák, P., Carlino, E., Fabrizioli, M., Panaccione, G., Rossi, G. *Detection of magnetic circular dichroism using a transmission electron microscope*. Nature, 441(7092):486–488, 2006. ISSN 0028-0836.
- [42] Rusz, J., Muto, S., Tatsumi, K. *New algorithm for efficient Bloch-waves calculations of orientation-sensitive ELNES*. Ultramicroscopy, 125(0):81 – 88, 2013. ISSN 0304-3991. doi: 10.1016/j.ultramic.2012.09.009.
- [43] Rusz, J., Eriksson, O., Novák, P., Oppeneer, P.M. *Sum rules for electron energy loss near edge spectra*. Phys. Rev. B, 76(6):060408, 2007.
- [44] Calmels, L., Houdellier, F., Warot-Fonrose, B., Gatel, C., Hÿtch, M.J., Serin, V., Snoeck, E., Schattschneider, P. *Experimental application of sum rules for electron energy loss magnetic chiral dichroism*. Phys. Rev. B, 76:060409, 2007. doi: 10.1103/PhysRevB.76.060409.
- [45] Schattschneider, P., Hébert, C., Rubino, S., Stöger-Pollach, M., Rusz, J., Novák, P. *Magnetic circular dichroism in EELS: Towards 10 nm resolution*. Ultramicroscopy, 108(5):433–438, 2008. ISSN 0304-3991.
- [46] Schattschneider, P., Stöger-Pollach, M., Rubino, S., Sperl, M., Hurm, C., Zweck, J., Rusz, J. *Detection of magnetic circular dichroism on the two-nanometer scale*. Phys. Rev. B, 78(10):104413, 2008.
- [47] Rusz, J., Rubino, S., Eriksson, O., Oppeneer, P.M., Leifer, K. *Local electronic structure information contained in energy-filtered diffraction patterns*. Phys. Rev. B, 84(6):064444, 2011.
- [48] Rusz, J., Idrobo, J.C., Bhowmick, S. *Achieving atomic resolution magnetic dichroism by controlling the phase symmetry of an electron probe*. Phys. Rev. Lett., 113:145501, 2014. doi: 10.1103/PhysRevLett.113.145501.

- [49] Schattschneider, P., Schaffer, B., Ennen, I., Verbeeck, J. *Mapping spin-polarized transitions with atomic resolution.* Phys. Rev. B, 85:134422, 2012. doi: 10.1103/PhysRevB.85.134422.
- [50] Stöger-Pollach, M., Treiber, C., Resch, G., Keays, D., Ennen, I. *EMCD real space maps of Magnetospirillum magnetotacticum.* Micron, 42(5):456 – 460, 2011. ISSN 0968-4328. doi: 10.1016/j.micron.2011.01.003.
- [51] Ennen, I., Löffler, S., Kübel, C., Wang, D., Auge, A., Hütten, A., Schattschneider, P. *Site-specific chirality in magnetic transitions.* Journal of Magnetism and Magnetic Materials, 324(18):2723 – 2726, 2012. ISSN 0304-8853. doi: 10.1016/j.jmmm.2012.03.050.
- [52] Loukya, B., Negi, D.S., Dileep, K., Pachauri, N., Gupta, A., Datta, R. *Effect of bloch wave electron propagation and momentum-resolved signal detection on the quantitative and site-specific electron magnetic chiral dichroism of magnetic spinel oxide thin films.* Phys. Rev. B, 91:134412, 2015. doi: 10.1103/PhysRevB.91.134412.
- [53] Rubino, S., Schattschneider, P., Stöger-Pollach, M., Hébert, C., Rusz, J., Calmels, L., Warot-Fonrose, B., Houdellier, F., Serin, V., Novak, P. *Energy-loss magnetic chiral dichroism (EMCD): Magnetic chiral dichroism in the electron microscope.* Journal of Materials Research, 23(10):2582–2590, 2008. doi: 10.1557/JMR.2008.0348.
- [54] Warot-Fonrose, B., Gatel, C., Calmels, L., Serin, V., Schattschneider, P. *Effect of spatial and energy distortions on energy-loss magnetic chiral dichroism measurements: Application to an iron thin film.* Ultramicroscopy, 110(8):1033 – 1037, 2010. ISSN 0304-3991. doi: 10.1016/j.ultramic.2009.12.011.
- [55] Hébert, C., Schattschneider, P., Rubino, S., Novak, P., Rusz, J., Stöger-Pollach, M. *Magnetic circular dichroism in electron energy loss spectrometry.* Ultramicroscopy, 108(3):277 – 284, 2008. ISSN 0304-3991. doi: 10.1016/j.ultramic.2007.07.011.
- [56] Löffler, S., Schattschneider, P. *Transition probability functions for applications of inelastic electron scattering.* Micron, 43(9):971 – 977, 2012. ISSN 0968-4328. doi: 10.1016/j.micron.2012.03.020.

- [57] Rubino, S. *Magnetic Circular Dichroism in the Transmission Electron Microscope*. Ph.D. thesis, Technische Universität Wien, 2007.
- [58] Schattschneider, P. *Linear and Chiral Dichroism in the Electron Microscope*. Pan Stanford Publishing Pte. Ltd., Singapore, 2012.
- [59] Idrobo, J.C., Pennycook, S.J. *Vortex beams for atomic resolution dichroism*. Journal of Electron Microscopy, 60(5):295–300, 2011. doi: 10.1093/jmicro/dfr069.
- [60] O’Brien, W.L., Tonner, B.P. *Orbital and spin sum rules in x-ray magnetic circular dichroism*. Phys. Rev. B, 50:12672–12681, 1994. doi: 10.1103/PhysRevB.50.12672.
- [61] Schattschneider, P., Rubino, S., Stöger-Pollach, M., Hébert, C., Rusz, J., Calmels, L., Snoeck, E. *Energy loss magnetic chiral dichroism: A new technique for the study of magnetic properties in the electron microscope (invited)*. Journal of Applied Physics, 103(7):07D931, 2008.
- [62] Rusz, J., Lidbaum, H., Rubino, S., Hjörvarsson, B., Oppeneer, P.M., Eriksson, O., Leifer, K. *Influence of plural scattering on the quantitative determination of spin and orbital moments in electron magnetic chiral dichroism measurements*. Phys. Rev. B, 83:132402, 2011. doi: 10.1103/PhysRevB.83.132402.
- [63] Chen, C.T., Idzerda, Y.U., Lin, H.J., Smith, N.V., Meigs, G., Chaban, E., Ho, G.H., Pellegrin, E., Sette, F. *Experimental Confirmation of the X-Ray Magnetic Circular Dichroism Sum Rules for Iron and Cobalt*. Phys. Rev. Lett., 75:152–155, 1995. doi: 10.1103/PhysRevLett.75.152.
- [64] Klaer, P., Herper, H.C., Entel, P., Niemann, R., Schultz, L., Fähler, S., Elmers, H.J. *Electronic structure of the austenitic and martensitic state of magnetocaloric Ni-Mn-In Heusler alloy films*. Phys. Rev. B, 88:174414, 2013. doi: 10.1103/PhysRevB.88.174414.
- [65] Wang, Z., Zhong, X., Yu, R., Cheng, Z., Zhu, J. *Quantitative experimental determination of site-specific magnetic structures by transmitted electrons*. Nat Commun, 4:1395, 2013.
- [66] Huang, D.J., Chang, C.F., Jeng, H.T., Guo, G.Y., Lin, H.J., Wu, W.B., Ku, H.C., Fujimori, A., Takahashi, Y., Chen, C.T. *Spin and Orbital Magnetic Moments of Fe<sub>3</sub>O<sub>4</sub>*. Phys. Rev. Lett., 93:077204, 2004. doi: 10.1103/PhysRevLett.93.077204.

- [67] Graf, T., Felser, C., Parkin, S.S. *Simple rules for the understanding of Heusler compounds*. Progress in Solid State Chemistry, 39(1):1 – 50, 2011. ISSN 0079-6786. doi: 10.1016/j.progsolidstchem.2011.02.001.
- [68] Planes, A., Mañosa, L., Acet, M. *Magnetocaloric effect and its relation to shape-memory properties in ferromagnetic Heusler alloys*. Journal of Physics: Condensed Matter, 21(23):233201, 2009.
- [69] Meinert, M. *Modified Becke-Johnson potential investigation of half-metallic Heusler compounds*. Phys. Rev. B, 87(4):045103, 2013.
- [70] Fecher, G.H., Kandpal, H.C., Wurmehl, S., Morais, J., Lin, H.J., Elmers, H.J., Schönhense, G., Felser, C. *Design of magnetic materials: the electronic structure of the ordered, doped Heusler compound  $\text{Co}_2\text{Cr}_{1-x}\text{Fe}_x\text{Al}$* . Journal of Physics: Condensed Matter, 17(46):7237, 2005. doi: 10.1088/0953-8984/17/46/008.
- [71] Pecharsky, V.K., Gschneidner, K.A. *Magnetocaloric effect from indirect measurements: Magnetization and heat capacity*. Journal of Applied Physics, 86(1):565–575, 1999. doi: 10.1063/1.370767.
- [72] Rojas, D.P., Espeso, J.I., Rodríguez Fernández, J., Gómez Sal, J.C., Sanchez Marcos, J., Müller, H. *First order ferromagnetic transition in binary  $\text{CeIn}_2$* . Phys. Rev. B, 80:184413, 2009. doi: 10.1103/PhysRevB.80.184413.
- [73] Fähler, S., Rössler, U.K., Kastner, O., Eckert, J., Eggeler, G., Emmerich, H., Entel, P., Müller, S., Quandt, E., Albe, K. *Caloric effects in ferroic materials: New concepts for cooling*. Advanced Engineering Materials, 14(1-2):10–19, 2012. ISSN 1527-2648. doi: 10.1002/adem.201100178.
- [74] Meinert, M., Hübner, T., Schmalhorst, J., Reiss, G., Arenholz, E. *Phase separation in  $\text{Fe}_2\text{CrSi}$  thin films*. Journal of Applied Physics, 114(11):113908, 2013. doi: 10.1063/1.4821972.
- [75] Geisler, M.P., Meinert, M., Schmalhorst, J., Reiss, G., Arenholz, E. *Multiple phases in sputtered  $\text{Cr}_2\text{CoGa}$  films*. Journal of Alloys and Compounds, 598:213 – 216, 2014. ISSN 0925-8388. doi: 10.1016/j.jallcom.2014.02.035.



- [76] Jourdan, M., Minár, J., Braun, J., Kronenberg, A., Chadov, S., Balke, B., Gloskovskii, A., Kolbe, M., Elmers, H., Schönhense, G., Ebert, H., Felser, C., Kläui, M. *Direct observation of half-metallicity in the Heusler compound  $\text{Co}_2\text{MnSi}$* . Nat Commun, 5(3974), 2014.
- [77] Weiss, W., Ranke, W. *Surface chemistry and catalysis on well-defined epitaxial iron-oxide layers*. Progress in Surface Science, 70(1–3):1 – 151, 2002. ISSN 0079-6816. doi: 10.1016/S0079-6816(01)00056-9.
- [78] Willinger, M.G., Zhang, W., Bondarchuk, O., Shaikhutdinov, S., Freund, H.J., Schlögl, R. *A case of strong metal–support interactions: Combining advanced microscopy and model systems to elucidate the atomic structure of interfaces*. Angewandte Chemie International Edition, 53(23):5998–6001, 2014. ISSN 1521-3773. doi: 10.1002/anie.201400290.
- [79] Walz, F. *The Verwey transition - a topical review*. Journal of Physics: Condensed Matter, 14(12):R285, 2002.
- [80] de la Figuera, J., Novotny, Z., Setvin, M., Liu, T., Mao, Z., Chen, G., N’Diaye, A.T., Schmid, M., Diebold, U., Schmid, A.K., Parkinson, G.S. *Real-space imaging of the verwey transition at the (100) surface of magnetite*. Phys. Rev. B, 88:161410, 2013. doi: 10.1103/PhysRevB.88.161410.
- [81] Kasama, T., Church, N.S., Feinberg, J.M., Dunin-Borkowski, R.E., Harrison, R.J. *Direct observation of ferrimagnetic/ferroelastic domain interactions in magnetite below the verwey transition*. Earth and Planetary Science Letters, 297(1–2):10 – 17, 2010. ISSN 0012-821X. doi: 10.1016/j.epsl.2010.05.004.
- [82] Sorantin, P.I., Schwarz, K. *Chemical bonding in rutile-type compounds*. Inorganic Chemistry, 31(4):567–576, 1992. doi: 10.1021/ic00030a009.
- [83] Laskowski, R., Blaha, P. *Understanding the  $L_{2,3}$  x-ray absorption spectra of early 3d transition elements*. Phys. Rev. B, 82(20):205104, 2010.
- [84] Hetaba, W., Blaha, P., Tran, F., Schattschneider, P. *Calculating energy loss spectra of NiO: Advantages of the modified Becke-Johnson potential*. Phys. Rev. B, 85(20):205108, 2012.

- 
- [85] Schattschneider, P., Nelhiebel, M., Souchay, H., Jouffrey, B. *The physical significance of the mixed dynamic form factor*. *Micron*, 31(4):333–345, 2000. ISSN 0968-4328.
- [86] Löffler, S., Ennen, I., Tian, F., Schattschneider, P., Jaouen, N. *Breakdown of the dipole approximation in core losses*. *Ultramicroscopy*, 111(8):1163–1167, 2011. ISSN 0304-3991. doi: 10.1016/j.ultramic.2011.03.006.

Suavis laborum est praeteritorum memoria.

Marcus Tullius Cicero, De finibus bonorum et malorum

# Curriculum Vitae

## Dipl.-Ing. Walid Hetaba

### Persönliche Daten:

Name: Walid HETABA  
Geburtsort und -datum: St. Pölten, 28.08.1985  
Nationalität: Österreich

Anstellung: Elektronenmikroskopiker  
Universitäre Service-Einrichtung für  
Transmissions-Elektronenmikroskopie (USTEM)  
Technische Universität Wien  
Wiedner Hauptstraße 8-10, 1040 Wien, Österreich

Kontakt: [walid.hetaba@tuwien.ac.at](mailto:walid.hetaba@tuwien.ac.at)  
<http://www.ustem.tuwien.ac.at/staff/hetaba/>

### Ausbildung:

1995 – 2003: Bundesrealgymnasium Krems Ringstraße  
04. 06. 2003: Reifeprüfung, mit ausgezeichnetem Erfolg bestanden  
Jan. – Sep. 2004: Präsenzdienst beim PzB 10 in Spratzern/St. Pölten  
2004 – 2011: Studium der Technischen Physik an der Technischen Universität  
Wien, mit Auszeichnung bestanden

12.12.2006: 1. Diplomprüfung  
Mar. – Aug. 2008: ERASMUS Auslandssemester an der Humboldt-Universität zu Berlin  
08.02.2011: 2. Diplomprüfung, mit Auszeichnung bestanden  
22.06.2011: 3. Diplomprüfung, mit Auszeichnung bestanden  
seit Sep. 2011: Doktoratsstudium der technischen Wissenschaften, Fachrichtung  
Technische Physik an der Technischen Universität Wien

### Arbeits- und Auslandserfahrung:

2006 – 2010: Tutor am Institut für allgemeine Physik/Institut für angewandte  
Physik, TU Wien

Mar. – Aug. 2008: ERASMUS Auslandssemester an der Humboldt-Universität zu Berlin

2010 – 2011: Tutor am Institut für Analysis und Scientific Computing, TU Wien  
2011 – 2012: Projektassistent am Institut für Festkörperphysik, TU Wien  
2012, 2013: Wissenschaftliche Aufenthalte am Fritz-Haber-Institut der Max-  
Planck-Gesellschaft in Berlin

2013 – 2014: Wissenschaftlicher Mitarbeiter in der AG Dünne Schichten & Physik  
der Nanostrukturen, Fakultät für Physik, Universität Bielefeld

seit 2013: Elektronenmikroskopiker am USTEM, TU Wien  
2014 – 2015: Stipendiat der Max-Planck-Gesellschaft

## Lehrerfahrung:

2006W:	134.109 UE Grundlagen der Physik I, Tutor
2007S:	134.110 UE Grundlagen der Physik II, Tutor
2007W:	134.124 PR Laborübungen II, Tutor
	134.125 UE Grundlagen der Physik III, Tutor
2008W:	134.109 UE Grundlagen der Physik I, Tutor
2009S:	134.110 UE Grundlagen der Physik II, Tutor
2009W:	134.124 PR Laborübungen II, Tutor
	134.125 UE Grundlagen der Physik III, Tutor
2010S:	134.126 PR Laborübungen III, Tutor
2010W:	101.423 VU Auffrischkurs Mathematik für TPH, Tutor

## Studienvertretung und Kommissionen:

Jan. 2007 – Nov. 2010:	Studienkommission Technische Physik, studentisches Hauptmitglied
Apr. 2007 – Apr. 2009:	Arbeitsgruppe „Laborsanierung“, studentisches Mitglied
Mai – Jul. 2007:	Habilitationskommission Prokofiev – Materialwissenschaft, studentisches Ersatzmitglied
Mai – Sep. 2009:	Habilitationskommission Marton – Experimentalphysik, studentisches Ersatzmitglied
Jul. 2007 – Jun. 2009:	1. stellvertretender Vorsitzender der Studienvertretung Technische Physik
Okt. 2007 – Jan. 2010:	Berufungskommission „Oberflächenphysik“, studentisches Hauptmitglied
Jun. – Okt. 2008:	Habilitationskommission Gebeshuber – Experimentalphysik, studentisches Hauptmitglied
Nov. 2008 – Okt. 2010:	Berufungskommission „Experimentelle Festkörperphysik“, studentisches Hauptmitglied
Dez. 2009 – Jul. 2011:	Berufungskommission „Biophysik“, studentisches Ersatzmitglied
Okt. 2011 – Mar. 2015:	Studienkommission für die Doktoratsstudien, studentisches Hauptmitglied
Dez. 2011 – Jun. 2012:	Habilitationskommission Stöger-Pollach – Elektronenmikroskopie, studentisches Ersatzmitglied
Nov. 2011 – Okt. 2012:	Stellvertretender Vorsitzender der Studienkommission für die Doktoratsstudien
Okt. 2012 – Mar. 2014:	Vorsitzender der Studienkommission für die Doktoratsstudien
Jul. 2013 – Jun. 2015:	1. stellvertretender Vorsitzender der Studienvertretung Doktorat; Ersatzmitglied in der Universitätsvertretung der Hochschülerschaft an der TU Wien
Jan. 2014 – Jun. 2014:	Habilitationskommission Ipp – Theoretische Physik, studentisches Hauptmitglied
seit Jun. 2014:	Fakultätsrat der Fakultät für Physik, studentisches Hauptmitglied

### Auszeichnungen:

2003:	Franz-Haschkovitz-Preis
2011:	Best Poster Award: 16. Tagung Festkörperanalytik, Wien
2011:	Best Poster Award: 10 <sup>th</sup> Multinational Congress on Microscopy, Urbino, Italien

### Sprachfähigkeiten:

Deutsch:	Muttersprache
Englisch:	Cambridge ESOL Certificate in Advanced English, Grade A
Latein:	Realgymnasium, 12 Wochenstunden, schriftliche Reifeprüfung
Arabisch:	Grundkenntnisse in der Hochsprache, erweiterte Kenntnisse im ägyptischen Dialekt

### Vereinstätigkeiten:

- Österreichische Gesellschaft für Elektronenmikroskopie, österreichischer Ländervertreter im Arbeitskreis EELS/EFTEM
- Verein der Freunde der Festkörperphysik und -chemie, Obmann
- Deutsche Physikalische Gesellschaft
- Deutsche Gesellschaft für Elektronenmikroskopie

## Publikationsliste

Stand: August 2015

### Zeitschriftenartikel

1. Jan Rogge, Walid Hetaba, Jan Schmalhorst, Houari Bouchikhaoui, Patrick Stender, Dietmar Baither, Guido Schmitz, Andreas Hütten:  
*Co<sub>2</sub>FeAl based magnetic tunnel junctions with BaO and MgO/BaO barriers*  
AIP Advances **5** (2015), 077173
2. Edvinas Navickas, Tobias M. Huber, Yan Chen, Walid Hetaba, Gerald Holzlechner, Ghislain Rupp, Michael Stöger-Pollach, Gernot Friedbacher, Herbert Hutter, Bilge Yildiz, Jürgen Fleig:  
*Fast oxygen exchange and diffusion kinetics of grain boundaries in Sr-doped LaMnO<sub>3</sub> thin films*  
Physical Chemistry Chemical Physics **17**, 12 (2015), 7659-7669
3. Markus Meinert, Manuel P. Geisler, Jan Schmalhorst, Ulrich Heinzmann, Elke Arenholz, Walid Hetaba, Michael Stöger-Pollach, Andreas Hütten, Günter Reiss:  
*Experimental realization of a semiconducting full-Heusler compound: Fe<sub>2</sub>TiSi*  
Physical Review B **90** (2014), 085127
4. Thomas Huber, Bernhard Bergmair, Christoph Vogler, Florian Bruckner, Leoni Breth, Walid Hetaba, Gino Hrkac, Dieter Süss:  
*Ultra low-cost RFID based on soft magnetic ribbons*  
IEEE Transactions on Magnetics, accepted
5. Walid Hetaba, Stefan Löffler, Marc-Georg Willinger, Manfred Erwin Schuster, Robert Schlögl, Peter Schattschneider:  
*Site-specific ionisation fine-structure of Rutile in the electron microscope*  
Micron **63** (2014), 15-19
6. Michaela Kogler, Eva-Maria Köck, Lukas Perfler, Thomas Bielz, Michael Stöger-Pollach, Walid Hetaba, Marc Willinger, Xing Huang, Manfred Schuster, Bernhard Klötzer, Simon Penner:  
*Methane Decomposition and Carbon Growth on Y<sub>2</sub>O<sub>3</sub>, Yttria-Stabilized Zirconia, and ZrO<sub>2</sub>*  
Chemistry of Materials **26**, 4 (2014), 1690-1701
7. Annalena Wolff, Walid Hetaba, Marco Wißbrock, Stefan Löffler, Nadine Mill, Katrin Eckstädt, Axel Dreyer, Inga Ennen, Norbert Sewald, Peter Schattschneider, Andreas Hütten:  
*Oriented attachment explains cobalt ferrite nanoparticle growth in bioinspired syntheses*  
Beilstein Journal of Nanotechnology **5** (2014), 210-218

8. Ramona Thalinger, Michael Stöger-Pollach, Walid Hetaba, Michael Feuerbacher, Bernhard Klötzer, Simon Penner:  
*Electron microscopy investigations of meta-support interaction effects in M/Y<sub>2</sub>O<sub>3</sub> and M/ZrO<sub>2</sub> thin films (M=Cu, Ni)*  
Materials Chemistry and Physics **143**, 1 (2013), 167-177
9. Annalena Wolff, Katrin Frese, Marco Wißbrock, Katrin Eckstädt, Inga Ennen, Walid Hetaba, Stefan Löffler, Anna Regtmeier, Patrick Thomas, Norbert Sewald, Peter Schattschneider, Andreas Hütten:  
*Influence of the synthetic polypeptide c25-mms6 on cobalt ferrite nanoparticle formation*  
Journal of Nanoparticle Research **14** (2012), 1161
10. Walid Hetaba, Peter Blaha, Fabien Tran, Peter Schattschneider:  
*Calculating energy loss spectra of NiO: Advantages of the modified Becke-Johnson potential*  
Physical Review B **85** (2012), 205108
11. Walid Hetaba, Anna Mogilatenko, Wolfgang Neumann:  
*Electron beam-induced oxygen desorption in  $\gamma$ -LiAlO<sub>2</sub>*  
Micron **41**, 5 (2010), 479-483
12. Wolfgang Neumann, Holm Kirmse, Ines Häusler, Anna Mogilatenko, Changling Zheng, Walid Hetaba:  
*Advanced microstructure diagnostics and interface analysis of modern materials by high-resolution analytical transmission electron microscopy*  
Bulletin of the Polish Academy of Sciences: Technical Sciences **58**, 2 (2010), 237-253

#### Buchbeiträge:

1. Walid Hetaba:  
*Die physikalische Forschung an der Technischen Hochschule in Wien 1938 – 1945 im Spiegel der Dissertationen*  
in: *Österreichische Hochschulen im 20. Jahrhundert; Austrofaschismus, Nationalsozialismus und die Folgen*, Österreichische HochschülerInnenschaft (Hg.), Facultas.wuv, 2013, ISBN: 978-3-7089-1031-4

#### Vorträge und Posterpräsentationen (mit Tagungsband-Eintrag):

1. Walid Hetaba, Stefan Löffler, Michael Stöger-Pollach, Andreas Hütten, Gareth Parkinson, Peter Schattschneider:  
*EMCD as a probe for magnetic phase transitions*  
Vortrag: Microscopy Conference 2015, Georg-August-Universität Göttingen, BRD; 06.09.2015 – 11.09.2015; in: „MC2015 Proceedings“, (2015), S.535-537



2. Walid Hetaba, Stefan Löffler, Michael Stöger-Pollach, Andreas Hütten, Gareth Parkinson, Peter Schattschneider:  
*Probing magnetic phase transitions using EMCD*  
Vortrag: 12<sup>th</sup> Multinational Congress on Microscopy, Eger, Ungarn; 23.08.2015 – 28.08.2015;  
in: "12<sup>th</sup> Multinational Congress on Microscopy", Hungarian Academy of Sciences, Eger, Ungarn (2015), S. 252-254
  
3. T. Huber, E. Navickas, D. Takeshi, G. Harrington, N. Perry, G. Rupp, W. Hetaba, M. Stöger-Pollach, H. Tuller, B. Yildiz, K. Sasaki, J. Fleig:  
*Bias Enhanced Fast Oxygen Exchange and Diffusion Kinetics of Grain Boundaries in LSM Thin Films*  
Poster: 20th International Conference on Solid State Ionics, Colorado; 14.06.2015 – 19.06.2015; in: "20th International Conference on Solid State Ionics", (2015), S. 68
  
4. Walid Hetaba, Stefan Löffler, Michael Stöger-Pollach, Andreas Hütten, Gareth Parkinson, Marc-Georg Willinger, Robert Schlögl:  
*Probing magnetic phase transitions in Heusler-alloys and Magnetite using EMCD*  
Poster: 79<sup>th</sup> Annual Meeting of the DPG and Spring Meeting of the Condensed Matter Section, Berlin; 15.03.2015 – 20.03.2015
  
5. M. Stöger-Pollach, T. Schachinger, W. Hetaba, D. Abou-Ras, R. Rodemeier:  
*Low Voltage EELS and Bessel Beams in Semiconductor Science*  
Vortrag: SALVE - Symposium 2015, University of Ulm, BRD (eingeladen); 17.02.2015 – 18.02.2015; in: "SALVE - Sub-Angstrom Low-Voltage Electron Microscopy", (2015)
  
6. Walid Hetaba, Niclas Teichert, Andreas Hütten, P. Schattschneider:  
*TEM investigation of multilayer-Heusler systems for ferroic cooling applications*  
Poster: 18<sup>th</sup> International Microscopy Congress, Prag; 07.09.2014 - 12.09.2014; in: "18<sup>th</sup> International Microscopy Congress Proceedings", Czechoslovak Microscopy Society, (2014), ISBN: 978-80-260-6720-7; Paper-Nr. MS-7-P-265, 2 S
  
7. M. Stöger-Pollach, W. Hetaba, R. Rodemeier:  
*An ELNES study of anisotropic materials using variable beam energies*  
Poster: 18<sup>th</sup> International Microscopy Congress, Prag; 07.09.2014 – 12.09.2014; in: "18<sup>th</sup> International Microscopy Congress Proceedings", Czechoslovak Microscopy Society, (2014), ISBN: 978-80-260-6720-7; Paper-Nr. IT-5-P-2163, 2 S
  
8. Walid Hetaba, Marc-Georg Willinger, Manfred Erwin Schuster, Stefan Löffler, Robert Schlögl, Peter Schattschneider:  
*Site-specific ionisation edge fine-structure in the electron microscope*  
Poster: Microscopy Conference 2013, Universität Regensburg, BRD; 25.08.2013 – 30.08.2013; in: *MC2013 Proceedings Part 1* (2013), 200-201

9. Walid Hetaba, Annalena Wolff, Nadine Mill, Marco Wißbrock, Norbert Sewald, Andreas Hütten:  
*TEM analysis of the influence of the synthetic polypeptide c25-mms6 on the cobalt ferrite nanoparticle growth*  
Poster: Microscopy Conference 2013, Universität Regensburg, BRD; 25.08.2013 – 30.08.2013;  
in: *MC2013 Proceedings Part 1* (2013), 425-426
10. Stefan Löffler, Viktoria Motsch, Walid Hetaba, Ralf Hambach, Giulio Biddau, Lorenzo Pardini, Claudia Draxl, Ute Kaiser, Peter Schattschneider:  
*Towards mapping atomic orbitals in the TEM*  
Poster: Microscopy Conference 2013, Universität Regensburg, BRD; 25.08.2013 – 30.08.2013;  
in: *MC2013 Proceedings Part 1* (2013), 198-199
11. Walid Hetaba, Stefan Löffler, Peter Schattschneider:  
*Site-specific elemental analysis under electron channelling conditions*  
Vortrag: 15<sup>th</sup> European Microscopy Congress, Manchester, UK; 16.09.2012 – 21.09.2012; in:  
*Proceedings of the 15<sup>th</sup> European Microscopy Congress*, D.J. Stokes, W.M. Rainforth (Hrg.);  
The Royal Microscopic Society, Vol. 2: Physical Sciences: Tools and Techniques (2012), ISBN:  
978-0-9502463-6-9; 497
12. Michael Stöger-Pollach, Walid Hetaba, Stefan Löffler:  
*Is there a chance for mapping optical properties of buried quantum structures by means of Low Voltage Valence EELS in a STEM?*  
Poster: 15<sup>th</sup> European Microscopy Congress, Manchester, UK; 16.09.2012 – 21.09.2012; in:  
*Proceedings of the 15<sup>th</sup> European Microscopy Congress*, D.J. Stokes, W.M. Rainforth (Hrg.);  
The Royal Microscopic Society, Vol. 1: Physical Sciences: Applications (2012), ISBN: 978-0-  
9502463-5-2; 935
13. Walid Hetaba, Annalena Wolff, Stefan Löffler, Katrin Frese, Katrin Eckstädt, Norbert Sewald, Andreas Hütten:  
*Influence of the polypeptide c25-mms6 on the Cobalt Ferrite nanoparticle formation analysed by TEM and EELS*  
Poster: 15<sup>th</sup> European Microscopy Congress, Manchester, UK; 16.09.2012 – 21.09.2012; in:  
*Proceedings of the 15<sup>th</sup> European Microscopy Congress*, D.J. Stokes, W.M. Rainforth (Hrg.);  
The Royal Microscopic Society, Vol. 1: Physical Sciences: Applications (2012), ISBN: 978-0-  
9502463-5-2; 491
14. Walid Hetaba, Stefan Löffler, Peter Blaha, Fabien Tran, Peter Schattschneider:  
*EELS of NiO: Advantages of core-hole calculations using the modified Becke-Johnson potential*  
Poster: 15<sup>th</sup> European Microscopy Congress, Manchester, UK; 16.09.2012 – 21.09.2012; in:  
*Proceedings of the 15<sup>th</sup> European Microscopy Congress*, D.J. Stokes, W.M. Rainforth (Hrg.);  
The Royal Microscopic Society, Vol. 2: Physical Sciences: Tools and Techniques (2012), ISBN:  
978-0-9502463-6-9; 707

15. Viktoria Motsch, Stefan Löffler, Walid Hetaba, Peter Schattschneider:  
*Simulating HR-EFTEM images for orbital mapping*  
Poster: 15<sup>th</sup> European Microscopy Congress, Manchester, UK; 16.09.2012 – 21.09.2012; in:  
*Proceedings of the 15<sup>th</sup> European Microscopy Congress*, D.J. Stokes, W.M. Rainforth (Hrg.);  
The Royal Microscopic Society, Vol. 2: Physical Sciences: Tools and Techniques (2012), ISBN:  
978-0-9502463-6-9; 699
16. Stefan Löffler, Walid Hetaba, Peter Schattschneider:  
*Simulating the energy-loss near edge structure for interferometric EELS in reciprocal space*  
Poster: 15<sup>th</sup> European Microscopy Congress, Manchester, UK; 16.09.2012 – 21.09.2012; in:  
*Proceedings of the 15<sup>th</sup> European Microscopy Congress*, D.J. Stokes, W.M. Rainforth (Hrg.);  
The Royal Microscopic Society, Vol. 2: Physical Sciences: Tools and Techniques (2012), ISBN:  
978-0-9502463-6-9; 669
17. Walid Hetaba, Michael Stöger-Pollach, Stefan Löffler, Peter Schattschneider:  
*Advantages of the modified Becke-Johnson exchange potential for calculating EELS in WIEN2k*  
Poster: 10<sup>th</sup> Multinational Congress on Microscopy, Urbino, Italy; 04.09.2011 – 09.09.2011
18. Walid Hetaba, Stefan Löffler, Peter Schattschneider:  
*Site specific elemental analysis using electron channelling*  
Poster: 10<sup>th</sup> Multinational Congress on Microscopy, Urbino, Italy; 04.09.2011 – 09.09.2011
19. Michael Stöger-Pollach, Stefan Löffler, Walid Hetaba, Peter Schattschneider:  
*Investigating the optical properties of  $Al_xGa_{1-x}As$  by low voltage VEELS*  
Poster: 10<sup>th</sup> Multinational Congress on Microscopy, Urbino, Italy; 04.09.2011 – 09.09.2011
20. Walid Hetaba, Michael Stöger-Pollach, Stefan Löffler, Peter Schattschneider:  
*Advantages of the modified Becke-Johnson potential in WIEN2k for NiO demonstrated by EELS*  
Poster: Microscopy Conference 2011, Kiel, Germany; 28.08.2011 – 02.09.2011; in: *MC 2011 Kiel, Vol. 1: Instrumentation and Methods*, W. Jäger et al. (Hrg.) (2011), ISBN: 978-3-00-033910-3; IM5.P170
21. Walid Hetaba, Stefan Löffler, Peter Schattschneider:  
*Site selective elemental analysis under electron channelling conditions*  
Poster: Microscopy Conference 2011, Kiel, Germany; 28.08.2011 – 02.09.2011; in: *MC 2011 Kiel, Vol. 1: Instrumentation and Methods*, W. Jäger et al. (Hrg.) (2011), ISBN: 978-3-00-033910-3; IM5.P169
22. Michael Stöger-Pollach, Stefan Löffler, Walid Hetaba, Inga Ennen:  
*Low voltage low loss EELS for accurate determination of dielectric properties of semiconductors*  
Poster: Microscopy Conference 2011, Kiel, Germany; 28.08.2011 – 02.09.2011; in: *MC 2011 Kiel, Vol. 1: Instrumentation and Methods*, W. Jäger et al. (Hrg.) (2011), ISBN: 978-3-00-033910-3; IM5.P165

23. Inga Ennen, Stefan Löffler, Walid Hetaba, Michael Stöger-Pollach, Peter Schattschneider, Alexander Auge, Andreas Hütten:  
*Magnetic dichroism on the nanoscale*  
Poster: Microscopy Conference 2011, Kiel, Germany; 28.08.2011 – 02.09.2011; in: *MC 2011 Kiel, Vol. 1: Instrumentation and Methods*, W. Jäger et al. (Hrg.) (2011), ISBN: 978-3-00-033910-3; IM5.P164
24. Walid Hetaba, Anna Mogilatenko, W. Neumann, P. Schattschneider:  
*An ELNES study of LiAlO<sub>2</sub>*  
Poster: Microscopy Conference Graz, Dreiländertagung, Graz, Austria; 30.08.2009 – 04.09.2009; in: *MC Graz 2009, Vol. 1: Instrumentation and Methodology*, G. Kothleitner, M. Leich (Hrg.) (2009), ISBN: 978-3-85125-062-6; 125-126
25. Walid Hetaba, Peter Schattschneider:  
*Electron microscopy of LiAlO<sub>2</sub> – a promising substrate for opto-electronic devices*  
Poster: Junior Scientist Conference 2008, Vienna University of Technology, Austria; 16.11.2008 – 18.11.2008; in: *Proceedings of the Junior Scientist Conference 2008*, H.K. Kaiser, R. Kirner (Hrg.) (2008), ISBN: 978-3-200-01612-5; 149-150

### Vorträge und Posterpräsentationen (ohne Tagungsband-Eintrag)

1. Walid Hetaba, Stefan Löffler, Michael Stöger-Pollach, Andreas Hütten, Gareth Parkinson, Peter Schattschneider:  
*Probing magnetic phase transitions in Heusler-alloys and Magnetite using EMCD*  
Poster: 18. Tagung Festkörperanalytik, Wien, Österreich; 06.07.2015 – 08.07.2015
2. S. Löffler, W. Hetaba, M. Bugnet, M.-G. Willinger, M. E. Schuster, N. Gauquelin, S. Lazar, E. Assmann, K. Held, G. A. Botton, R. Schlögl, P. Schattschneider:  
*Mapping electronic orbitals in the TEM*  
Vortrag: 42<sup>nd</sup> MSC-SMC Annual Meeting 2015, Hamilton, Ontario, Canada; 26.05.2015 – 29.05.2015
3. W. Hetaba:  
*Mapping electronic structure using advanced TEM and EELS*  
Vortrag: Joint Group Seminar MPI-CEC, Mülheim an der Ruhr, Deutschland (eingeladen); 18.05.2015 – 19.05.2015
4. M. Stöger-Pollach, T. Schachinger, W. Hetaba, D. Abou-Ras:  
*Determining Optical Properties using Low Voltage EELS and Bessel Beams*  
Vortrag: 5th ASEM Workshop on Advanced Electron Microscopy, Medical University Graz (eingeladen); 07.05.2015 – 08.05.2015

5. Walid Hetaba:  
*EMCD as a probe for magnetic phase transitions*  
Vortrag: 3<sup>rd</sup> Electron Microscopy Project Day, Arbeitsgruppe Elektronenmikroskopie, Abteilung Anorganische Chemie, Fritz-Haber-Institut der Max-Planck-Gesellschaft, Berlin, Deutschland; 02.04.2015
6. Walid Hetaba, Tobias Huber, Michael Stöger-Pollach:  
*Aberration-corrected TEM investigation of Magnetite*  
Poster: 4<sup>th</sup> Annual SFB FOXSI PhD Workshop 2014, Haus im Ennstal, Österreich; 29.03.2015 – 01.04.2015
7. S. Löffler, W. Hetaba, M.-G. Willinger, M. E. Schuster, N. Gauquelin, S. Lazar, E. Assmann, K. Held, G. A. Botton, R. Schlögl, P. Schattschneider:  
*Mapping electronic orbitals in the TEM*  
Poster: Annual SFB FOXSI Symposium 2015, PhD WS "FOXSKI", Haus im Ennstal, NÖ; 29.03.2015 – 01.04.2015
8. Walid Hetaba:  
*The influence of coherence effects in inelastic electron scattering*  
Vortrag: Doktorandentag, Abteilung Anorganische Chemie, Fritz-Haber-Institut der Max-Planck-Gesellschaft, Berlin, Deutschland; 04.11.2014 – 5.11.2014
9. Walid Hetaba, Michael Stöger-Pollach, Rudi Rodemeier:  
*Investigating anisotropic materials using ELNES at variable beam energies*  
Vortrag: 4<sup>th</sup> ASEM-Workshop: Advanced Electron Microscopy, Medizinische Universität Wien, Wien, Österreich; 08.05.2014 – 09.05.2014
10. Walid Hetaba, Marc-Georg Willinger, Manfred Erwin Schuster, Stefan Löffler, Robert Schlögl, Peter Schattschneider:  
*Site-specific ionisation fine-structure of Rutile in the electron microscope*  
Poster: European Workshop on Spatially-Resolved Electron Spectroscopy & Three Country Workgroup meeting on EELS & EFTEM, Technische Universität Graz, Graz, Österreich; 23.04.2014 – 25.04.2014
11. Walid Hetaba, Tobias Huber, Michael Stöger-Pollach:  
*Analytical TEM investigation of Lanthanum Manganite (LSM) model electrodes*  
Poster: 3<sup>rd</sup> Annual SFB FOXSI PhD Workshop 2014, Hochkar, Österreich; 07.04.2014 – 10.04.2014
12. S. Löffler, W. Hetaba, M. Bugnet, M.-G. Willinger, M. E. Schuster, N. Gauquelin, S. Lazar, E. Assmann, K. Held, G. A. Botton, R. Schlögl, P. Schattschneider:  
*Mapping electronic orbitals in the TEM*  
Poster: 4<sup>th</sup> Annual SFB FOXSI PhD Workshop, Göstling/Ybbs; 07.04.2014 – 10.04.2014
13. Walid Hetaba:  
*Effects of Symmetry Breaking in Electron Energy-Loss Spectrometry*  
Vortrag: Arbeitsgruppe Elektronenmikroskopie, Abteilung Anorganische Chemie, Fritz-Haber-Institut der Max-Planck-Gesellschaft, Berlin, Deutschland (eingeladen); 19.12.2013

14. Stefan Löffler, Viktoria Motsch, Walid Hetaba, Ralf Hambach, Giulio Biddau, Lorenzo Pardini, Claudia Draxl, Ute Kaiser, Peter Schattschneider:  
*Towards mapping atomic orbitals in the TEM*  
Poster: Inauguration of the Vienna UltraSTEM lab – Workshop: New avenues for materials research by high-resolution microscopy, Wien, Österreich; 28.11.2013
15. Annalena Wolff, Walid Hetaba, Nadine Mill, Marco Wißbrock, Stefan Löffler, Peter Schattschneider, Norbert Sewald, Andreas Hütten:  
*Biomimetics: A promising route to obtain magnetically anisotropic nanoparticles*  
Poster: 5<sup>th</sup> Seeheim Conference on Magnetism 2013, Frankfurt, Deutschland; 29.09.2013 – 03.10.2013
16. Walid Hetaba:  
*Transmission Electron Microscopy for the Ferroic Cooling Project*  
Vortrag: SPP 1599 Ferroic Cooling Project Meeting, Leibniz-Institut für Festkörper- und Werkstoffforschung, Dresden, Deutschland; 27.09.2013
17. Walid Hetaba, Michael Stöger-Pollach, Johannes Bernardi, Simon Penner, Ramona Thalinger, Katharina Langer-Hansel, Tobias Huber, Astrid Wolfbeisser:  
*Chemical and Structural Analysis on the Nanoscale*  
Poster: 2<sup>nd</sup> Annual SFB FOXSI Symposium 2013, Burg Schlaining, Österreich; 18.09.2013 – 20.09.2013
18. Niclas Teichert, Lars Helmich, Walid Hetaba, Andreas Hütten:  
*Investigation of coupling phenomena in multi-layered Heusler alloys aiming for maximization of the magnetocaloric effect*  
SPP 1599 Ferroic Cooling Convention, Lichtenfels, Deutschland; 31.07.2013
19. Walid Hetaba, Marc-Georg Willinger, Manfred Schuster, Stefan Löffler, Robert Schlögl, Peter Schattschneider:  
*Site-specific ionisation edge fine-structure in the electron microscope*  
Vortrag: 3<sup>rd</sup> ASEM-Workshop: Advanced Electron Microscopy, Medizinische Universität Wien, Wien, Österreich; 25.04.2013 – 26.04.2013
20. Walid Hetaba:  
*Site-specific ionization edge fine-structure in the electron microscope*  
Vortrag: Max-Planck-Institut für chemische Energiekonversion, Mülheim a.d. Ruhr, Deutschland (eingeladen); 23.04.2013
21. Annalena Wolff, Idir Yahiatene, Walid Hetaba, Nadine Mill, Marco Wißbrock, Stefan Löffler, Katrin Eckstädt, Norbert Sewald, Peter Schattschneider, Andreas Hütten:  
*Understanding the protein-inorganic crystal interaction in bioinspired syntheses*  
Poster: DPG Frühjahrstagung Regensburg 2013, Regensburg, Deutschland; 10.03.2013 – 15.03.2013

22. Walid Hetaba:  
*Site-specific ionization edge fine-structure in the electron microscope*  
Vortrag: Electron Microscopy Project Day, Arbeitsgruppe Elektronenmikroskopie, Abteilung Anorganische Chemie, Fritz-Haber-Institut der Max-Planck-Gesellschaft, Berlin, Deutschland; 06.11.2012
23. Annalena Wolff, Katrin Eckstädt, Walid Hetaba, Marco Wißbrock, Nadine Mill, Stefan Löffler, Norbert Sewald, Peter Schattschneider, Andreas Hütten:  
*Synthetic Polypeptide c25-mms6 alters Cobalt Ferrite Nanoparticle Growth*  
Vortrag: 16. Deutsche Physikerinnentagung, Freiburg, Deutschland; 25.10.2012 – 28.10.2012
24. Walid Hetaba, Stefan Löffler, Peter Schattschneider:  
*Site selective analysis using electron channelling*  
Vortrag: Arbeitsgruppe Elektronenmikroskopie, Abteilung Anorganische Chemie, Fritz-Haber-Institut der Max-Planck-Gesellschaft, Berlin, Deutschland; 24.07.2012
25. Walid Hetaba, Stefan Löffler, Peter Schattschneider:  
*Simulations of energy loss spectra: Advances and future prospects*  
Vortrag: 2<sup>nd</sup> ASEM-Workshop: Advanced Electron Microscopy, Salzburg, Österreich; 26.04.2012 – 27.04.2012
26. V. Motsch, S. Löffler, W. Hetaba, P. Schattschneider:  
*Simulating HR-EFTEM images*  
Vortrag: 2<sup>nd</sup> ASEM - Workshop, Salzburg, Österreich; 26.04.2012 - 27.04.2012
27. Annalena Wolff, Katrin Frese, Marco Wißbrock, Katrin Eckstädt, Inga Ennen, Walid Hetaba, Stefan Löffler, Anna Regtmeier, Patrick Thomas, Norbert Sewald, Peter Schattschneider, Andreas Hütten:  
*Influence of the synthetic polypeptide c25-mms6 on nanoparticle growth*  
Vortrag: DPG Frühjahrstagung Berlin, Berlin, Deutschland; 25.03.2012 – 30.03.2012
28. Walid Hetaba, Michael Stöger-Pollach, Peter Schattschneider:  
*Advantages of the modified Becke-Johnson exchange potential for calculating EELS in WIEN2k*  
Poster: 16. Tagung Festkörperanalytik, Wien, Österreich; 04.07.2011 – 06.07.2011
29. Michael Stöger-Pollach, Stefan Löffler, Walid Hetaba, Johannes Bernardi:  
*Low voltage low loss EELS for determination of optical properties of semiconductors*  
Poster: 16. Tagung Festkörperanalytik, Wien, Österreich; 04.07.2011 – 06.07.2011
30. Walid Hetaba, Stefan Löffler, Peter Schattschneider:  
*Site selective analysis under electron channelling conditions*  
Vortrag: 1<sup>st</sup> ASEM-Workshop: Advanced Electron Microscopy, Graz, Österreich; 07.04.2011 – 08.04.2011

31. Walid Hetaba:  
*Die Verwendung von WIEN2k zur Berechnung von Energieverlustspektren*  
Vortrag: Arbeitsgruppe Transmissionselektronenmikroskopie, Institut für Physik, Humboldt-Universität zu Berlin, Berlin, Deutschland (eingeladen); 29.11.2010
32. Walid Hetaba, Stefan Löffler, Peter Schattschneider:  
*Site selective analysis using electron channelling*  
Vortrag: 7<sup>th</sup> Workshop on EELS/EFTEM, Zürich, Schweiz; 27.10.2010 – 29.10.2010
33. Walid Hetaba, Michael Stöger-Pollach, Peter Schattschneider, Fabien Tran, Peter Blaha:  
*EELS of NiO: an ELNES study using a modified Becke-Johnson Potential*  
Poster: 7<sup>th</sup> Workshop on EELS/EFTEM, Zürich, Schweiz; 27.10.2010 – 29.10.2010
34. Walid Hetaba:  
*An ELNES study of LiAlO<sub>2</sub>*  
Vortrag: Jahreshauptversammlung der Österreichischen Gesellschaft für Elektronenmikroskopie, Wien, Österreich; 28.01.2010
35. Walid Hetaba, Anna Mogilatenko, Wolfgang Neumann, Peter Schattschneider:  
*An ELNES study of LiAlO<sub>2</sub>*  
Poster: 24th Workshop on Novel Materials and Superconductivity, Plannersalm, Österreich; 21.02.2009 – 28.02.2009
36. Walid Hetaba:  
*O-K ELNES Simulationen zur Phasenanalyse von Einschlüssen in LiAlO<sub>2</sub>*  
Vortrag: Materialwissenschaftlich-kristallographisches Seminar, Arbeitsgruppe Kristallographie, Institut für Physik, Humboldt-Universität zu Berlin, Berlin, Deutschland; 19.06.2008

## Diplomarbeit

1. Walid Hetaba:  
*Fine Structure and Site Specific Energy Loss Spectra of NiO*  
Betreuer: Peter Schattschneider; Institut für Festkörperphysik, Technische Universität Wien, 2011

## Reviewer

1. 2013 für Ultramicroscopy